

UNIVERSITÀ  
DEGLI STUDI  
DI PADOVA

Sede Amministrativa: Università degli Studi di Padova  
Dipartimento di Fisica e Astronomia “Galileo Galilei”

---

SCUOLA DI DOTTORATO DI RICERCA IN FISICA  
CICLO XXV

# An Imaging Camera for Biomedical Application Based on Compton Scattering of Gamma Rays

Direttore della scuola: Ch.mo Prof. Andrea Vitturi

Supervisore: Ch.mo Prof. Paolo Rossi

Dottorando: Cristiano Lino Fontana



A paperclip can be a wondrous thing.  
More times than I can remember, one of these  
has gotten me out of a tight spot.  
— *MacGyver*



## Abstract

In this thesis we present the R&D of a Compton Camera (CC) for small object imaging. The CC concept requires two detectors to obtain the incoming direction of the gamma ray. This approach, sometimes named “Electronic Collimation,” differs from the usual technique that employs collimators for physically selecting gamma-rays of a given direction. This solution offers the advantage of much greater sensitivity and hence smaller doses. We propose a novel design, which uses two similar Position Sensitive Photomultipliers (Hamamatsu 8500) coupled to different scintillators (one plastic and one inorganic). Assets of just one kind of detector are the simplicity of design and operation. Along the experimental apparatus we present our original algorithm for image reconstruction, that was tested with a Geant4 Monte Carlo code. Employed on experimental data, we obtained a resolution of 6 mm, which is suitable for small animal imaging (such as rats or rabbits) and for small human organs imaging (thyroid and prostate). The prototype was designed to be a compact modular element that can be extended placing more similar detectors side by side.

## Sommario

In questa tesi presentiamo il lavoro di ricerca e sviluppo di una Camera Compton (CC) per *imaging* di piccoli oggetti. Le CC richiedono l'utilizzo di due rivelatori per ottenere la direzione d'incidenza di raggi gamma. Questo approccio, talvolta chiamato “Collimazione Elettronica,” si differenzia dalle tecniche usuali che utilizzano collimatori per selezionare fisicamente i raggi gamma di una certa direzione. Questa soluzione offre il vantaggio di una sensibilità maggiore e quindi di dosi inferiori. Proponiamo qui un nuovo sistema, che usa due simili Fotomoltiplicatori sensibili alla posizione (Hamamatsu 8500) accoppiati a differenti scintillatori (uno in plastica ed uno inorganico). Avere un solo tipo di rivelatore comporta una maggiore semplicità di progettazione ed utilizzo. Assieme all'apparato sperimentale, presentiamo il nostro algoritmo originale per la ricostruzione d'immagini, che è stato testato con un codice Monte Carlo scritto con Geant4. Applicando l'algoritmo ai dati sperimentali, abbiamo ottenuto una risoluzione di 6 mm, che è adatta all'imaging di piccoli animali (quali ratti e conigli) e per piccoli organi umani (tiroide e prostata). Il prototipo è stato sviluppato per essere un elemento modulare compatto, che può essere esteso affiancando altri rivelatori simili.



# Acknowledgments

I would like to thank who helped me making all of this possible:

- The University of the Studies of Padua, the Foundation Cariparo and the INFN for funding and supporting my PhD project;
- my parents Federica and Giorgio for their unique support;
- Giovanna Frigo for staying at my side no matter what;
- Paolo Rossi for giving me this great opportunity here in Italy and for the experience that I had at the Sandia National Labs (USA);
- FMB Informatica s.n.c. for offering the developed board PCB layout for free;
- Inel Elettronica s.r.l. and Giuseppe Lando for letting me borrow their oscilloscope for months;
- Nikolay Uzunov for his experimental and theoretical help and advice, and for his plastic scintillator;
- Michele Bello for his help with electronics and everything else;
- Konstantin Atroshchenko for his help with LabVIEW;
- Giovanni Di Domenico for his precious suggestions;
- Marcello Rotondo for the relaxing coffee breaks (*cafeeeee<sup>TM</sup>*);
- Barney L. Doyle for the opportunities given me at the Sandia National Labs, at the Lawrence Berkeley National Lab (USA) and at the Lawrence Livermore National Lab (USA).
- Denis Conventi and his collaborators of the LNL mechanical workshop, for their marvellous and quick work;
- Fabiana Gramegna for letting us use her lab for our experimental work;
- Laura Melendez for cheering up our lab and arguing with Paolo;
- Matteo Pegoraro for his advices for electronics;
- Giovanni Carugno, Leonardo La Torre, Roberto Stroili, Calir Ur and Giuseppe Viesti for letting us borrow their NIM and VME modules;
- Luca Stevanto for reminding me something very important.





# Contents

<b>1. Introduction</b>	<b>1</b>
1.1. Rationale	1
1.1.1. Collaboration	1
1.1.2. Why a Compton camera?	2
1.2. Medical Imaging With Gamma-Rays	2
1.3. Interactions of gamma and X-rays for medical applications with matter	3
1.4. Scintillating materials	4
1.4.1. Scintillator characteristics	6
1.4.2. Continuous and Segmented scintillators	7
1.5. Photomultipliers	7
1.5.1. Principles of operation	7
1.5.2. Position sensitive Photomultipliers	8
1.6. Gamma-rays and X-rays collimators	8
1.7. SPECT Imaging system	12
<b>2. Apparatus Design</b>	<b>13</b>
2.1. Scintillators	13
2.1.1. Tracker	13
2.1.2. Calorimeter	17
2.2. Photomultiplier	17
2.3. Readout Electronics	19
<b>3. Image Reconstruction</b>	<b>21</b>
3.1. Compton Interaction	21
3.2. Released energy spectrum	23
3.3. Angle uncertainty	24
3.4. Compton cones	24
3.4.1. Numerical solutions of $S(\hat{u}) = 0$	27
3.4.2. Cone Weighting	32
3.5. Image generation	32
<b>4. Geant4 Simulation</b>	<b>39</b>
4.1. <code>PhysicsList</code> class description	39
4.2. <code>DetectorConstruction</code> class description	39
4.3. <code>PrimaryGeneratorAction</code> class description	40
4.4. <code>SensitiveDetector</code> and <code>Hit</code> class descriptions	41
4.5. Trajectories	41
4.6. Actions	41
4.7. Simulation results	42

<b>5. Readout Electronics</b>	<b>45</b>
5.1. Requirements . . . . .	45
5.2. Charge Multiplexing Circuits . . . . .	45
5.3. Signal Preamplifiers . . . . .	48
5.4. Charge Multiplexing and Preamplifier PCB . . . . .	51
5.5. Trigger generation . . . . .	53
5.6. NIM-TTL Converter . . . . .	53
5.7. Circuit simulation . . . . .	53
5.8. Current pulse generator . . . . .	62
5.9. LED pulse generator . . . . .	63
<b>6. Acquisition software</b>	<b>71</b>
6.1. Hardware interface and Signals acquisition . . . . .	71
6.2. Signals analysis . . . . .	75
6.3. Data storing . . . . .	75
<b>7. Detectors calibration and characterization</b>	<b>77</b>
7.1. Calorimeter calibration . . . . .	77
7.1.1. Energy calibration . . . . .	77
7.1.2. Photomultiplier spatial linearization . . . . .	77
7.1.3. Scintillator spatial calibration . . . . .	81
7.1.4. Uniformity . . . . .	81
7.2. Tracker calibration . . . . .	82
7.2.1. Energy calibration . . . . .	82
7.2.2. Photomultiplier spatial linearization . . . . .	82
7.2.3. Continuous scintillator spatial calibration . . . . .	84
7.2.4. Continuous scintillator uniformity . . . . .	84
7.2.5. Segmented scintillator spatial calibration and uniformity . . . . .	84
<b>8. Image formation model</b>	<b>89</b>
<b>9. Collimated images</b>	<b>95</b>
<b>10. Images using Compton scattered gamma-rays</b>	<b>99</b>
10.1. Detector spectra during coincidences . . . . .	99
10.2. Bidimensional energy spectrum . . . . .	99
10.3. Compton Images . . . . .	102
<b>11. Conclusions</b>	<b>109</b>
<b>A. Charge Multiplexing and Preamplifier PCB</b>	<b>111</b>
<b>Bibliography</b>	<b>127</b>

## List of Figures

1.1.	Some examples of inorganic scintillators. . . . .	5
1.2.	An example of an organic scintillator, NE102. . . . .	6
1.3.	Lead collimators for gamma-rays. . . . .	9
1.4.	Different kinds of lead collimators for gamma-rays. . . . .	10
1.5.	POV-ray simulation of an image of a collimated point-like source, holes diameter 1 mm, holes depth 20 mm, septa 0.1 mm, source distance 14 cm. . . . .	11
1.6.	Some parameters for lead collimators. . . . .	11
1.7.	A sketch of an imaging system. . . . .	12
2.1.	Complete apparatus of Calorimeter (top detector) and Tracker (right detector) mounted on the automatic positioning system. . . . .	14
2.2.	Electron stopping power for Vinyltoluene [Ber+05]. . . . .	15
2.3.	Continuous 4 mm thick plastic scintillator. . . . .	15
2.4.	Segmented 12 mm thick plastic scintillator. . . . .	16
2.5.	Continuous 4 mm LaBr <sub>3</sub> scintillator, damages and breaks are easily visible. . . . .	17
2.6.	Hamamatsu 8500 Photomultiplier. . . . .	18
3.1.	A photon of energy $E$ interacts with an electron and is scattered by an angle $\Theta$ with an energy $E'$ . . . . .	22
3.2.	Dependency of Compton cross section on the scattering angle, at some significant energies, from equation (3.5) on page 21. . . . .	22
3.3.	Spectra of recoiling electrons from Compton interactions, at some significant energies, from equation (3.8) on page 23. . . . .	23
3.4.	Angle uncertainties for a gamma-ray of 142 keV, plotted against the electron energy $E_e$ and the measurement relative error. . . . .	25
3.5.	Compton cones obtained by the scattering direction and scattering angle. . . . .	26
3.6.	POV-ray [Pov] simulation of the intersection of three Compton cones. . . . .	27
3.7.	Intersection between the unit sphere and the Compton cone, the real photon path is drawn and the radius of the intersection circle. . . . .	28
3.8.	Locus of $S(\hat{u}) = 0$ on a $(\theta, \varphi)$ bidimensional mesh; red dots show positive values of the function, while blue dots show negative values. Arrows indicate the algorithm path on the mesh, with labels indicating the preceding step kind. . . . .	28
3.9.	Examples of locuses of $S(\hat{u}) = 0$ on a $(\theta, \varphi)$ bidimensional mesh. . . . .	29

3.10. Zoom of roots of $S(\cdot)$ obtained with an algorithm from the Octave standard library. . . . .	31
3.11. Execution times per reconstructed cone at different levels of subdivisions of the $\theta$ domain. . . . .	32
3.12. Projections on the tracker plane of the four-dimensional histogram $h(\cdot)$ . . . . .	33
3.13. $(\theta, \varphi)$ space associated to the simulation of the Point Spread Function (the color scale represents the logarithm of the actual counts). . . . .	34
3.14. Simulations of $(\theta, \varphi)$ spaces associated to different subdivisions of the Tracker for a point-like source. . . . .	35
3.15. Example image of a simulation of a point-like source projected on the Tracker plane, source distance 2.5 cm, image reconstruction resolution 1 mm, angular resolution 0.05 rad, $1.3 \cdot 10^6$ Compton events. . . . .	37
3.16. Example image of a simulation of a point-like source projected on the Tracker plane, source distance 2.5 cm, image reconstruction resolution 1 mm, angular resolution 0.05 rad, $1.3 \cdot 10^6$ Compton events. . . . .	38
4.1. Simulations geometries, the left one is called “Forward” geometry, the right one is called “Side” geometry. . . . .	40
4.2. Dependence of the scattering angle from the recoiling electron energy, obtained from the Geant4 simulations, the theoretical plot is superimposed on the data. . . . .	42
4.3. Dependence of the scattering angle from the recoiling electron energy, obtained from the Geant4 simulations of 142 keV gamma-rays, the theoretical plot is superimposed. . . . .	43
5.1. Block diagram of the readout electronics. . . . .	46
5.2. Resistor Net of a Discretized Position Circuit. . . . .	47
5.3. Signals of the four outputs of the Resistor Net, source $^{57}\text{Co}$ , scintillator $\text{LaBr}_3$ , high voltage 1000 V. . . . .	48
5.4. Signal preamplifier circuit schematic. . . . .	49
5.5. Signals of the four outputs of the preamplifier, source $^{57}\text{Co}$ , scintillator $\text{LaBr}_3$ , high voltage 1000 V. . . . .	50
5.6. Charge Multiplexing and Preamplifier PCB; Resistive Net on the top of the image, preamplifier on the bottom. . . . .	52
5.7. NIM to TTL converter with delay generation and dead-time generation. . . . .	54
5.8. Signals of the NIM to TTL converter. . . . .	55
5.9. Signals of the triggering electronics: (1) Fast H8500 triggering signal, (2) Timing Filter Amplifier output, (3) NIM triggering signal, (4) TTL triggering signal. . . . .	56
5.10. Edges of signals of the triggering electronics: (1) Fast H8500 triggering signal, (2) Timing Filter Amplifier output, (3) NIM triggering signal, (4) TTL triggering signal. . . . .	57

5.11. Signals of the triggering electronics: (1) Fast H8500 triggering signal, (2) TTL triggering signal, (3) Resistor Network signal, (4) Preamplifier signal. . . . .	58
5.12. Qucs [Quc] simulation schematic of resistor net and preamplifier. . . . .	59
5.13. Zoom of signal generator schematic and simulation parameters; exponential pulse shape, 10 ns rising time, 300 ns falling time, $-100 \mu\text{A}$ maximum. . . . .	60
5.14. Zoom of resistor net and preamplifier schematic. . . . .	60
5.15. Simulated analog signals of resistor net and preamplifier. . . . .	61
5.16. Anodes coordinates reconstructed with equations (5.2) and (5.3) applied to simulated signal peak values. . . . .	64
5.17. Signal strength in function of the position for output channel A of simulated signals. . . . .	65
5.18. Current Pulse generator . . . . .	65
5.19. Signals of the pulse generator (Figure 5.18 on page 65): (1) Input TTL signal from clock (variable frequency), test point 1; (2) Comparator output, test point 2; (3) Fast NIM trigger output; (4) Current pulse output. . . . .	66
5.20. Anodes coordinates reconstructed with equations (5.2) and (5.3) applied to real current signals of the developed current pulser. . . . .	67
5.21. Signal strength in function of the position for output channel A of real current signals of the developed current pulser. . . . .	68
5.22. LED Pulse generator . . . . .	68
5.23. Signals of the pulse generator (Figure 5.22 on page 68): (1) Input TTL signal from clock (variable frequency), test point 1; (2) Comparator output, test point 2; (3) Buffer output, test point 3; (4) Final pulse, test point 4. . . . .	69
6.1. Acquisition software front-panel. . . . .	72
6.2. Acquisition software block diagram. . . . .	73
6.3. Simplified block diagram showing only the hardware interface and interactions . . . . .	74
7.1. Calorimeter calibration spectra and regression line. . . . .	78
7.2. Dots generated in an uniform mesh with a LED and acquired with the Calorimeter. . . . .	79
7.3. Dots generated with a $^{57}\text{Co}$ source and acquired with the Calorimeter. . . . .	80
7.4. Calorimeter uniformity. . . . .	81
7.5. Tracker calibration spectra. . . . .	82
7.6. Dots generated in an uniform mesh with a LED and acquired with the Tracker. . . . .	83
7.7. Dots generated with a $^{57}\text{Co}$ source and acquired with the Tracker. . . . .	84
7.8. Tracker uniformity with the continuous scintillator. . . . .	85
7.9. Uniformity image of the Tracker with the segmented scintillator. . . . .	86
8.1. Diagrams of a monodimensional coordinate system and a bidimensional one. . . . .	89

8.2.	Monte Carlo generated signals of a grid of point-like sources 5 mm apart, spatial resolution is 0.25 mm (0.5%). . . . .	91
8.3.	Monte Carlo generated signals of a grid of point-like sources 5 mm apart, spatial resolution is 0.25 mm (0.5%) and a gaussian offset is added to the signals, with $\sigma = 3\%$ . . . . .	92
8.4.	Monte Carlo generated signals of a grid of point-like sources 5 mm apart, spatial resolution is 0.25 mm (0.5%), gaussian offset is added to the signals, with $\sigma = 3\%$ , and a saturation effect at the 80% of the maximum signal. . . . .	93
9.1.	Point-like $^{57}\text{Co}$ source in front of the Calorimeter with a parallel holes lead collimator. . . . .	96
9.2.	Circumference-like $^{57}\text{Co}$ source (radius 10 mm) in front of the Calorimeter with a parallel holes lead collimator. . . . .	97
10.1.	Detectors spectra simulated with Geant4 for a 142 keV gamma source, energy uncertainty 18%. . . . .	100
10.2.	Detectors spectra of real data for a 122 keV gamma from a $^{57}\text{Co}$ source, energy uncertainty 18%. . . . .	101
10.3.	Bidimensional energy histogram simulated with Geant4 for a 142 keV gamma source, energy uncertainty 18%. . . . .	102
10.4.	Bidimensional energy histogram of real data for a 122 keV gamma from a $^{57}\text{Co}$ source. (a) main Compton region, (b) second Compton region, (c) random coincidences between the Calorimeter full-energy peak and the Tracker, (d) random coincidences with the Calorimeter's $^{138}\text{La}$ , (e) Tracker overflow with higher energy Compton interactions. . . . .	103
10.5.	Real Compton images of a quasi-point-like $^{57}\text{Co}$ source, projected on the Tracker plane, selection on bidimensional spectrum FWHM wide. . . . .	104
10.6.	Real Compton images of a quasi-point-like $^{57}\text{Co}$ source, projected on the Tracker plane along different directions, selection on bidimensional spectrum FWHM wide. . . . .	105
10.7.	Real Compton images of a quasi-point-like $^{57}\text{Co}$ source, projected on the Tracker plane, selection on bidimensional spectrum FWHM/2 wide. . . . .	106
10.8.	Real Compton images of a quasi-point-like $^{57}\text{Co}$ source, projected on the Tracker plane, selection on bidimensional spectrum FWHM/3 wide. . . . .	107

# 1. Introduction

The purpose of this thesis is to develop an innovative SPECT (Single Photon Emission Computed Tomography) imaging system for biomedical application. This system, referred in the following as Compton Camera (CC), is able to image the biodistribution of radiopharmaceuticals in the body of test animals by measuring the gamma rays coming from the labeling radio-nuclide, mainly the  $^{99m}\text{Tc}$ , with a novel method based on the Compton Effect. This approach offers the advantage of much greater sensitivity and hence smaller doses. On the other hand, one has to face challenges like the necessity of precise energy and position measurements and the complexity of tri-dimensional tomography reconstruction. Introduction, historical overview, description of materials and methods, and account of my original work will follow.

## 1.1. Rationale

### 1.1.1. Collaboration

This work was carried out in the Laboratory for Radiopharmaceuticals and Molecular Imaging (*Laboratorio di Radiofarmaci ed Imaging Molecolare*, LRIM) in the National Laboratories of Legnaro (*Laboratori Nazionali di Legnaro*, LNL) in Legnaro (PD), Italy, under the scope of the experiments XDXL and APOTEMA of the Italian National Institute for Nuclear Physics (*Istituto Nazionale di Fisica Nucleare*, INFN). The initial objective for the XDXL experiment was to study and develop the use of Compton cameras (CC) for imaging of gamma and X-rays. The collaboration worked in parallel in two main fields

- astronomical X-ray imaging to develop compact Compton cameras for artificial satellites;
- biomedical gamma-ray imaging to develop compact Compton cameras for small animal and small human organs imaging.

The collaborations, of the INFN sections of Padua (Italy) and Legnaro, were responsible for the biomedical applications research and development. A first phase of the development was dedicated to a traditional collimated gamma-camera and a second to the development of a prototype of a small Compton camera. After the first few years the Padua and Legnaro collaborations passed to the scope of the APOTEMA experiment, whose main aim is to study the accelerator-driven production of Technetium and Molybdenum for medical applications. The collaborations are now specializing in the  $^{99m}\text{Tc}$  imaging and in its biomedical applications.

### 1.1.2. Why a Compton camera?

Compton cameras offer a series of advantages such as

- an enhancement of the efficiency due to the lack of the collimator [SHR99; Par00];
- a reduction of the patient administered dose due to the higher efficiency;
- an increase of the resolution due to the possibility of using higher energies (than the traditional 142 keV of  $^{99m}\text{Tc}$ ) [Ros+11a; Ros+11b];
- higher energies produce cleaner images due to the lower scattering probability inside the body of patients;
- can be used where a compact geometry is required, for instance for small organs imaging (thyroid, prostate, *etcetera*).

The use of gamma-ray sources of higher energies than the  $^{99m}\text{Tc}$  one was one of the key objectives of the XDXL experiment. A set of possible candidates for higher energy sources for nuclear medicine was proposed on [Mos+08] and include:  $^{131}\text{I}$  364 keV (thyroid),  $^{113\text{m}}\text{In}$  392 keV,  $^{85}\text{Sr}$  520 keV (bone scintigraphy),  $^{58}\text{Co}$  810 keV (pulmonary cancer),  $^{43}\text{K}$  610 keV (myocardium imaging), and some  $\beta^+$  emitters. These sources are suited for medical use for their short half-life, to reduce the patient dose, but long enough to be processed and prepared for injection and be metabolized by the patient.

After the passage to the APOTEMA experiment, the collaboration changed its research focus to the study of  $^{99m}\text{Tc}$  imaging. Some key objectives of the new experiment are

- development of an optimal production system of  $^{99}\text{Mo}$  or  $^{99m}\text{Tc}$  with a cyclotron;
- study of impurities in the produced sources;
- study of image quality depending on the characteristics of accelerator-produced radioactive sources.

For the latter the collaboration proposed the use of the compact Compton camera.

## 1.2. Medical Imaging With Gamma-Rays

The discovery of X-rays in 1895 by Wilhelm Röntgen induced a revolution in the medical diagnostics because physicians were able to “look” inside the body without having to open it [SQR95; Gf05]. The first X-rays images were of the planar kind, generated by an emitting source, and the object interposed was observed either in a fluorescent screen or by a light-sensitive photographic film. Later on, with the advent of cheap and fast computing capabilities, and the usage of CAT scanners (Computer Assisted Tomographic scanners), the images could show the tridimensional structure of objects.



Besides the traditional X-ray imaging another field originated from the Physics research, the *Diagnostic Nuclear Medicine*[AA+06]. The purpose is to study, with *in vivo* imaging, the physiology of diverse organs by labeling molecules with radioactive nuclides [Dou09]. These technique opened new horizons to the Medicine, because finally we were able to detect and analyze the path of molecules inside our body. New imaging methods on the basis of the detection of X-ray and gamma-ray emission, from the organs administered with labeled nuclides, arose during the last decades. Techniques such as the Positron Emission Tomography (PET) technology has been proposed and is used since 1951. It exploits the gamma-ray emission from specific positron-emitting radionuclides. The annihilation of each positron in the tissue produces a pair of aligned gamma-rays, propagating in opposite directions, that can be detected to image the source's biodistribution inside the body. Single Photon Computed Tomography (SPECT) scanners have been used since 1963. SPECT scanners produce tomographic images from single gamma rays emitted by certain kinds of radioactive nuclides administered in the organs. The gamma rays are easily detected using position-sensitive gamma-ray detectors, but it is intrinsically impossible to define their incoming direction, and thus to construct an image. Planar images on the scintillators are obtained with the use of different kinds of collimators such as pin-hole collimators, parallel-hole collimators, *etcetera*, in order to select a particular direction to image the source distribution. The use of gamma and X-rays is so widespread for some reasons

- their low interaction probabilities bring lower doses released to the patients;
- they can be easily produced with linear electron accelerators [TT06];
- gamma-ray sources can be easily handled because they can be sealed.

### 1.3. Interactions of gamma and X-rays for medical applications with matter

Photons, depending on their energy and on the material, undergo different kind of reactions [LR09]. At the interesting energies for Medical Imaging (from tens of keV to a few hundreds of keV) the dominating effects are

- *Photoelectric effect*, in which photons are absorbed by an atom, followed in most cases by a characteristic re-emission of photons;
- *Rayleigh scattering*, a coherent scattering in which photons leave atoms not excited nor ionized;
- *Compton scattering*, an incoherent scattering in which the photons ionize the atoms;
- *Pair production*, an interaction with a nucleus that generates a couple of electron and positron from the photon.

When photon beam passes through the matter, it is attenuated due to the above cited processes. It shows an exponential decrease of its intensity according to the law

$$I(x) = I_0 e^{-\mu x} \quad (1.1)$$

where  $I_0$  is the initial intensity,  $I(\cdot)$  is the intensity of the beam at the depth  $x$ , and  $\mu$  is a linear attenuation coefficient, depending on the element composition of the matter.

The Photoelectric effect occurs when a photon interacts with an atom and ionizes it, and thus it depends strongly on the atomic properties. In this process the photon is absorbed. The linear attenuation coefficient shows rapid changes in the vicinity of the atomic energy levels. The photoelectric effect is the predominant interaction until energies of the order of 50 keV to 100 keV, for light elements such as Carbon, Silicon or Oxygen. For heavier elements, such as Lead or Tungsten, it can be the major effect up to energies of the order of the 1 MeV.

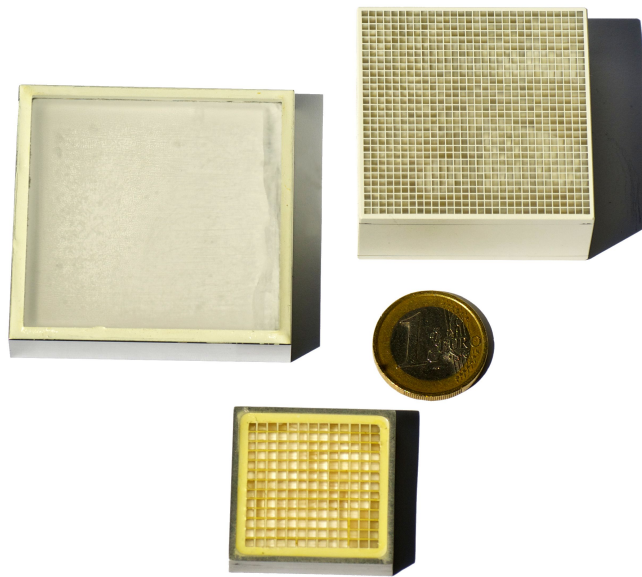
The Rayleigh scattering is a coherent scattering of a photon beam by atoms that are excited and consecutively re-emit photons with the same wavelength [DZ09]. Photons of a few keV are used for X-rays or gamma-rays diffraction studies on crystals, for instance. The influence of the Rayleigh scattering on the attenuation coefficients decreases with the energy of the photons, and practically this kind of scattering has no effect at the energy range of interest for Medical Imaging.

Compton scattering is an incoherent interaction of photons that interact with electrons of the material. The photon transmits part of his energy to the electron which consequently recoils. This kind of interaction is dominating for the light elements for energies from 50 keV to 100 keV. For heavier elements, however, it can be completely overwhelmed by the photoelectric effect. The Compton linear attenuation coefficient remains almost constant up to the threshold energy of about 1 MeV, in which the pair production becomes dominant (also for heavier elements). The reason of this steadiness is that the photons interact mostly with free (or lightly bounded) electrons in the material and thus do not depend on the material properties. For a more detailed explanation see section 3.1 on page 21.

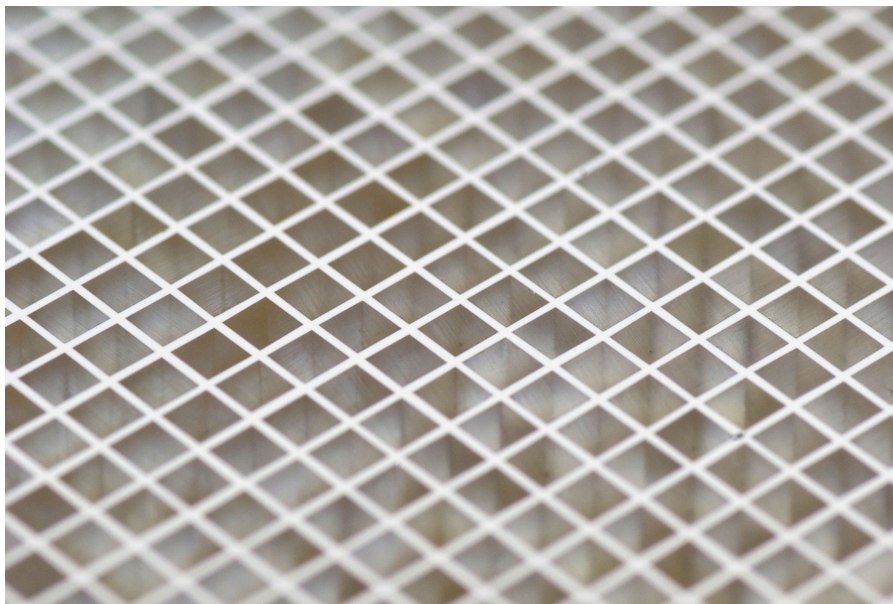
After the Compton region, at about 1 MeV the pair production region rises. At those energies the photons interact with nuclei with the sufficient energy for producing couples of electron and positron.

## 1.4. Scintillating materials

During the interaction with ionizing radiations, some materials show the mostly peculiar behaviour of emitting optical photons that can be detected by photo-sensible apparatuses. This phenomenon known as *scintillation* was used in some of the first techniques for radiation detection and nowadays it is still widely used [Kno10].



(a) (Left)  $\text{LaBr}_3$  continuous scintillator, (Right) LYSO segmented scintillator, (Bottom) CsI segmented scintillator.



(b) Zoom of the segmented LYSO.

Figure 1.1.: Some examples of inorganic scintillators.

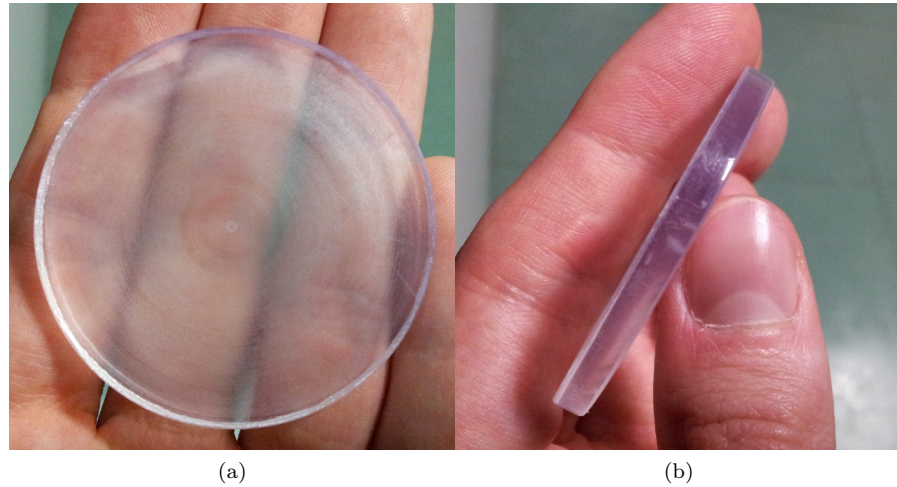


Figure 1.2.: An example of an organic scintillator, NE102.

#### 1.4.1. Scintillator characteristics

The characteristics of the different scintillators vary depending on their constituents, some important parameters are

- Light yield or scintillation efficiency;
- yield linearity;
- transparency at the emission wavelength;
- light decay time;
- manufacture, machinability and handling;
- refraction index.

The most used materials are inorganic alkali halide crystals (Figure 1.1 on the previous page) or organic liquids and plastics (Figure 1.2). Usually inorganic materials (such as NaI, LaBr<sub>3</sub>, LuYSiO<sub>4</sub>, *etcetera*) have high light yields, good linearity and high stopping power, but are rather slow (with some exceptions). Decay times go from 1  $\mu$ s, of CsI(Tl), to the fast 25 ns of LaBr<sub>3</sub>(Ce). Organic scintillators are extremely fast (times of the order of the ns) but have lower light yields. Depending on the application one kind can be favorable over the other, for instance the high  $Z$  inorganic scintillators easily absorb gamma-rays or X-rays but can not be used for neutron detection. Organic scintillators are composed of light elements and thus have the tendency of producing mostly Compton interactions with ionizing photons and not the photoelectric effect. Organic scintillators, also, for their richness of hydrogen are used for neutron detection.

Inorganic scintillators also show the best spatial resolution due to their higher stopping power and thus smaller mean free path for the photons. A

limiting factor implied by the inorganic scintillators is their light decay time, the decay time gives an upper bound to the acquisition rate that can be expected. A typical dose used for small animal imaging is of the order of 100 MBq, with an efficiency of about  $10^{-4}$  it leads to about  $10^4$  events per second [Gue04]. This turns out to be a rate that can be sustained even by slow scintillators, such as CsI. A problem of some inorganic scintillators is their hygroscopy, *id est* the ability to absorb water, that requires them to be kept away from humidity, in watertight containers. Highly hygroscopic crystals are NaI and LaBr<sub>3</sub>, that are literally destroyed by the mere air humidity.

### 1.4.2. Continuous and Segmented scintillators

Scintillators can be continuous, *id est* a single slab of material, or segmented, *id est* a set of scintillating pillars glued together (Figure 1.1 on page 5). Continuous scintillators are easily produced (up to certain dimensions) and for some materials are mandatory, for instance LaBr<sub>3</sub> scintillators are very difficult to machine for their hygroscopy. The spatial resolution can be worse than the segmented scintillators because, in a scintillation event, the emitted light is isotropic and thus part of the light is lost in internal reflections, on the interfaces between the crystal and a photomultiplier window. Segmented scintillators are composed of a set of pillars with a small cross section, compared to the length. Between the pillars a reflective material is inserted in order to increase the internal reflections and bring most of the light to the front face. The pillar length can not be too much because the number of internal reflections would eventually fade the light, and thus making the ulterior length useless. The advantage of such set-up is that the light is roughly uniform on the face of each pillar, and it is independent on the interaction depth. The light output is therefore concentrated on each pillar face and a position sensitive detector can identify each pillar. The spatial resolution is the grid stride. By identifying each pillar it is also easier to calibrate the energy responses for each one of them. A drawback is the dead volume, constituted by the reflective layers, that reduces the sensitivity.

## 1.5. Photomultipliers

### 1.5.1. Principles of operation

Photomultipliers (PMTs) are one of the kinds of photo-sensitive detectors, they are constituted by an entrance transparent window, on which a thin metal layer is deposited, followed by a series of metallic plates or grids, all is enclosed in a vacuum tube [Ham]. The thin metal layer at the entrance is called *photocathode* and it generates electrons with the photoelectric effect of photons hitting it. The photoelectrons are emitted in the internal vacuum of the tube and are accelerated by the high voltage applied to the plates, which are called *dynodes*. When electrons hit the dynodes their energy is partially used to eject secondary electrons. Having a series of dynodes, at each stage the number of electrons is multiplied by a certain factor depending also on the voltage. After the electron multiplying phase, the electrons are collected

by an anode. A typical signal amplification factor is about  $10^6$  but it must be multiplied by the *quantum efficiency*, *id est* the ratio between the photons that emit a photoelectron and the total number of photons, that can be about 20%.

### 1.5.2. Position sensitive Photomultipliers

Besides a high amplification, certain kinds of photomultipliers can give also position information. Two mainstream approaches are used

- cross-wire (or cross-plate) anodes;
- multianodes.

The former has two anodes, one for  $x$  and one for  $y$ , that give two signals each and the differences between the signals give the position along that direction. The latter has multiple anodes, one for each position.

## 1.6. Gamma-rays and X-rays collimators

To produce an image of a real object a projection is required to reduce its structure from a tridimensional description to a bidimensional description. A projection has a well-known mathematical description as a linear operator that has a domain with more dimensions than the codomain [Can96]. The image formation process involves a physical mean that is able to project the imaged object to a bidimensional description; such means could be camera lenses or light collimators. The common techniques consist in the use of collimators to select gamma-rays emitted from an incoherent source and thus obtain a projection [Pre11; Ros+11b]. Collimators are made of heavy elements, such as lead or tungsten, and can be a tight mesh of small holes on the material (Figure 1.3 on the facing page); this approach has the downsides of dramatically reducing the number of detected gamma-rays, reducing efficiency, and the mechanical engineering problem of handling those heavy objects. There are different kind of collimators (Figure 1.4 on page 10):

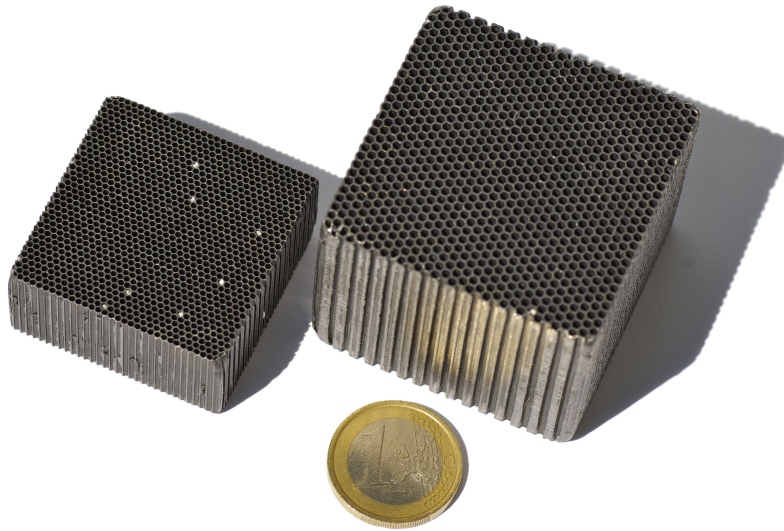
- (a) Parallel holes in which the image is a 1:1 projection of the source;
- (b) Converging or diverging collimators which can magnify or demagnify the source;
- (c) Pinhole collimators which can magnify more but have a much lower sensitivity.

For this work we will be interested only in parallel collimators, and a very short review follows.

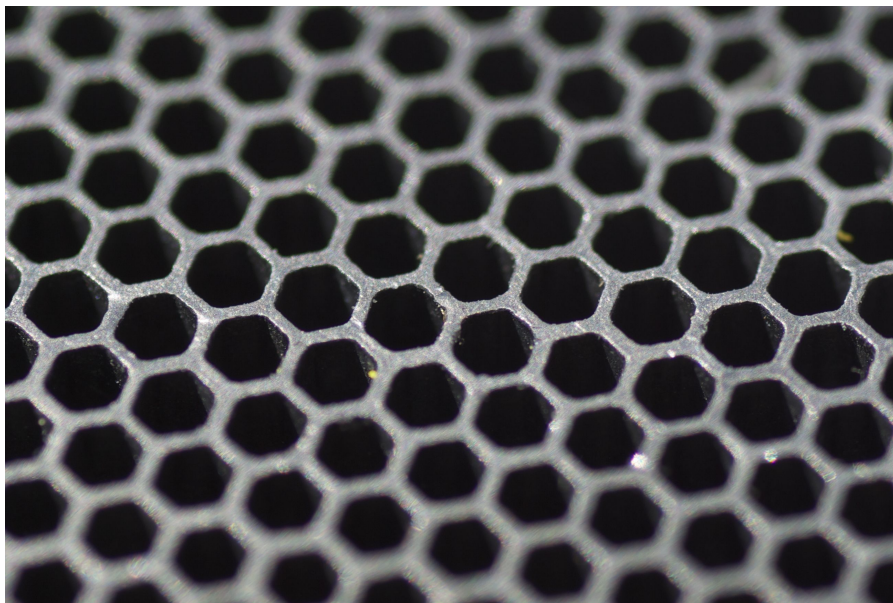
The angular acceptance of a parallel collimator can be defined as [SP03]:

$$\alpha = \arctan\left(\frac{a}{d}\right) \quad (1.2)$$

where  $a$  is the holes diameter and  $d$  is the holes depth (Figure 1.6 on page 11). Obviously, increasing the angular acceptance the sensitivity is increased but

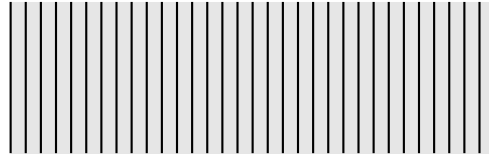


(a)

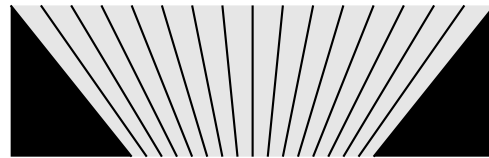


(b) Zoom of the small hexagonal holes

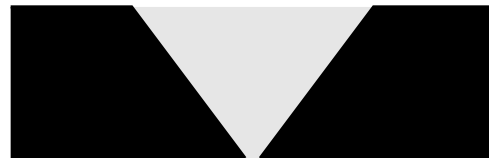
Figure 1.3.: Lead collimators for gamma-rays.



(a) Parallel holes collimator



(b) Converging holes collimator



(c) Pinhole collimator

Figure 1.4.: Different kinds of lead collimators for gamma-rays.



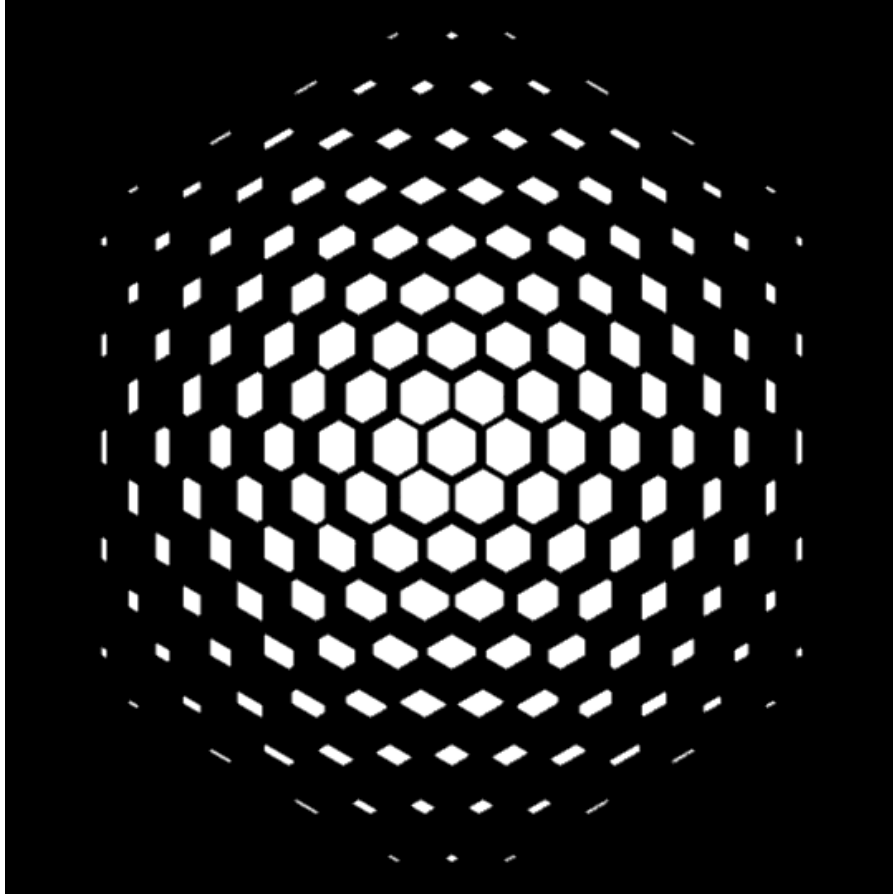


Figure 1.5.: POV-ray simulation of an image of a collimated point-like source, holes diameter 1 mm, holes depth 20 mm, septa 0.1 mm, source distance 14 cm.

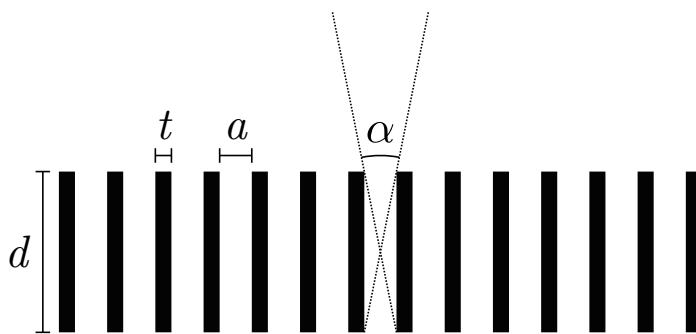


Figure 1.6.: Some parameters for lead collimators.

the resolution is worsened and *vice versa*. Septa thickness should be enough so that gamma rays do not pass through them but not too much in order to maximize the sensitivity. An optimum value is about [SP03]:

$$t \geq \frac{6 a/\mu}{d - 3/\mu} \quad (1.3)$$

where  $\mu$  is the linear attenuation coefficient at the gamma energy.

## 1.7. SPECT Imaging system

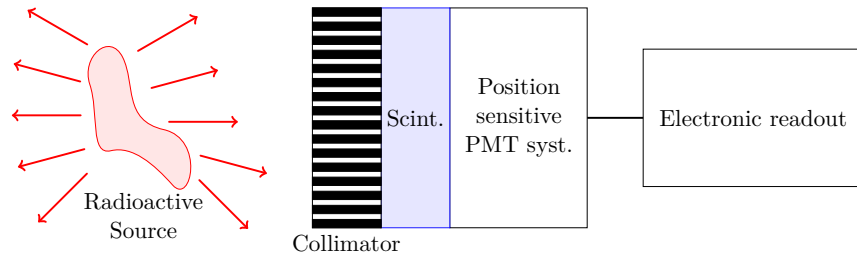


Figure 1.7.: A sketch of an imaging system.

The common SPECT imaging system integrates the previously described objects (Figure 1.7). A collimator is positioned in front of a scintillator which is coupled to a position sensitive photomultiplier system. Usually collimators are enclosed in protecting packages due to their fragility and cost. Scintillators are attached to the photomultipliers with optical glues, optical greases or optical rubbers that have refraction indexes similar to the glass and scintillating materials, in order to reduce the reflections on the interfaces. Finally there is the electronics for the data acquisition and storing. The whole system is mounted on mechanical structures that allow it to be easily moved, for linear scans, or to be rotated around the imaging object, for 3D reconstructions.

## 2. Apparatus Design

As stated before our purpose is to develop an innovative SPECT detector that, instead of using a collimator, uses the Compton effect to define the gamma-rays directions. The detector being designed with a cost-driven point of view, we decided to sacrifice the detector performances in favour of a low-budget approach. In figure 2.1 on the following page we can see the complete apparatus composed of two detectors and mounted on an automatic positioning system.

If we want to analyse Compton events we must measure the photon energy before and after the Compton interaction and its outgoing direction. Ideally, knowing the recoiling electron direction would be sufficient to completely reconstruct the event, but our design prevents us from acquiring this information. In figure 2.2 on page 15 we can see a plot of the electron total stopping power of vilyltoluene (a kind of plastic used for scintillators). At the maximum energy of the recoil electron the stopping power is about  $51 \text{ MeV cm}^{-1}$  that corresponds to a mean free path of about  $27 \mu\text{m}$ . This means that the maximum thickness to be able to see the recoil electron is about  $27 \mu\text{m}$ , which is not feasible. Apparatuses that are not able to measure the recoil electron direction are sometimes defined as *incomplete* detectors [Fon+11; Ros+11a; Ros+11b]. In this case one had to develop a complex reconstruction algorithm, described on chapter 3 on page 21. To measure the required parameters we decided to use two different detectors

- a *Tracker* forming the scattering volume, in which the photon undergoes the Compton interaction;
- a *Calorimeter* that completely absorbs the photon after the Compton interaction.

Both the detectors are photomultipliers coupled to a scintillator:

- the Tracker has a plastic scintillator to maximize the Compton probability;
- the Calorimeter has a inorganic scintillator to maximize the Photoelectric probability, and thus the complete absorption.

### 2.1. Scintillators

#### 2.1.1. Tracker

As the Tracker scintillator we used a plastic scintillator of the NE102 family [Ne1; Naq+93]. The base material is polyvinyltoluene, which has a density

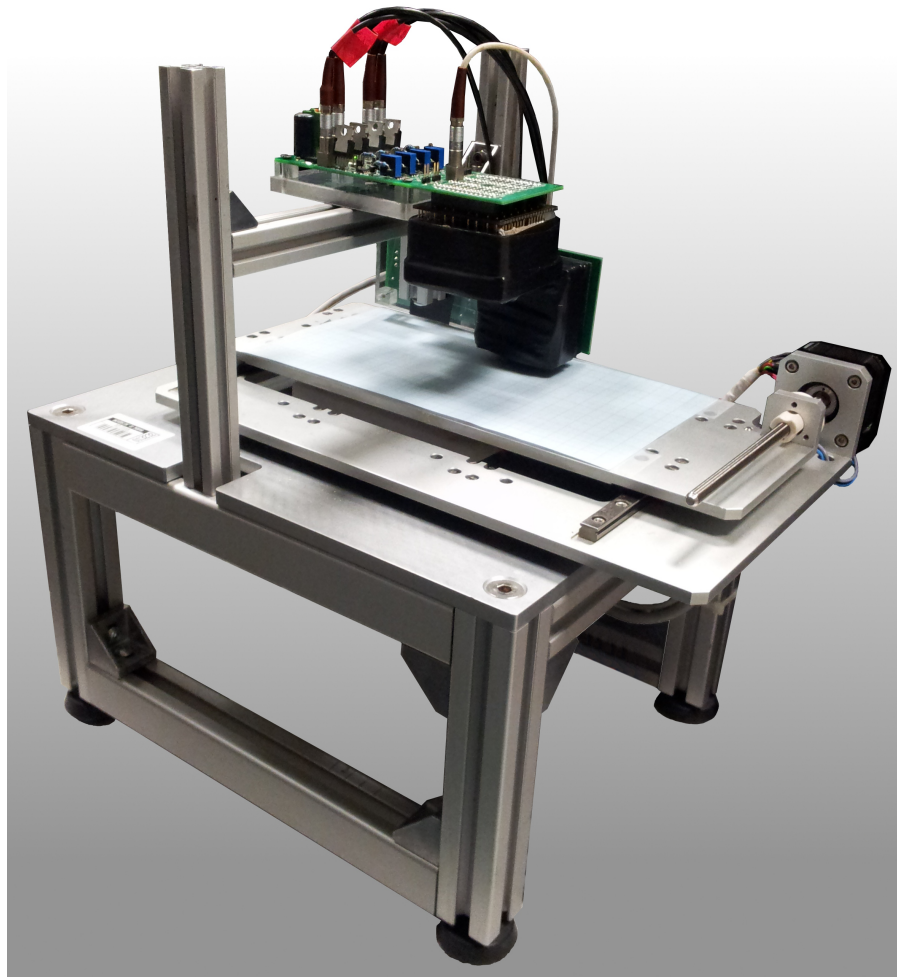


Figure 2.1.: Complete apparatus of Calorimeter (top detector) and Tracker (right detector) mounted on the automatic positioning system.

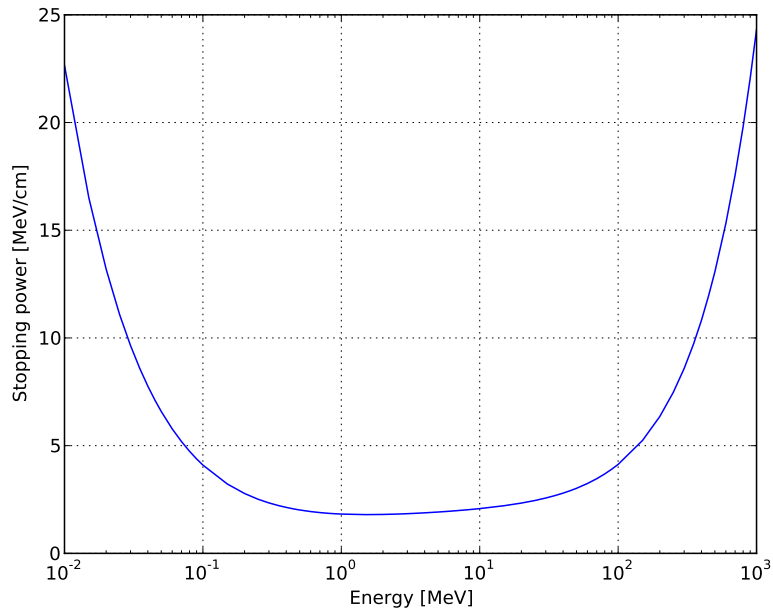


Figure 2.2.: Electron stopping power for Vinyltoluene [Ber+05].

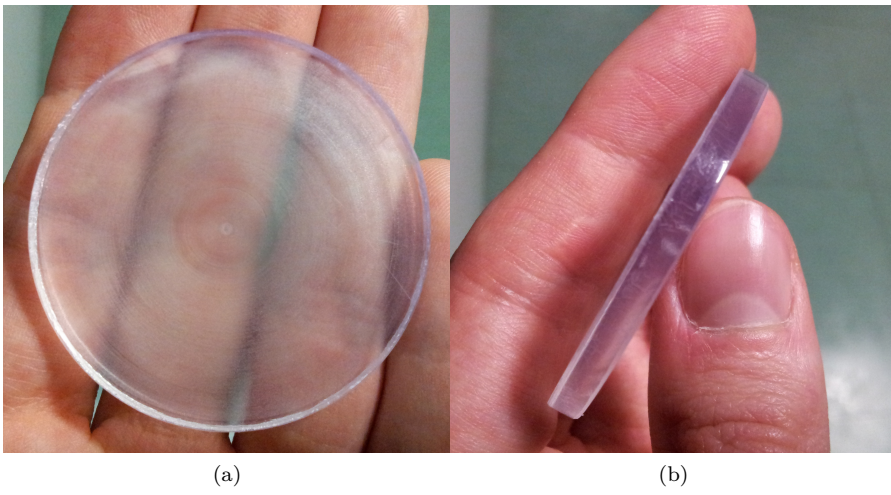
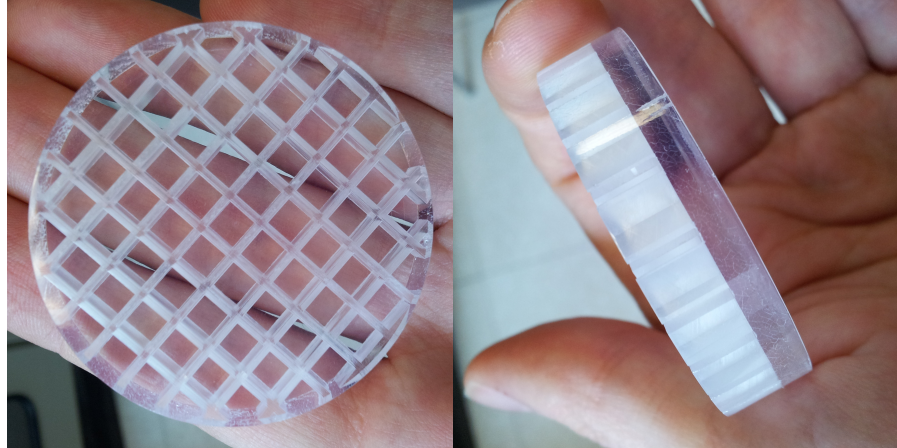
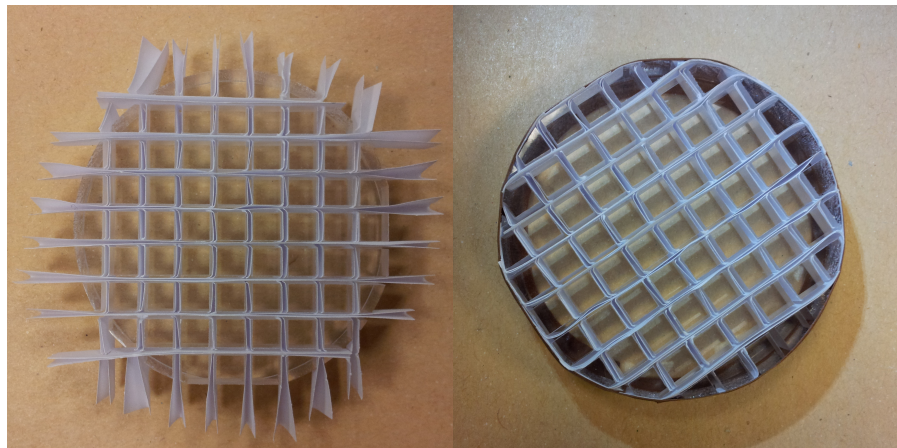


Figure 2.3.: Continuous 4 mm thick plastic scintillator.



(a) Front

(b) Side



(c) Pieces of white paper were inserted.

(d) Enclosed in tape.

Figure 2.4.: Segmented 12 mm thick plastic scintillator.



Figure 2.5.: Continuous 4 mm  $\text{LaBr}_3$  scintillator, damages and breaks are easily visible.

similar of water ( $1.032 \text{ g/cm}^3$ ) and a refractive index of 1.58. The light rise time is about 1 ns, the decay time is about 2 ns, and the wavelength of maximum emission is about 420 nm.

We had two options for this scintillator

- a 4 mm thick continuous round piece, polished on one side, diameter 5 cm (Figure 2.3 on page 15);
- a 12 mm thick segmented round piece, diameter 5 cm, machined in our laboratory (Figure 2.4 on the facing page).

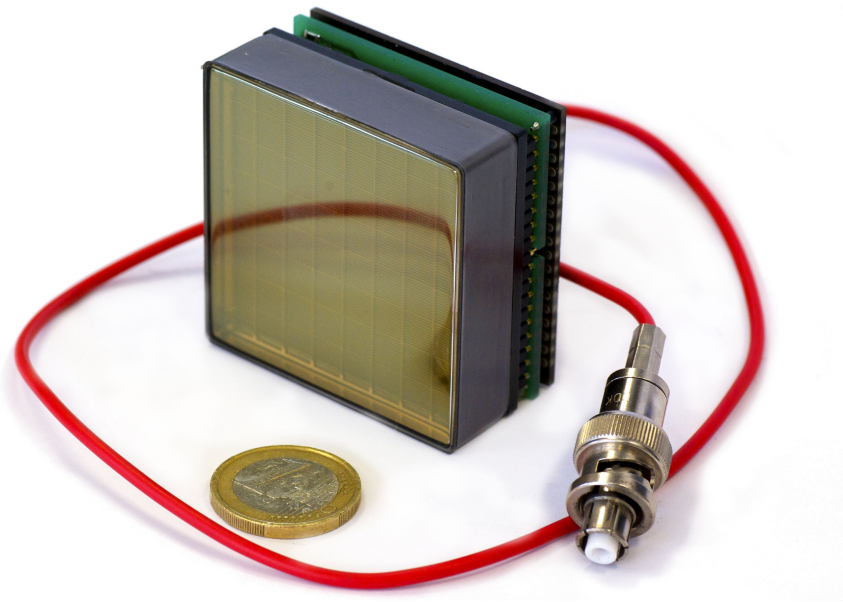
The segmented scintillator was obtained by a continuous piece (Figure 2.4 on the preceding page). The piece that was cut, but not for its whole thickness, and pieces of white paper were inserted in between the pillars, in order to reflect light. The single pillars are  $4 \text{ mm} \times 4 \text{ mm}$  wide.

### 2.1.2. Calorimeter

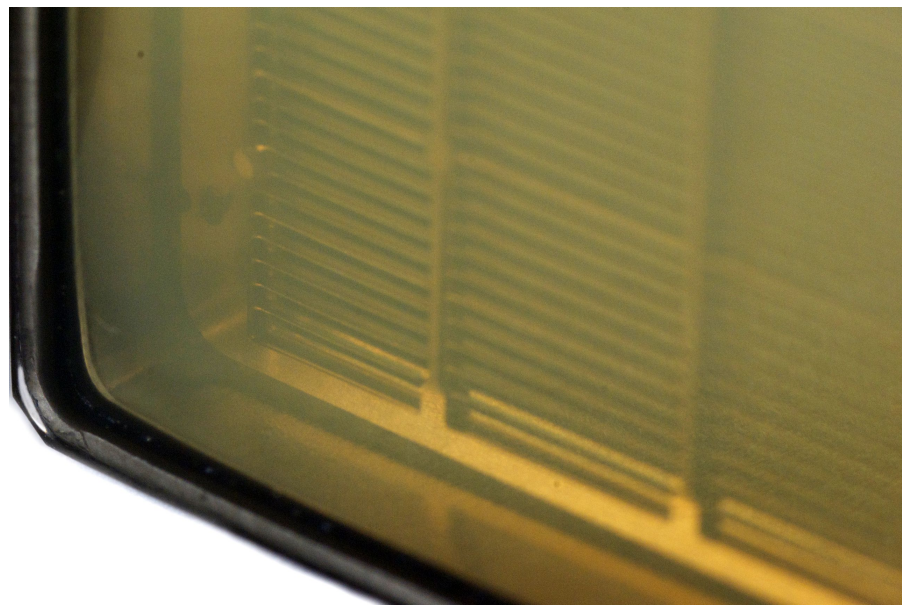
As the Calorimeter scintillator we used a continuous  $\text{LaBr}_3$  inorganic scintillator [Loe+02]. The decay time is 30 ns and the wavelength of maximum emission is 350 nm. The scintillator, 4 mm thick, is enclosed in an aluminium case with a glass window of 3 mm. In figure 2.5 we can see a picture of the scintillator, unfortunately it has visible damages and breaks that affect the image quality. Artifacts on the right of the uniformity calibration image, in figure 7.4 on page 81, are probably due to the breaks of the crystal.

## 2.2. Photomultiplier

The chosen photomultiplier for this work is the Hamamatu 10966, a modern variant of the Hamamatsu 8500, that is a flat-panel multianode position sensitive photomultiplier. It guarantees a sub-millimeter spatial resolution, a small



(a)



(b) Zoom of the internal metal dynodes and front glass.

Figure 2.6.: Hamamatsu 8500 Photomultiplier.



dead-area (11%), good spatial and energetic linearity and high gain ( $3.3 \cdot 10^5$ ) [Pan+04; H10; Fig+05]. It has a square area of  $52 \text{ mm} \times 52 \text{ mm}$  (effective area  $49 \text{ mm} \times 49 \text{ mm}$ ) and a  $8 \times 8$  multianode matrix (6.08 mm stride). There are 8 dynode stages and the last dynode provides an output that produces a fast signal for triggering. Maximum high voltage supply is 1100 V. The sensibility range is from 300 nm to 650 nm.

## 2.3. Readout Electronics

The Hamamatsu 8500 offers 64 analog output channels, there are different solutions that can be used for the readout

- channel number reduction with resistor networks [Olc+05; PM06];
- channel multiplexing [Ros+11a];
- parallel amplification and digitization [CND07].

For simplicity and development costs we decided to follow the first approach, *id est* to reduce the number of analog channels by connecting them with a resistor network. There are different topologies that can be applied, we opted for the charge multiplexing circuit of [Olc+05] as we will see in chapter 5 on page 45.



## 3. Image Reconstruction

We propose the use of an innovative technique in which the direction of gamma-rays is not selected by physical means, but it is measured by analyzing the Compton interactions of the photons [Fon+11; Ros+11a]. The concept of a Compton camera was first proposed in [TNE74]. The lack of a collimator guarantees a higher statistics and thus shorter acquisition times [SHR99; Par00]. The analysis of Compton scattering events leads to the deduction of the scattering angle and thus an indication of the gamma incoming direction. This is sometimes called *electronic collimation* [DS82; BS90; HLS90; Sin83].

### 3.1. Compton Interaction

The Compton Interaction was firstly explained by Arthur Compton [Com23] as an elastic interaction between a photon and a free electron at rest (diagram in figure 3.1 on the next page). A photon of energy  $E$  collides with an electron of an atom and it is subsequently scattered, with a new energy  $E'$  and a deviation angle  $\Theta$  that are bound by the formula:

$$\frac{1}{E'} - \frac{1}{E} = \frac{1 - \cos \Theta}{m_e}, \quad (3.1)$$

where  $m_e$  is the electron mass ( $c = 1$ ). From equation (3.1) on this page it is easy to calculate the transferred energy to the electron:

$$E_e = E - E' = E - \frac{m_e E}{(1 - \cos \Theta) E + m_e} \quad (3.2)$$

and then deduce the maximum of such energy:

$$E_e^{\max} = \frac{2 E^2}{2 E + m_e}. \quad (3.3)$$

Solving for the scattering angle we have

$$\Theta = \arccos \left( 1 - \frac{m_e}{E'} + \frac{m_e}{E} \right) \quad (3.4)$$

The interaction cross section was later found by Oskar Klein and Yoshio Nishina [KN28], it can be expressed in a convenient notation as in [Wei95]:

$$\frac{d\sigma}{d\Omega} = \frac{r_0^2}{2} \left( \frac{E'}{E} \right)^2 \left[ \frac{E'}{E} + \frac{E}{E'} - \sin^2 \Theta \right], \quad (3.5)$$

where  $r_0 = 2.818 \times 10^{-13}$  cm is the so called *classical electron radius*.

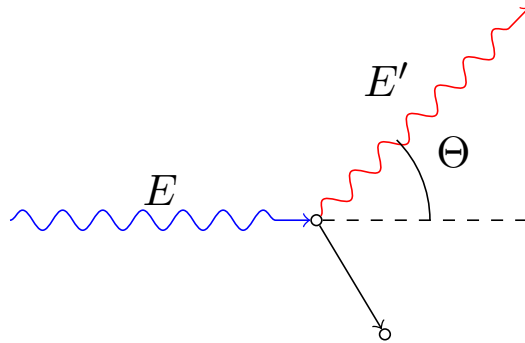


Figure 3.1.: A photon of energy  $E$  interacts with an electron and is scattered by an angle  $\Theta$  with an energy  $E'$ .

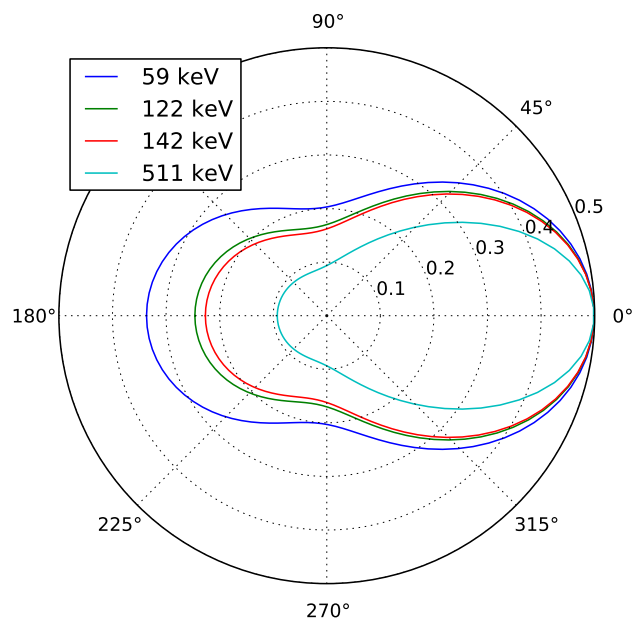


Figure 3.2.: Dependency of Compton cross section on the scattering angle, at some significant energies, from equation (3.5) on the preceding page.

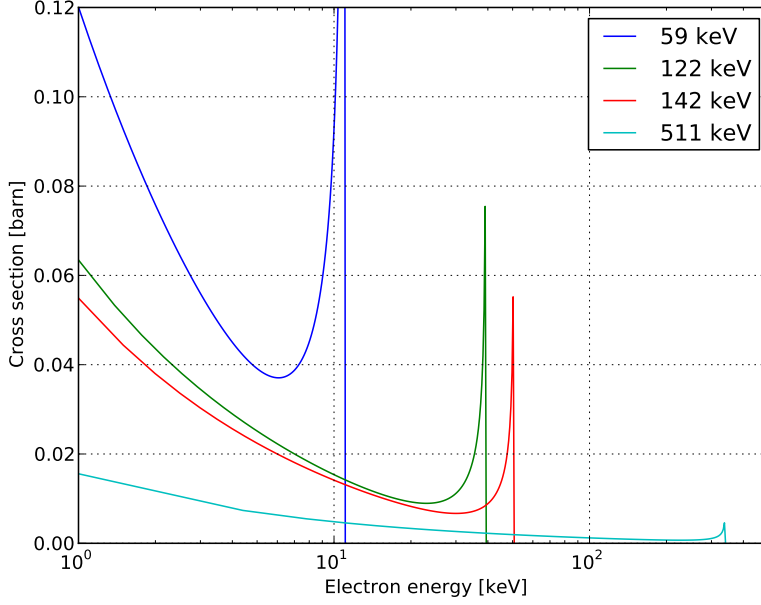


Figure 3.3.: Spectra of recoiling electrons from Compton interactions, at some significant energies, from equation (3.8) on the current page.

### 3.2. Released energy spectrum

To understand the spectrum of the electron energy we can use equations 3.1 and 3.5. If the electron can not escape the sensitive part of the detector, the measured spectrum is proportional to the interaction cross section and we can deduce its formula. Let us calculate the derivative of the electron energy in respect to the scattering angle

$$\frac{dE_e}{d\Theta} = \frac{d(E - E')}{d\Theta} = \frac{m_e E^2 \sin \Theta}{[(1 - \cos \Theta) E + m]^2}. \quad (3.6)$$

Integrating over the azimuthal angle we isolate the dependency of the cross section on only the scattering angle

$$\frac{d\sigma}{d\Theta} = \int_0^{2\pi} d\varphi \frac{d\sigma}{d\varphi d\Theta} = \pi r_0^2 \left(\frac{E'}{E}\right)^2 \left[\frac{E'}{E} + \frac{E}{E'} - \sin^2 \Theta\right] \quad (3.7)$$

and we can finally deduce the spectrum formula

$$\frac{d\sigma}{dE_e} = \frac{d\sigma}{d\Theta} \frac{d\Theta}{dE_e} = \pi r_0^2 \left(\frac{E'}{E}\right)^2 \left[\frac{E'}{E} + \frac{E}{E'} - \sin^2 \Theta\right] \cdot \frac{[(1 - \cos \Theta) E + m]^2}{m_e E^2 \sin \Theta}. \quad (3.8)$$

In figure 3.3 there are the spectra plotted at some significant energies.

### 3.3. Angle uncertainty

Being the measurement of the scattering angle the crucial point for the image reconstruction process, let us study its uncertainty and its dependence from the measured parameters assuming that the initial gamma energy  $E$  is well known. Using the formula of propagation of uncertainties [Ku66]

$$\sigma_f^2 = \sum_{i=0}^n \left[ \frac{\partial f}{\partial x_i} \right]^2 \sigma_{x_i}^2. \quad (3.9)$$

where  $f : \mathbb{R}^n \rightarrow \mathbb{R}$ . Using equation (3.4) on page 21 we have

$$\frac{\partial \Theta}{\partial E_e} = \frac{m_e}{(E')^2} \frac{1}{\sqrt{1 - \left[1 - \frac{m_e}{E'} + \frac{m_e}{E}\right]^2}}, \quad (3.10)$$

which in absolute value is equal to the partial derivative in respect to the final energy  $E'$ , and thus

$$\sigma_{\Theta} = \left| \frac{\partial \Theta}{\partial E_e} \right| \sigma_{E_e} = \frac{m_e}{(E - E_e)^2} \frac{\sigma_{E_e}}{\sqrt{1 - \left[1 - \frac{m_e}{E - E_e} + \frac{m_e}{E}\right]^2}}. \quad (3.11)$$

that is the angle uncertainty that we would get using the measure of the recoiling electron energy. In figure 3.4 on the next page there is a plot of angle uncertainties depending on the electron energy and relative error. If we use the measurement of the final gamma energy we would have a similar formula

$$\sigma_{\Theta} = \left| \frac{\partial \Theta}{\partial E'} \right| \sigma_{E'} = \frac{m_e}{(E')^2} \frac{\sigma_E}{\sqrt{1 - \left[1 - \frac{m_e}{E'} + \frac{m_e}{E}\right]^2}}. \quad (3.12)$$

We see that, in principle, using the measurement of one energy or the other is just a matter of which would be the most precise measurement. Although in [OBC97] it is shown that, due to Doppler effects of low energy gamma-rays, it is more important to have a high precision Calorimeter.

### 3.4. Compton cones

With out experimental set-up we are able to measure the gamma-rays direction after the Compton interaction, the electron energy and the final energy of the gamma. With only these parameters the exact incoming direction of the gamma can not be defined, but only a set of possible directions (Figure 3.5 on page 26). Defining the measured parameters as

$$\text{Tracker: } (x_t, y_t, E_t) \quad \text{Calorimeter: } (x_c, y_c, E_c) \quad (3.13)$$

where the coordinates are in the local coordinate system of the detectors. Let us convert the tracker local coordinates in global coordinates

$$(x_t, y_t) \mapsto R^{-1}(\alpha_t, \beta_t, \gamma_t)(x_t, y_t, 0) + (X_t, Y_t, Z_t) = \vec{x}_t, \quad (3.14)$$

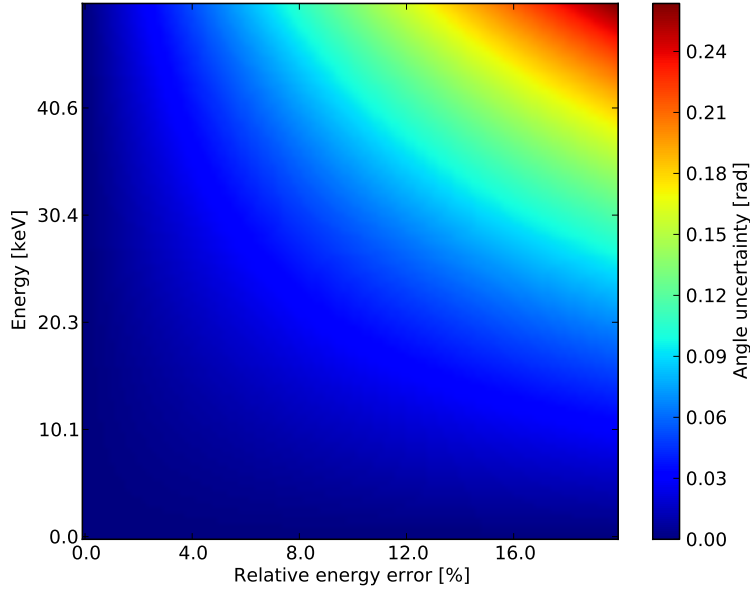


Figure 3.4.: Angle uncertainties for a gamma-ray of 142 keV, plotted against the electron energy  $E_e$  and the measurement relative error.

where  $(\alpha_t, \beta_t, \gamma_t)$  are the Euler angles of the detector rotation and  $(X_t, Y_t, Z_t)$  is the detector position, and similarly

$$(x_c, y_c) \mapsto R^{-1}(\alpha_c, \beta_c, \gamma_c)(x_c, y_c, 0) + (X_c, Y_c, Z_c) = \vec{x}_c. \quad (3.15)$$

Let us define the photon outgoing direction as

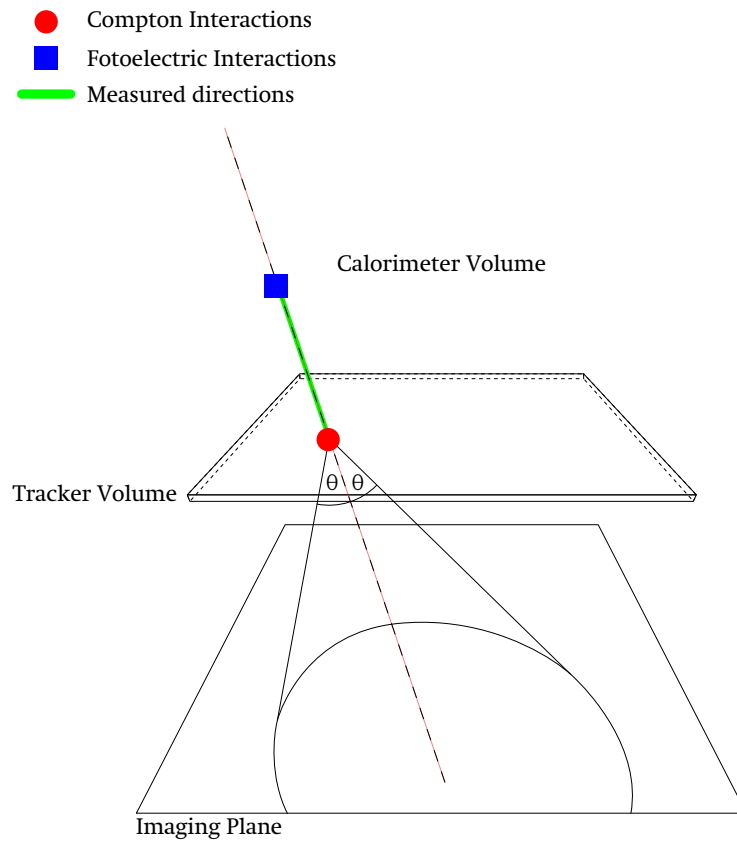
$$\vec{d} = \vec{x}_t - \vec{x}_c. \quad (3.16)$$

Supposing to have a Compton interaction on the origin of the coordinates system what we know are  $\vec{d}$  and  $\Theta$  that are bounded by the equation

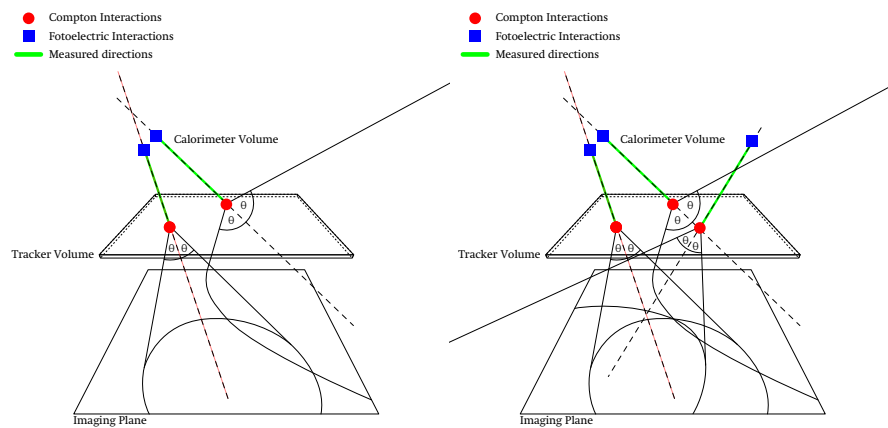
$$\vec{u} \cdot \vec{d} = \|\vec{u}\| \|\vec{d}\| \cos \Theta \quad (3.17)$$

where  $\vec{u}$  is the incoming direction of the gamma, this equation tells us that the angle between  $\vec{d}$  and  $\vec{u}$  is  $\Theta$  and thus satisfies the interaction geometry. For us, though,  $\vec{u}$  is the unknown variable so equation (3.17) actually describes a conical surface [Can96] with the vertex on the Compton interaction position (Figure 3.5 on the next page and figure 3.6 on page 27). To univocally determine the source position the intersection of at least three cones is necessary. We can modify equation (3.17) in order to define a function that has a level set corresponding to the locus of possible incoming directions

$$S : \mathbb{S}^2 \rightarrow \mathbb{R}, \quad S(\hat{u}) = \hat{u} \cdot \hat{d} - \cos \Theta \quad (3.18)$$



(a) Definition of a Compton Cone and its intersection with the imaging plane



(b) The intersection of two cones defines two possible source positions

(c) The intersection of three cones defines the source position

Figure 3.5.: Compton cones obtained by the scattering direction and scattering angle.



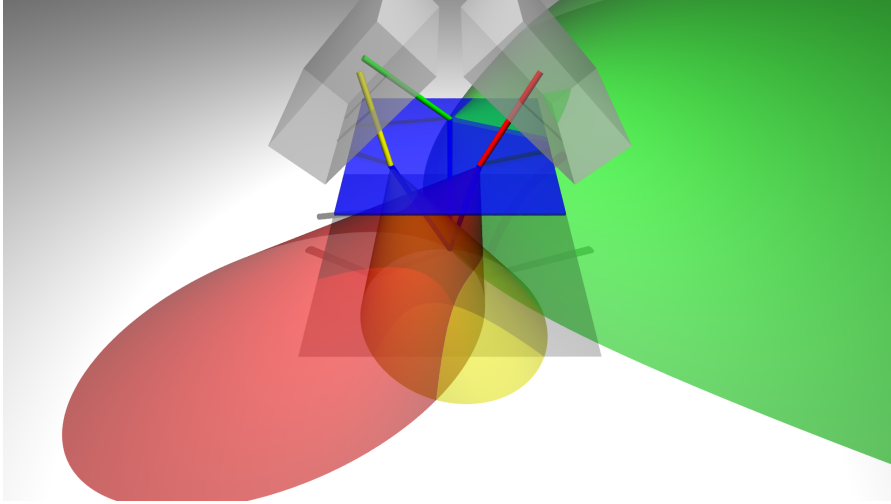


Figure 3.6.: POV-ray [Pov] simulation of the intersection of three Compton cones.

where  $\hat{d}$  is the unit vector parallel to  $\vec{d}$

$$\vec{d} = \frac{\vec{x}_t - \vec{x}_c}{\|\vec{x}_t - \vec{x}_c\|} \quad (3.19)$$

and  $\mathbb{S}^2$  is the unit sphere centered on the origin. We can reduce our problem domain to  $\mathbb{S}^2$  because we are interested in the directions of the vectors and not on their modulus. For convenience we used spherical coordinates centered on the Compton event with the following convention

$$\begin{cases} x &= r \cos(\theta) \cos(\varphi) \\ y &= r \sin(\theta) \cos(\varphi) \\ z &= r \sin(\varphi) \end{cases} \quad (3.20)$$

where  $\varphi \in [-\pi/2, \pi/2]$ ,  $\theta \in [0, 2\pi]$ . Obviously the roots of the function  $S(\cdot)$  are the solution of equation (3.17) and thus give all the possible incoming directions for each event. We can imagine the equation

$$S(\hat{u}) = 0 \quad (3.21)$$

as an equation of an intersection between the cone, described by equation (3.17), and a unity sphere centered on the cone vertex. On the spheres such intersections are circles, but not great circles as the cone aperture is arbitrary (Figure 3.7 on the next page).

### 3.4.1. Numerical solutions of $S(\hat{u}) = 0$

To determine the root locus of  $S(\cdot)$  a numerical algorithm was developed that searches in a mesh of values of  $\theta$  and  $\varphi$ , which are the two spherical

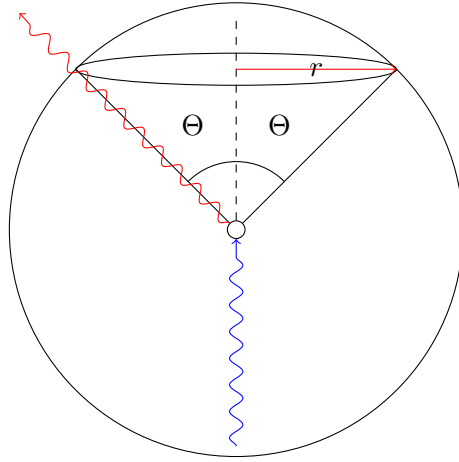


Figure 3.7.: Intersection between the unit sphere and the Compton cone, the real photon path is drawn and the radius of the intersection circle.

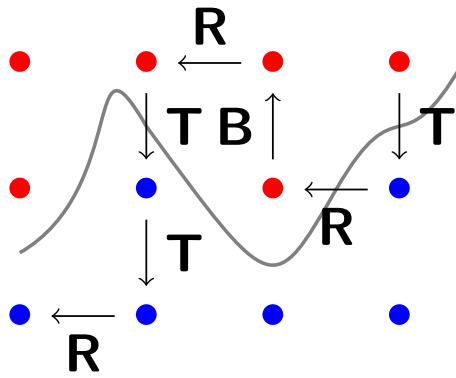


Figure 3.8.: Locus of  $S(\hat{u}) = 0$  on a  $(\theta, \varphi)$  bidimensional mesh; red dots show positive values of the function, while blue dots show negative values. Arrows indicate the algorithm path on the mesh, with labels indicating the preceding step kind.

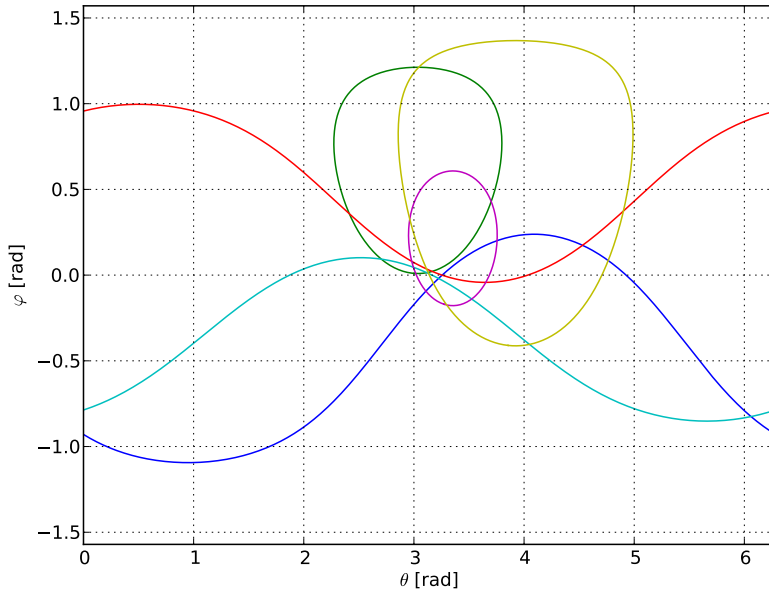
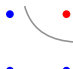

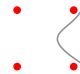


Figure 3.9.: Examples of locuses of  $S(\hat{u}) = 0$  on a  $(\theta, \varphi)$  bidimensional mesh.

coordinates that describe a unit vector in  $\mathbb{S}^2$ . A requirement for the algorithm was the elaboration speed, since it has to look for the zeros on  $\mathbb{S}^2$  for each Compton event, and the interaction rate can be rather high depending on the experimental set-up. Therefore an optimized C software was written to travel through the mesh of  $(\theta, \varphi)$  values tracing the root locus (Figure 3.8 on the facing page). The calculation requires frequent computations of sines and cosines for each mesh point, thus look-up tables are defined at the start-up of the program for sines and cosines of the possible values of  $\theta$  and  $\varphi$ . On the  $(\theta, \varphi)$  plane the cones do not look like circles as in  $\mathbb{S}^2$  but can have different kind of shapes, like closed ellipse-like shapes or sinusoidal lines (Figure 3.9).

As a first step the algorithm starts to pass through each line along the  $\theta$  dimension and compares the sign of subsequent mesh point, when it finds a sign changing pair it stops and uses that as the starting point of the root locus tracing. From now on the algorithm considers not pairs of points but squares of four points. There can be three possible cases:

1.  the root locus enters from one side of the square and exits from the adjacent side;
2.  it enters from one side and exits from the opposite side;

3.  it enters from one side and exits from the same side;

the third case is trivial because all the corners have the same sign and thus the algorithm ignores it. To follow the root locus the algorithm has the memory of the preceding step type:

**T**: the algorithm moved to the square underneath;

**B**: it moved to the top;

**L**: it moved to the right;

**R**: it moved to the left.

The algorithm starts toward the left side of the root locus with the following rules (Figure 3.8 on page 28):

- if the preceding step was not a **B** step and the locus passes through the bottom it goes down;
- if the preceding step was not a **T** step and the locus passes through the top it goes up;
- if the preceding step was not a **L** step and the locus passes through the left it goes left;
- if the preceding step was not a **R** step and the locus passes through the right it goes right;
- if none of the above it raises an exception because the root locus disappeared inside the square.

When the algorithm reaches a mesh boundary it stops and starts again from the first zero but going toward the right side, with an analogous set of rules. If the algorithm reaches the starting zero it completely stops because it followed a closed trajectory.

This algorithm was implemented in order to produce evenly-spaced dots on the  $(\theta, \varphi)$  plane, for instance a similar algorithm from the Octave standard library gives roots that are not evenly spaced and thus can generate artifacts on the final reconstructed image (Figure 3.10 on the next page).

### Algorithm run-time

The worst case scenario for this algorithm is a wide sinusoidal-like root locus that can cover the entire extent of the  $\theta$  and the  $\varphi$  domains, while the best scenario is a very small closed root-locus to the limit of being one square wide. The former can be a great circle passing near the poles, while the latter is a forward scattering with a very small change in the energy. In the worst case scenario the algorithm has to travel from, let us say, the upper left corner of the  $(\theta, \varphi)$  mesh ( $\varphi = \frac{\pi}{2}$ ) then go, while traveling on  $\theta$ , all the way down to the bottom ( $\varphi = -\frac{\pi}{2}$ ) and then up again toward the upper right corner

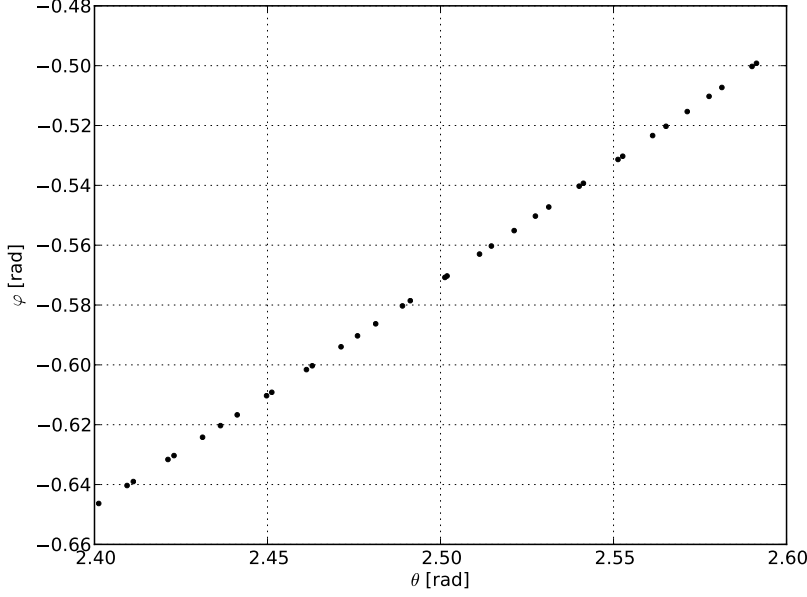


Figure 3.10.: Zoom of roots of  $S(\cdot)$  obtained with an algorithm from the Octave standard library.

( $\varphi = \frac{\pi}{2}$ ). In this scenario the algorithm covers the whole extent of  $\varphi$  twice and the extent of  $\theta$  once, therefore if we take a mesh spacing  $\delta$  equal for the two angles we would have

$$N_\varphi = \frac{\Delta\varphi}{\delta} = \frac{\pi}{\delta} = N, \quad N_\theta = \frac{\Delta\theta}{\delta} = \frac{2\pi}{\delta} = 2N \quad (3.22)$$

so the run-time for each Compton event  $T(\cdot)$  would be

$$T(n, N) \propto (2 \cdot N_\varphi + N_\theta) \cdot n = 4N \cdot n \quad (3.23)$$

where  $n$  is the number of Compton events that are to be analyzed, thus

$$T(n, N) \in O(n \cdot N). \quad (3.24)$$

We can imagine the mesh as a staircase that is traveled by the algorithm once downward and once upward: it does not cover a submesh of points but only a line, therefore it is an error to think that the run-time would be the product  $n \cdot N_\theta \cdot N_\varphi$ . In figure 3.11 on the following page we can see the dependence of the execution times per reconstructed cone on the parameter  $N_\theta$  that is roughly linear; the tests were performed on an Intel<sup>®</sup> Core<sup>™</sup> i5-3570K CPU @ 3.40 GHz.

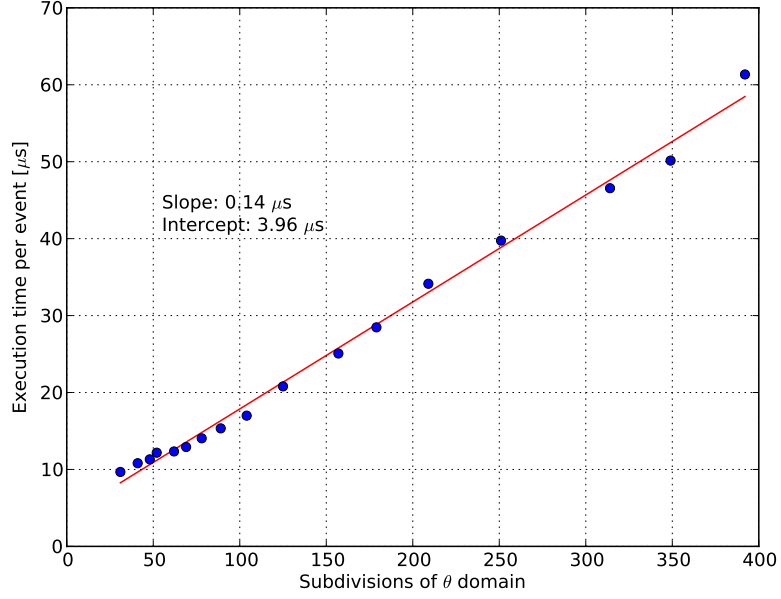


Figure 3.11.: Execution times per reconstructed cone at different levels of subdivisions of the  $\theta$  domain.

### 3.4.2. Cone Weighting

Since cones can lead to intersections that can be of different sizes and thus bring different global contributions to the final image, a weighting is necessary. The radius of the circles is simply (Figure 3.7 on page 28):

$$r = \sin \Theta \quad (3.25)$$

therefore the circumference length is

$$l = 2\pi \sin \Theta. \quad (3.26)$$

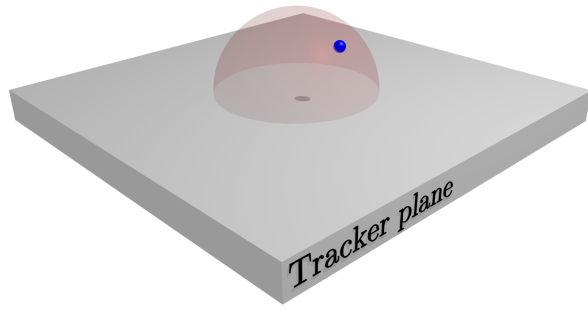
Another weighting factor comes from the Klein-Nishina formula, equation (3.5) on page 21, since smaller aperture Compton events are more likely to happen their weight on the final image would be enhanced.

The weighting factor of each cone is then

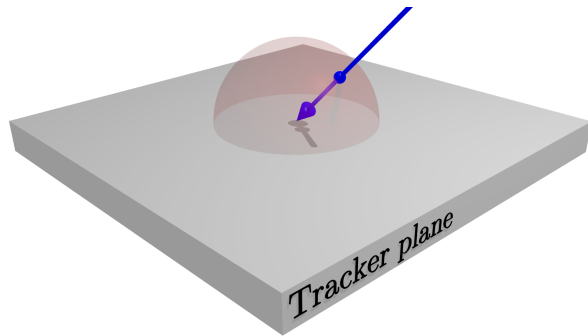
$$w = \frac{1}{l \cdot \frac{d\sigma}{d\Omega}(E, E')}. \quad (3.27)$$

## 3.5. Image generation

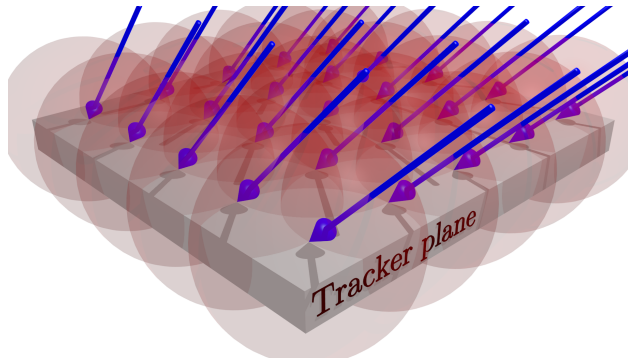
To reconstruct the images, a four-dimensional histogram is filled with the cones together with the Compton interaction positions. A trivial bidimen-



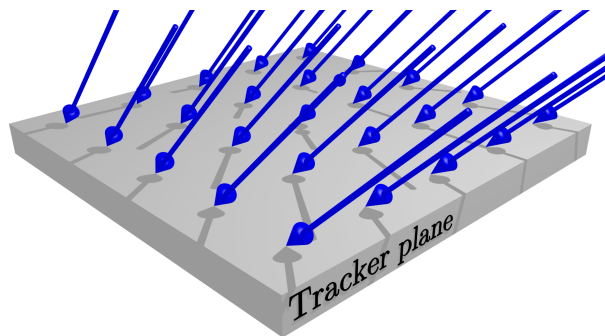
(a) Selected  $(\theta^*, \varphi^*)$  on the unit sphere centered on the Tracker center.



(b) Defined projector for the selected  $(\theta^*, \varphi^*)$ .



(c) Unit spheres centered on various Tracker points and their projectors.



(d) Projectors from each of the spheres.

Figure 3.12.: Projections on the tracker plane of the four-dimensional histogram  $h(\cdot)$ .

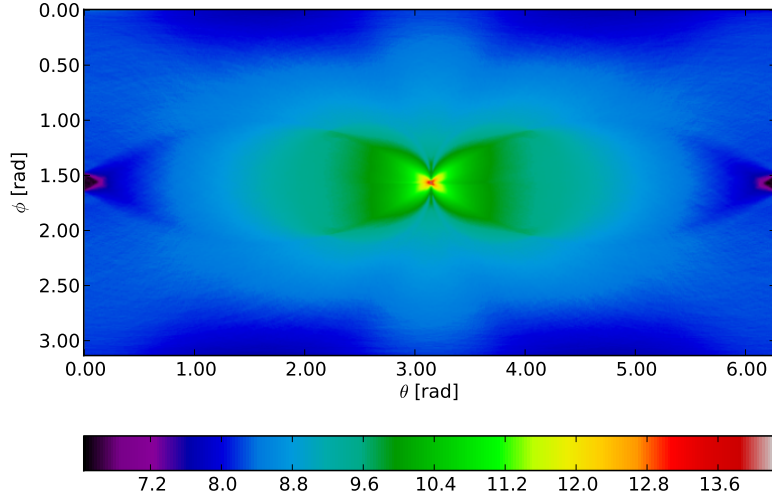


Figure 3.13.:  $(\theta, \varphi)$  space associated to the simulation of the Point Spread Function (the color scale represents the logarithm of the actual counts).

sional plot of  $(\theta, \varphi)$  is not sufficient for our application since the source-detector distance and the object dimensions are comparable to the detector characteristic dimension, thus a bidimensional histogram, like that, would introduce parallax errors in the images. We are required to take into account the extension of the detector. In our case we decided to use the Tracker as a reference frame for our images, because the Compton interactions occur on its volume and therefore the calculations are easier. The histogram is a function  $h : \mathbb{R}^4 \rightarrow \mathbb{R}$  that gives the frequency of each  $n$ -tuple of coordinates:

$$(\theta, \varphi, x_t, y_t) \mapsto h(\theta, \varphi, x_t, y_t). \quad (3.28)$$

where  $(x_t, y_t)$  are the coordinates of the Compton events. Each reconstructed cone is histogrammed weighted by the factor  $w$ , of equation (3.27).

What do  $(\theta, \varphi)$  couples represent? Choosing a position on the unit sphere can be interpreted as a choice of direction of projection, or better, a projector could be defined that projects the images along the direction that joins the center of the sphere and the particular couple  $(\theta^*, \varphi^*)$  selected (Figure 3.12 on the previous page). With this technique we can define an image as

$$g(x, y) := h(\theta^*, \varphi^*, x, y). \quad (3.29)$$

and we see that from a single acquisition multiple views of the object can be extracted: one for each  $(\theta, \varphi)$  pair. In figure 3.14 on the facing page we



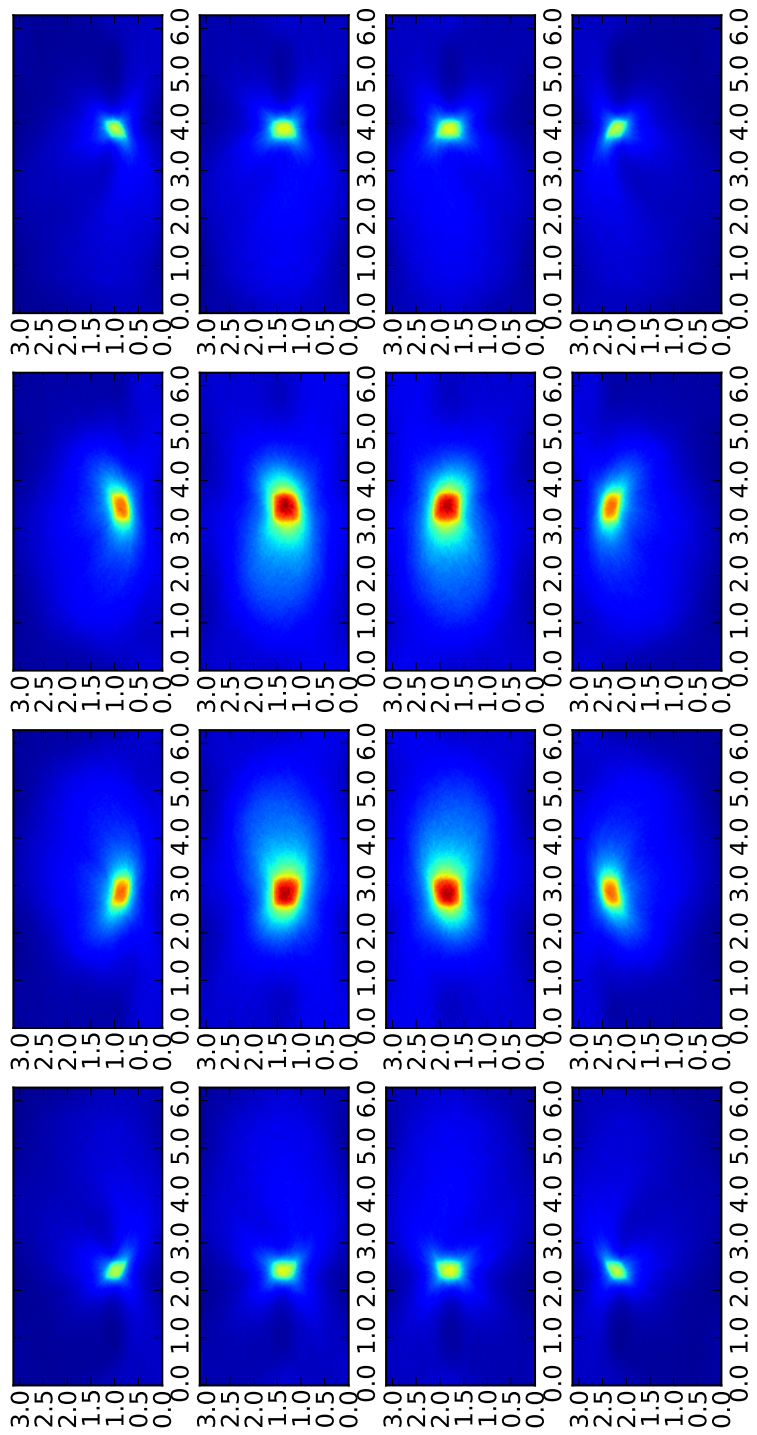
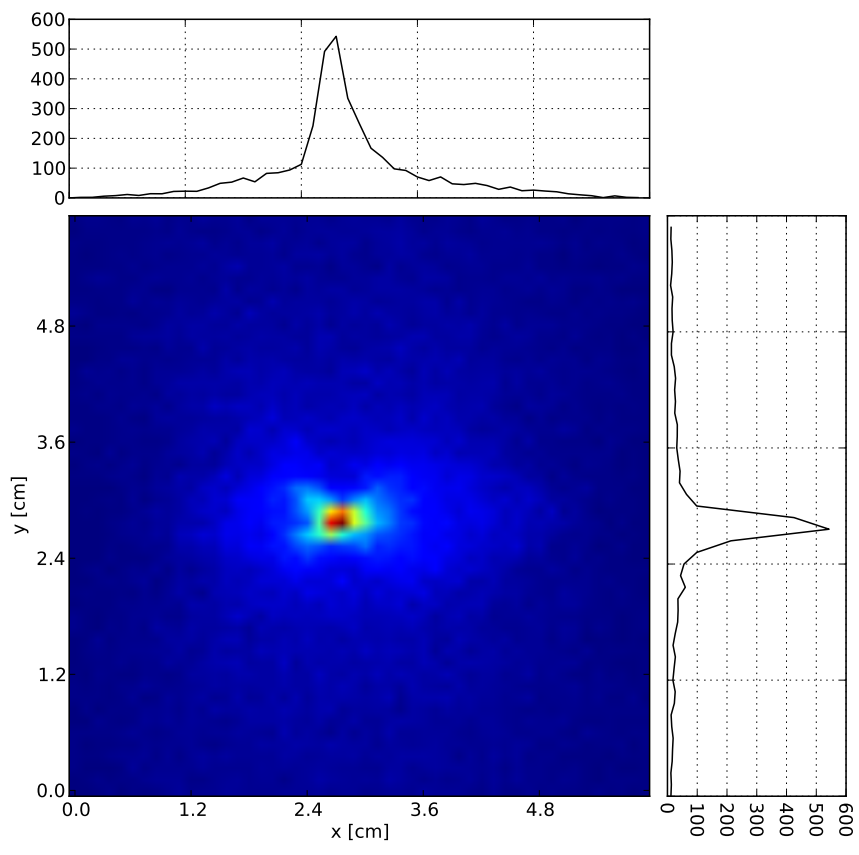


Figure 3.14.: Simulations of  $(\theta, \varphi)$  spaces associated to different subdivisions of the Tracker for a point-like source.

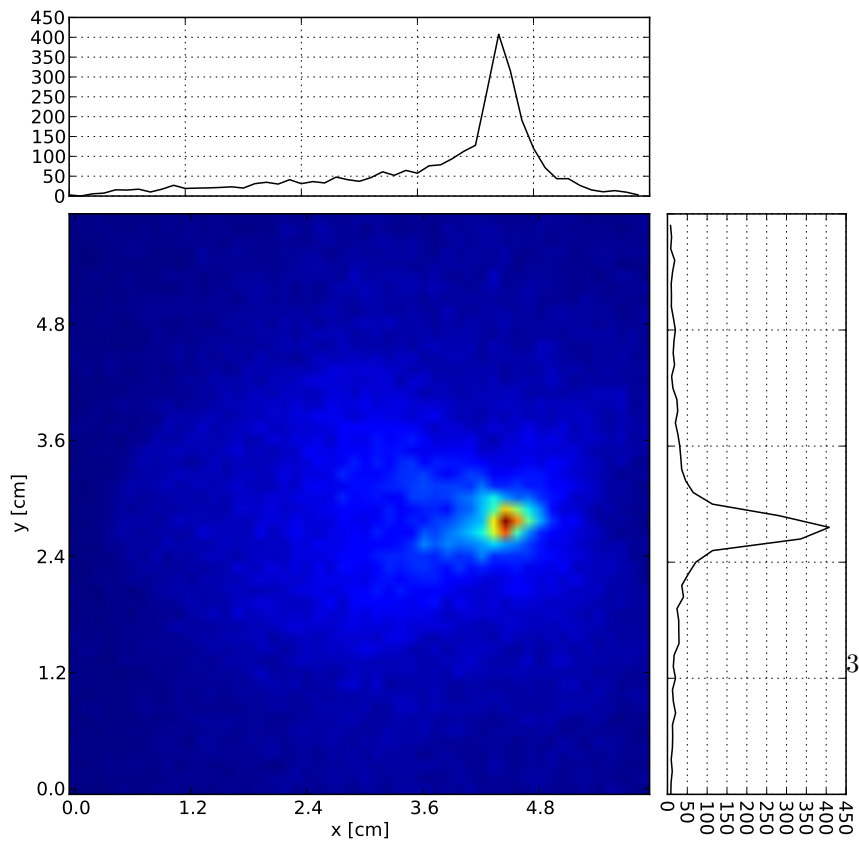
can see a simulation of a point-like source 2.5 cm from the detector: what is pictured are the  $(\theta, \varphi)$  spaces that are associated to a piece of a subdivision of the Tracker in  $4 \times 4$  pieces.

The downside of this approach is that the image resolution on the Tracker and the angular resolution depend on the histogram dimensions. For instance a 1 mm subdivision on a  $5 \text{ cm} \times 5 \text{ cm}$  Tracker gives us a  $50 \times 50$  mesh; an angular resolution of about 0.05 rad gives us a  $64 \times 128$  mesh (such angular resolution is the acceptance angle of a lead collimator used in our lab). The histogram is constituted by double precision floating point numbers, that are 8 B (byte) wide on the used architectures (Darwin Kernel 10.8.0 on XNU-1504.15.3 i386 and GNU/Linux Kernel 3.2.0-35-generic x86\_64), therefore the histogram size is  $50 \times 50 \times 64 \times 128 = 20480000$  bins which occupy about 156 MiB. The size goes as the inverse squared of the resolutions, so it can grow very quickly.

In figures 3.15 on the next page and 3.16 on page 38 there are some examples of a simulation of a point-like source projected on the Tracker plane along different directions. The source is 2.5 cm from the detector and  $1.3 \cdot 10^6$  Compton events were simulated. The reconstruction resolution on the Tracker plane is 1 mm, the angular resolution is 0.05 rad. The image shows a variable resolution depending on the position on the detector, at the center the Full Width at Half Maximum (FWHM) is about 2 mm on the  $y$  direction and 4 mm on the  $x$  direction, on the sides the overall FWHM is about 4 mm. The difference on the resolution magnitude is due to the position of the Calorimeter compared to the Tracker position, in this simulation the Calorimeter was orthogonal to the Tracker and on its left side.

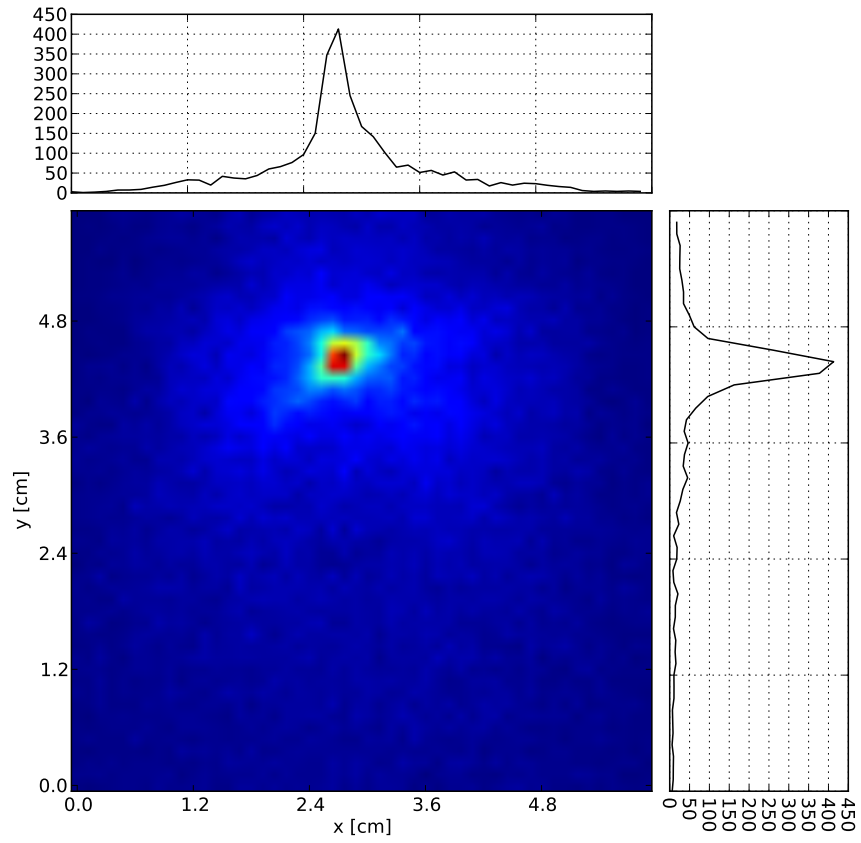


(a)  $(\theta^*, \varphi^*) = (\pi, 0)$

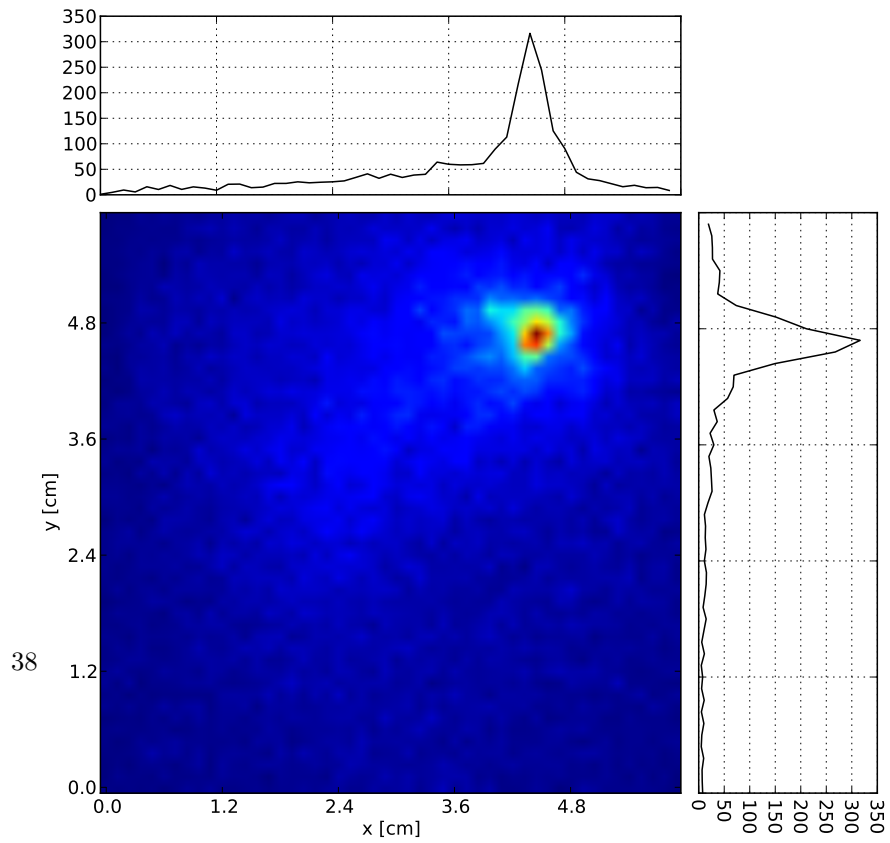


(b)  $(\theta^*, \varphi^*) = (6\frac{\pi}{5}, 0)$

Figure 3.15.: Example image of a simulation of a point-like source projected on the Tracker plane, source distance 2.5 cm, image reconstruction



(a)  $(\theta^*, \varphi^*) = (\pi, \frac{\pi}{5})$



(b)  $(\theta^*, \varphi^*) = (6\frac{\pi}{5}, \frac{\pi}{5})$

Figure 3.16.: Example image of a simulation of a point-like source projected on the Tracker plane, source distance 2.5 cm, image reconstruction

## 4. Geant4 Simulation

A Geant4 [Ago+03; All+06] simulation of the apparatus was implemented to develop the image reconstruction software and assess the possible geometries. Geant4 is a Object-Oriented (OO) C++ development toolkit that is used for Monte Carlo simulation of the interaction of particles in matter. Geant4 users implement their own programs using the provided classes and methods, therefore users have a high level of freedom. What is required for a simulation to run are the following classes that describe a certain aspect of the experiment:

- **PhysicsList**: list of reactions that are to be simulated;
- **DetectorConstruction**: geometry description of detectors and apparatuses;
- **PrimaryGeneratorAction**: generator of particle beams or sources;
- **SensitiveDetector**: description of detector characteristics (one per detector kind);
- **Hit**: description of detected events (one per detector kind).

### 4.1. PhysicsList class description

Physics Lists are one of the most complex and sensitive subjects in Geant4 simulations. They describe the list of reactions that the user wants to be simulated in his software: a wrong choice in the Physics List leads to wrong and biased results. The fewer simulated processes, the fewer CPU resources are to be used. However a poor list can skip important reactions.

For our simulation we used the Geant4 Standard electromagnetic processes that are found in the Geant4 distribution itself, with the addition of the Livermore physics models **G4EmLivermorePhysics**. We were interested in very low energy processes because our range of gamma energies is from 122 keV ( $^{57}\text{Co}$ ) up to 142 keV ( $^{99m}\text{Tc}$ ) and at such low energies the Doppler effect becomes important for the Compton interaction [OBC97; ZK03].

### 4.2. DetectorConstruction class description

Two different kind of geometries were described in the **DetectorConstruction** class (Figure 4.1 on the next page)

- a “Forward” geometry in which the Tracker Photomultiplier is interposed between the Tracker scintillator and the source;

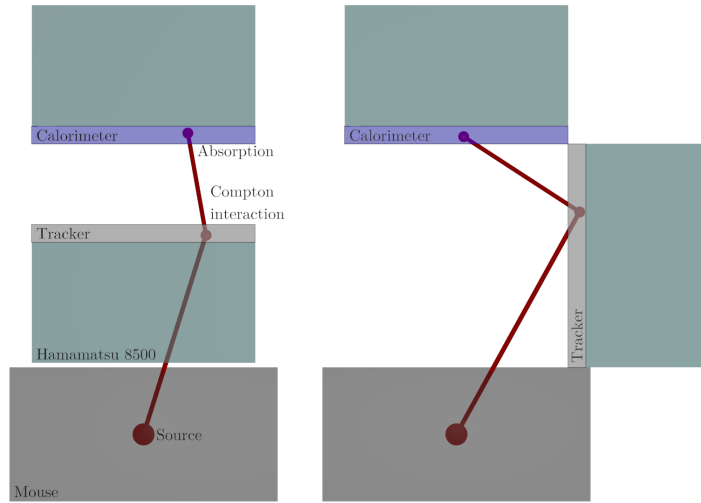


Figure 4.1.: Simulations geometries, the left one is called “Forward” geometry, the right one is called “Side” geometry.

- a “Side” geometry in which the Tracker is orthogonal to the Calorimeter and on the side.

. The Forward geometry has the advantage of detecting Compton events with smaller angles that, for equation (3.5) on page 21, have higher probabilities and give better images [OBC97]. However in this case the PMT partially absorbs the gamma-rays and its internal structures create artifacts. The Side geometry has the advantage of having clear paths for the gamma-rays, but higher Compton angles.

A mouse is simulated with a cylinder of tissue material, declared with the standard material `G4_TISSUE_SOFT_ICRP`. The Tracker scintillator is composed of Polyvinyltoluene, declared with the standard material `G4_PLASTIC_SC_VINYLTOLUENE`, and the Calorimeter scintillator is composed of  $\text{LaBr}_3$ , declared with a user defined material with the standard elements. Scintillators are simulated as `SensitiveDetectors` instances, which that are able to generate `Hit` instances whenever a release of energy in their volume occurs. The scintillation processes were left out from the simulation to spare elaboration time, they were simulated afterward with simple models (*id est* inserting a quantum efficiency and a energy resolution on the simulated data). The Hamamatsu 8500 are roughly simulated with a box of glass with the density equal to the PMT mean density, declared with the standard material `G4_Pyrex_Glass`.

### 4.3. PrimaryGeneratorAction class description

This is the class that is called to generate the gamma-rays using an instance of the `G4ParticleGun` class. The particle gun is a particle generator that cre-

ates particles with given energy and momentum. The energy can be generated with a fixed value, that corresponds to a monochromatic gamma-ray beam, or with a random energy that follows a distribution. The momentum direction can be generated as a fixed vector for collimated beams or as a random vector with an isotropic distribution for point-like sources.

#### 4.4. SensitiveDetector and Hit class descriptions

There are two classes `SensitiveDetector`, one for the Calorimeter and one for the Tracker, and they both take care of generating `Hit` instances whenever an energy deposit occurs inside the volume of the sensitive detector. `Hit` instances are objects that store the deposition position and the deposited energy and are collected in a `G4THitsCollection`, that is a container class for `Hit` instances.

#### 4.5. Trajectories

To store important parameters of the particle trajectories, a new trajectory class was written that inherits from the virtual class `G4VTrajectory`. A trajectory is a container of `G4VTrajectoryPoint`, that stores the positions of the particles and some more parameters depending on the user requests. In our case we wrote a class that inherits from the `G4VTrajectoryPoint` and stores the information on Compton interaction, as well as position, momentum and energy. Defining a `G4UserStackingAction` we were able to eliminate photons that interacted with parts that are not sensitive to spare calculation time.

#### 4.6. Actions

Also other kinds of auxiliary classes are used in the simulation, which are called Action classes. They describe actions that have to be taken by the program at certain execution stages. The `G4UserRunAction` describes actions that are to be taken at the beginning of a run of the simulation, for instance the program can start several runs with different parameters. We used that class to be able to initialize the random number generator with particular seeds in order to reproduce the same run with the same results.

The `G4UserEventAction` describes actions that are to be taken at the end of each event. This is a very important class because it can be used to extract the required information from the simulation. We used that class to:

- eliminate events that do not show a coincidence between the two scintillators;
- calculate the total released energy in the scintillators;
- calculate the interaction positions in the scintillators with an weighted mean;
- calculate the Compton scattering angle;

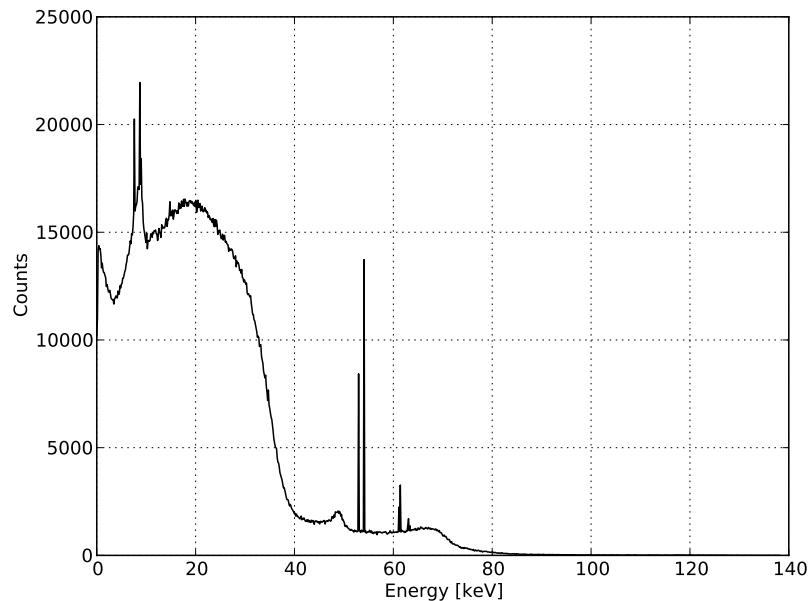


Figure 4.2.: Dependence of the scattering angle from the recoiling electron energy, obtained from the Geant4 simulations, the theoretical plot is superimposed on the data.

- calculate the recoiling electron path length.

## 4.7. Simulation results

The simulations were performed with a gamma-ray source of 142 keV, the characteristic emission energy of  $^{99m}\text{Tc}$ . Since we discovered that the Forward Geometry gives us 50% less events than the Side Geometry, we decided to implement the this latter, which features also a cleaner gamma-rays path. The produced images are described on chapter 3 on page 21. The conclusion was that the obtained resolution for a point-like source varies from 2 mm to 4 mm, which represent a unavoidable limit due to the Doppler Effect. In figure 4.3 on the facing page we can see a scatter plot showing the dependence of the scattering angle from the recoiling electron energy, obtained from our simulations, with the theoretical plot superimposed. We see that most of the events fall on the proximity of the theoretical line but there are events with electrons of energies up to 70 keV, that are 20 keV higher than the expected Compton edge of about 50 keV. In figure 4.2 we can see the Tracker spectrum that shows the classical Compton edge for gamma-rays of 142 keV at about 50 keV, but also a significant number of events with higher energies.



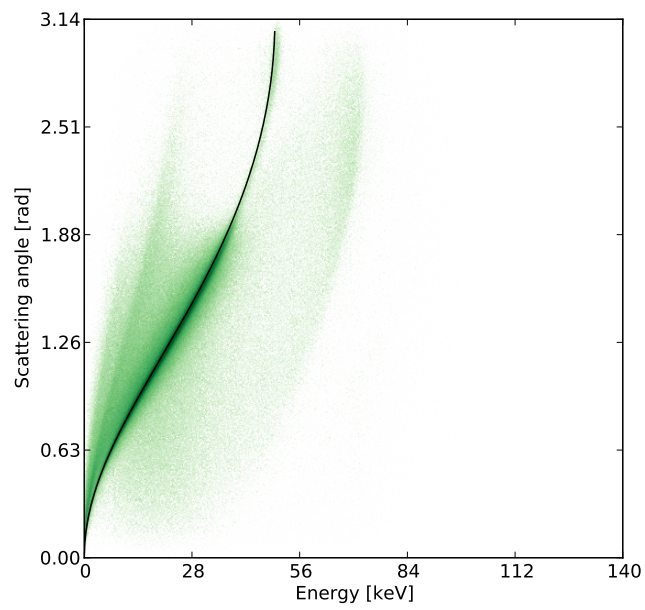


Figure 4.3.: Dependence of the scattering angle from the recoiling electron energy, obtained from the Geant4 simulations of 142 keV gamma-rays, the theoretical plot is superimposed.



## 5. Readout Electronics

### 5.1. Requirements

The usage of the Hamamatsu 8500 Multianode Photomultiplier is challenging because of the high number of analog channels that have to be acquired. This requires either one Analog to Digital Converter (ADC) per channel or some signal multiplexers and fewer ADCs. The former approach requires high investments, since ADCs are expensive, while the latter an accurate and complex electronics development. We decided to follow a cost-effective path and opted for a Charge Multiplexing Circuit, in which the yielded signals are combined by an analog circuit to reduce the overall number of analog channels [Sie+96; Olc+05].

Being PMTs current sources, the signals have to be integrated before being read by an ADC. Having reduced the number of signals we decided to use discrete circuits, instead of integrated circuits that offer many channels but also more complexity.

The chosen readout electronics can be seen in figure 5.1 on the following page, it consists of

- Resistive Nets as Charge Multiplexing Circuits;
- Signal preamplifiers;
- 16 bit ADCs;
- Timing Filter Amplifiers (TFAs) for fast signal shaping;
- Constant Fraction Discriminators (CFDs) for trigger generation;
- Coincidence unit;
- NIM to TTL converter.

### 5.2. Charge Multiplexing Circuits

The idea behind a Charge Multiplexing Circuit is to “encode” each anode in such a way that it can be univocally identified from all the other anodes. The simplest approach is to connect all the anodes with a single wire, with uniform resistivity, in a so called Position-Sensitive Proportional Counter Readout [BK70]. Our implementation follows the Discretized Position Circuit of [Sie+96], in which the anodes are connected by a net of discrete resistors with different values (figure 5.2 on page 47). The total energy of an event is easily computed by:

$$E = V_A + V_B + V_C + V_D, \quad (5.1)$$

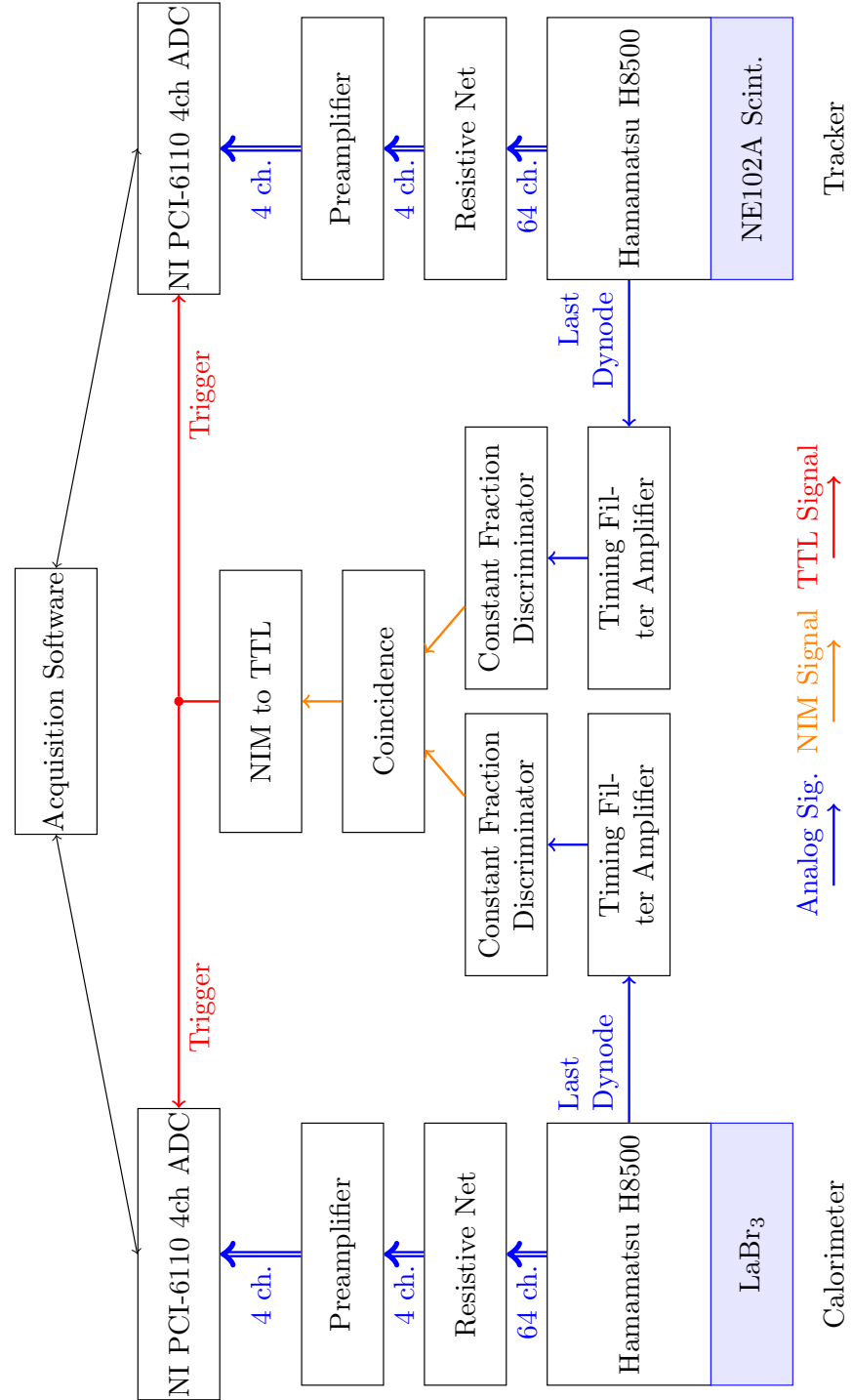


Figure 5.1.: Block diagram of the readout electronics.

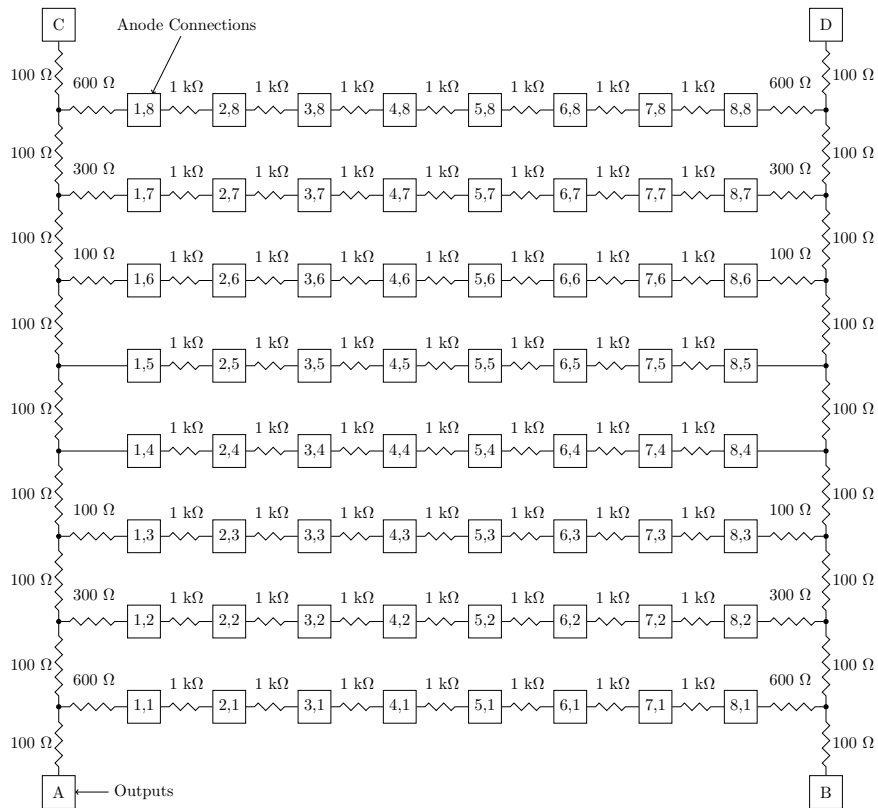


Figure 5.2.: Resistor Net of a Discretized Position Circuit.

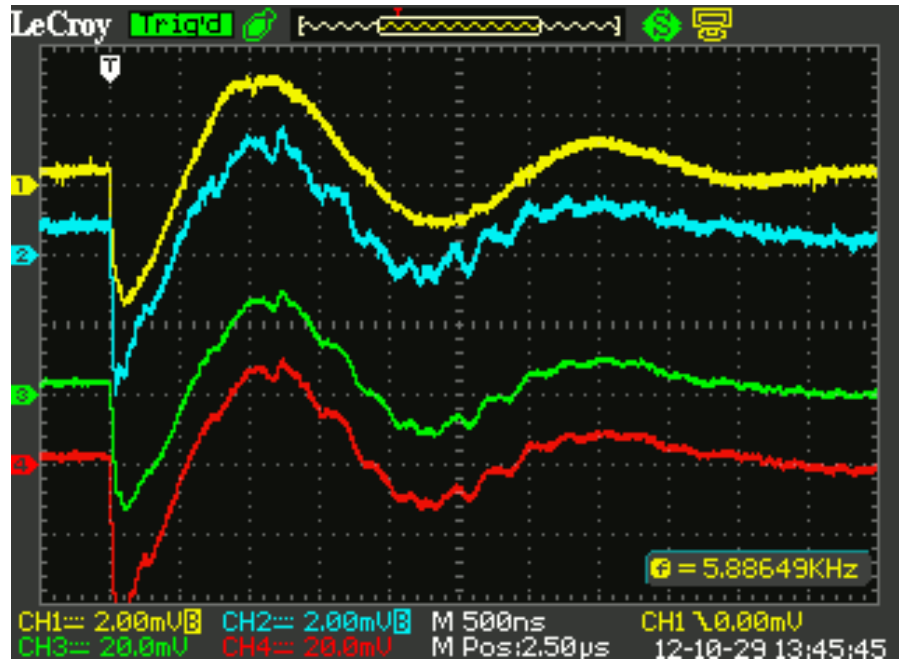


Figure 5.3.: Signals of the four outputs of the Resistor Net, source  $^{57}\text{Co}$ , scintillator  $\text{LaBr}_3$ , high voltage 1000 V.

while position values are:

$$x = \frac{(V_A + V_C) - (V_B + V_D)}{V_A + V_B + V_C + V_D} \quad (5.2)$$

and

$$y = \frac{(V_A + V_B) - (V_C + V_D)}{V_A + V_B + V_C + V_D}. \quad (5.3)$$

In figure 5.3 we can see an example of the signals from the output of the resistive net. They show a very fast leading edge, with a raising time of the order of the scintillating crystal, and long oscillating tails, that protract for about  $5\ \mu\text{s}$ . The long tails limit the possible acquisition rate up to about 200 kHz, if we want to avoid a significative pile-up of the signals.

### 5.3. Signal Preamplifiers

Each of the four signals, coming out of the resistive net, is integrated and amplified by a custom-made circuit, figure 5.4 on the next page. The circuit is composed of three stages:

1. a current integrator;
2. a signal amplifier;

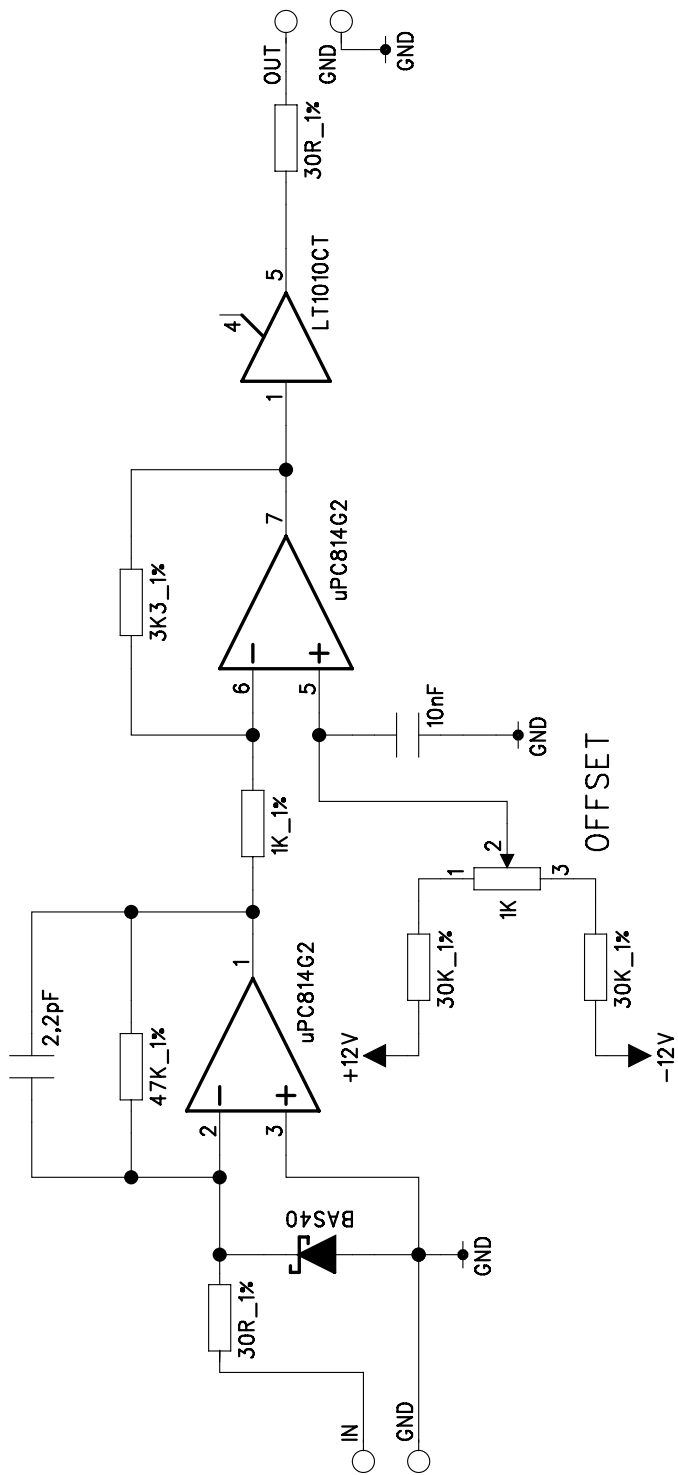
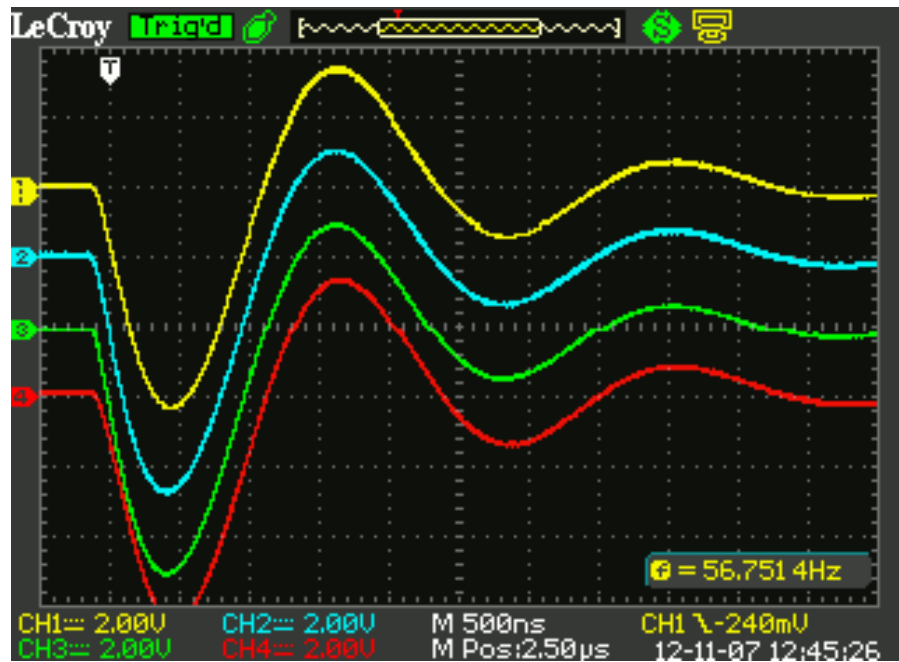
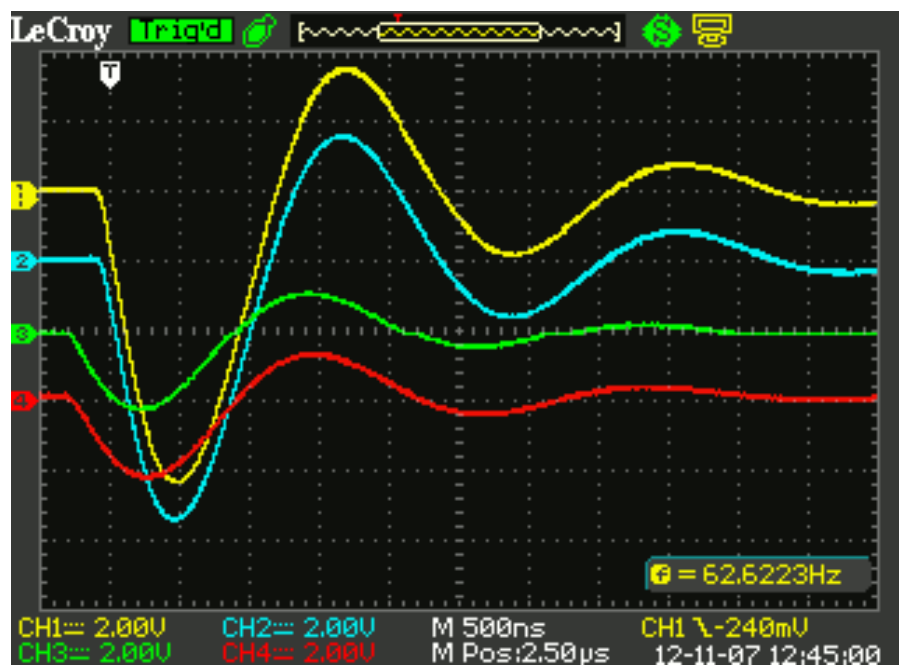


Figure 5.4.: Signal preamplifier circuit schematic.



(a) Signals generated in the center of the scintillator.



(b) Signals generated in the periphery of the scintillator.

Figure 5.5.: Signals of the four outputs of the preamplifier, source  $^{57}\text{Co}$ , scintillator  $\text{LaBr}_3$ , high voltage 1000 V.



3. a current buffer.

At the entrance of the circuit there is a  $30\ \Omega$  resistor followed by a protection diode, used to avoid saturations of the following circuit.

The charge integrator is constituted by the op amp uPC814 with a resistor and a capacitor on the feedback loop, the resistor is a through-hole exchangeable element, to easily modify the integration time, while the capacitor is surface-mounted. The integrator is in an inverting set-up, in which

$$V_{\text{out}} = -\frac{1}{RC} \int dt V_{\text{in}}(t) \quad (5.4)$$

where  $R$  and  $C$  are respectively the feedback resistor value and capacitor value [HH89]. The integration time is given by

$$\tau = RC = 2.2\ \text{pF} \cdot 47\ \text{k}\Omega = 0.10\ \mu\text{s}, \quad (5.5)$$

that means that the circuit integrates signals for a length of time of the order of  $\tau$  and then loses the charge. This time limited integration gives a smoothed signal with its peak value proportional to the total charge of the input signal but inverted.

Following the integrator there is a signal amplifier constituted by another uPC814, the amplification factor is given by the ratio between the feedback resistor and the input resistor:

$$V_{\text{out}} = -\frac{R_f}{R_i} V_{\text{in}} = \begin{cases} -\frac{2.4\ \text{k}\Omega}{1.1\ \text{k}\Omega} V_{\text{in}} = 2.2 V_{\text{in}} & \text{Calorimeter} \\ -\frac{27\ \text{k}\Omega}{1.1\ \text{k}\Omega} V_{\text{in}} = 25 V_{\text{in}} & \text{Tracker} \end{cases} \quad (5.6)$$

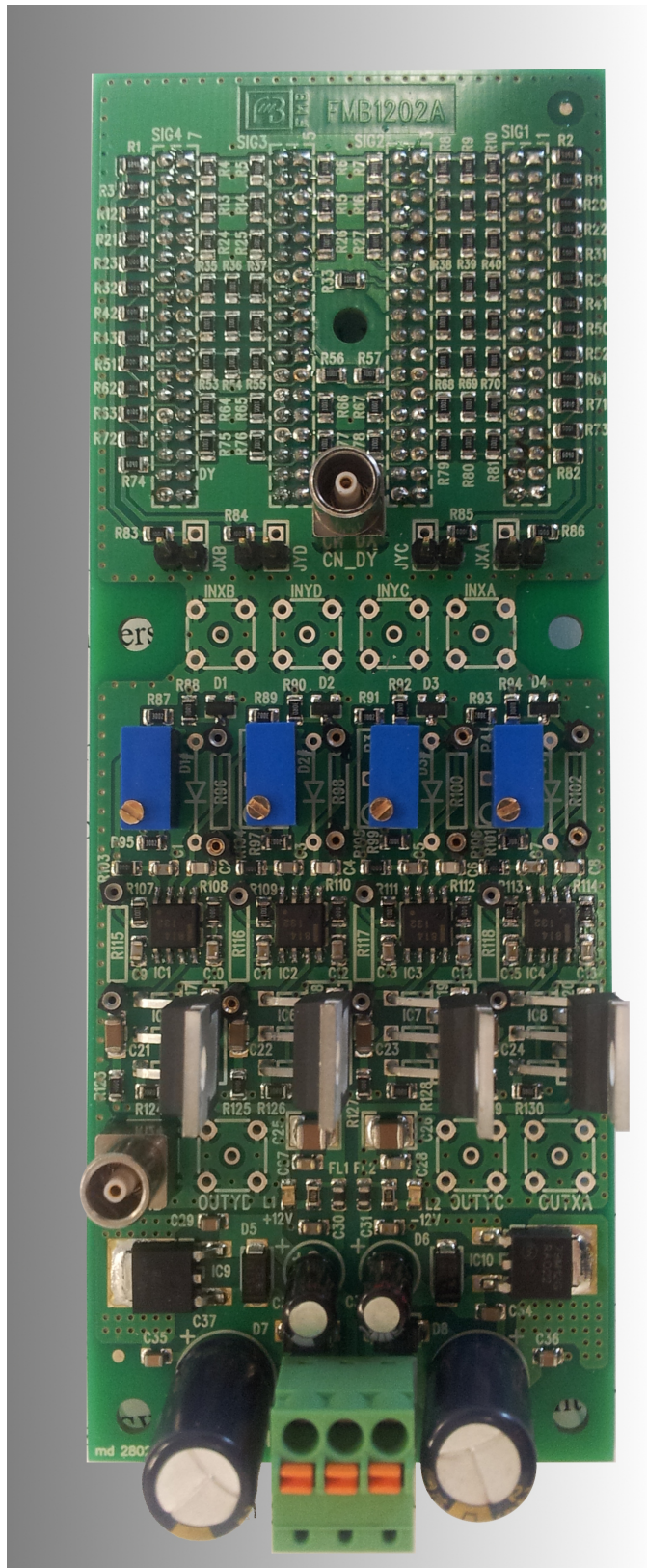
This device thus inverts the integrated signal and amplifies it.

Lastly, after the signal amplifier, there is a power buffer LT1010 [Lt1] that is used to drive the  $50\ \Omega$  coaxial cables. The op amp uPC814 is unable to provide enough current to give a significant voltage signal at the end of the cable.

In figure 5.5 on the facing page we can see an example of the signals generated by the preamplifier; there are two examples, one in which the generating event was near the center and thus the signals are of the same height and the other in which the signals are much different because they were generated on a side of the scintillator. We see that the rising time is significantly elongated by the integrator of the preamplifier and the long tails are still present. The tails are of about the same length of fig. 5.3 on page 48, thus the maximum rate of the circuit is determined by the resistor network and not by the shaping time.

## 5.4. Charge Multiplexing and Preamplifier PCB

Collaborating with an external company, we developed a Printed Circuit Board (PCB) to embed the Charge Multiplexing Resistor Net and the Signal Preamplifier in a single device (Figure 5.6 on the following page). Board



52

Figure 5.6.: Charge Multiplexing and Preamplifier PCB; Resistive Net on the top of the image, preamplifier on the bottom.

schematics and layout are on Appendix A on page 111. The board was designed with modularity in mind, the Resistive Net is independent from the Preamplifier circuit and the two parts can be isolated by disconnecting four jumpers. This allows us to use the very same preamplifier with different Resistive Nets in the future and *vice versa*.

## 5.5. Trigger generation

The fast signal from the last dynode of each H8500 is used for trigger generation with these steps:

1. they are fed to Timig Filter Amplifiers (TFAs) to shape and amplify them in order to provide better signals to the Constan Fraction Discriminators (CFDs);
2. they are discriminated with CFDs;
3. the two generated NIM signals are fed to a NIM coincidence unit;
4. the NIM signal is fed to a NIM to TTL converter to generate a signal suitable to the ADC trigger.

## 5.6. NIM-TTL Converter

We developed the NIM to TTL converter to be able to select a dead time, in order to let the ADC finish the conversion of the analog signals before a new input.

At the entrance (Fig. 5.7 on the following page) there is an inverting amplifier that multiplies the NIM signal of  $-800\text{ mV}$  to get a positive signal of about  $4.8\text{ V}$ . A little bit of integration time ( $42\text{ ns}$ ) is added to filter high frequency noises. The output of the inverting amplifier is fed to a monostable multivibrator 74HCT4538 [74h] that generates a TTL signal when it sees a rising edge in the input pin with a delay of about  $100\text{ ns}$  (Fig. 5.7 on the next page). The signal length ( $600\text{ ns}$ ) is set by regulating the R5 trimmer. The TTL output is used as the trigger signal for the ADC (on its falling edge) and as a start signal for a second multivibrator that generates the dead time ( $5\text{ }\mu\text{s}$ ). The output of the second monostable is used as a veto for the first monostable and for the second monostable itself, during the signal duration both the monostables do not accept new incoming signals. In figure 5.9 on page 56 there are examples of the triggering signals, in figure 5.10 on page 57 there is a closeup of the signals edges, and in figure 5.11 on page 58 there are examples of the triggering signals with the analog signals.

## 5.7. Circuit simulation

The resistor net and preamplifier were simulated with the open-source software Qucs [Quc], in figure 5.12 on page 59 there is the whole simulation

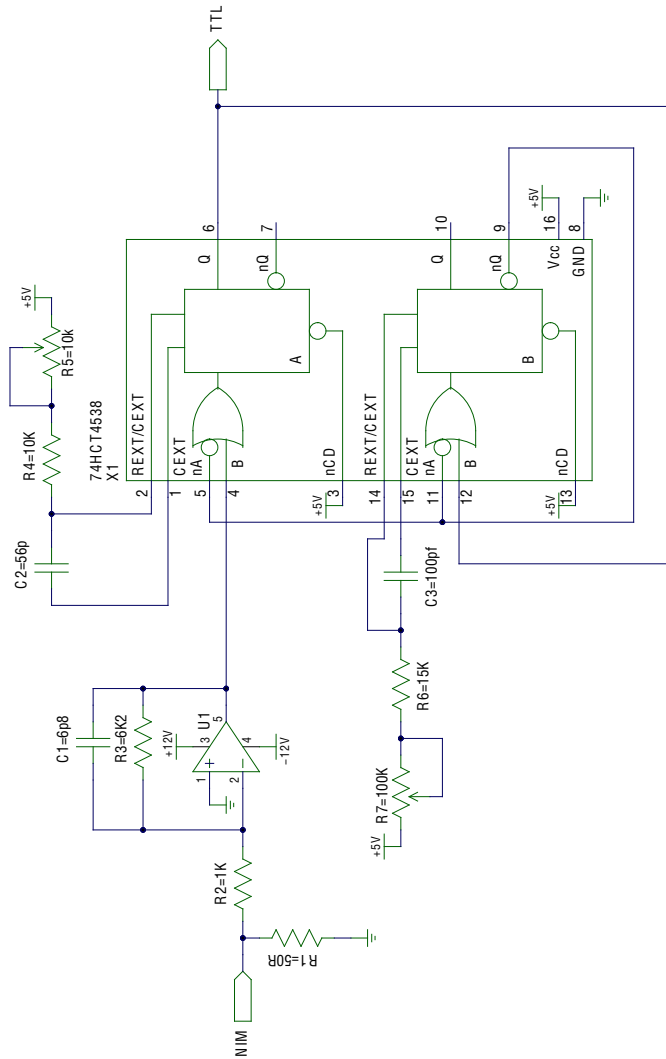


Figure 5.7.: NIM to TTL converter with delay generation and dead-time generation.

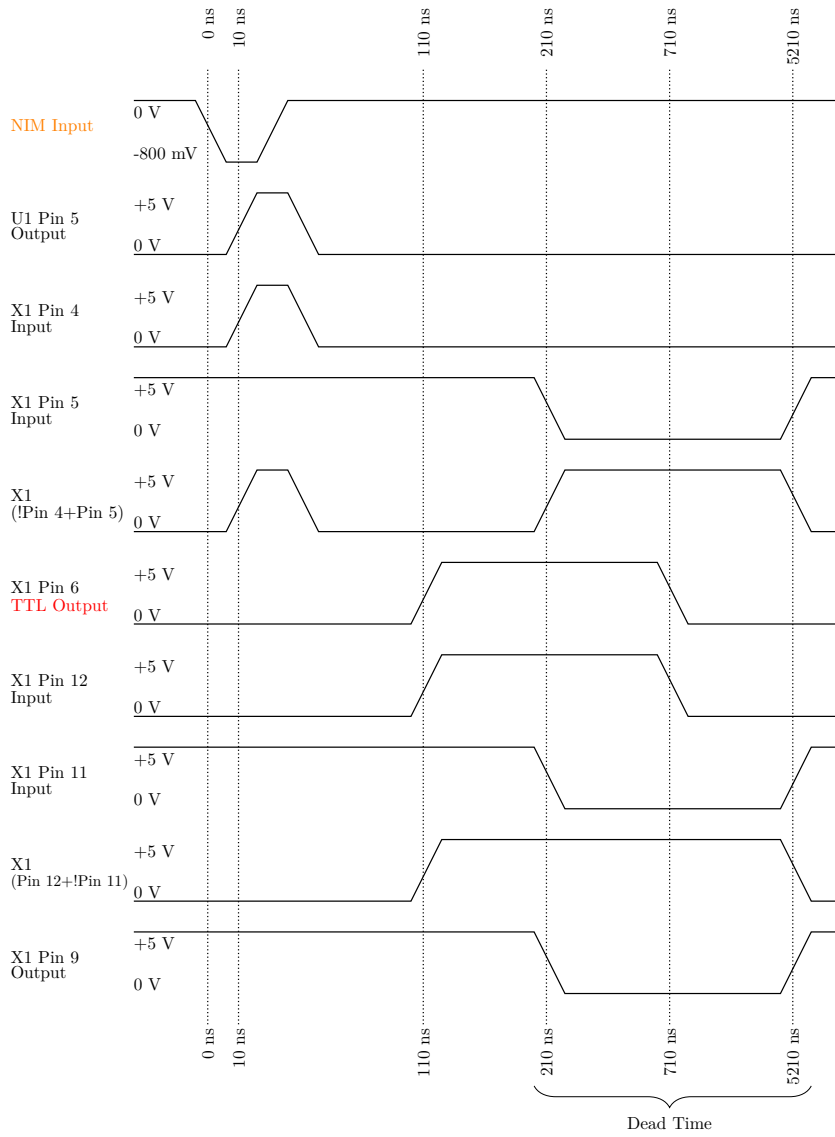
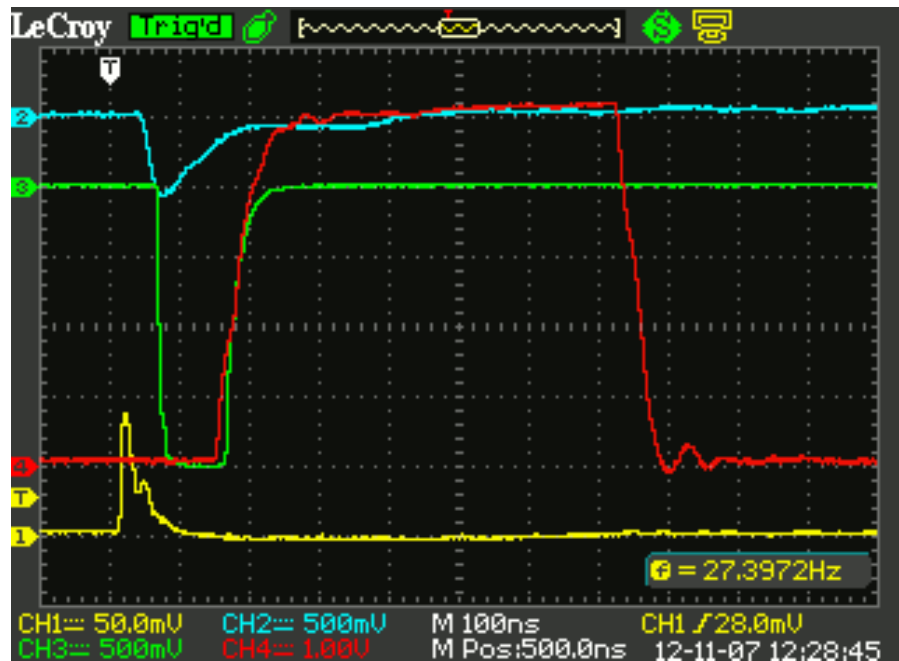
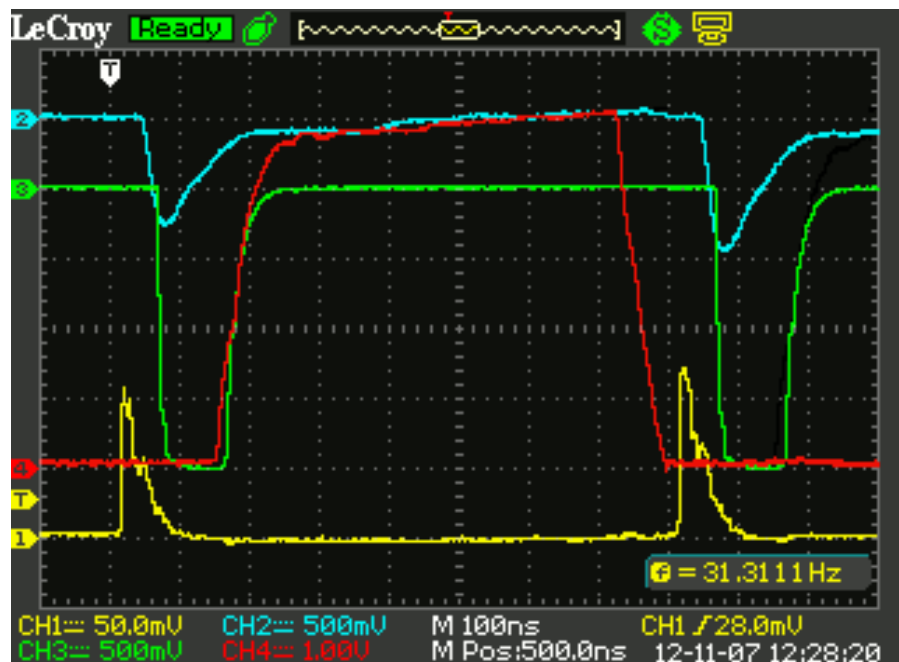


Figure 5.8.: Signals of the NIM to TTL converter.



(a) Example of signals.



(b) Example of vetoed signals.

Figure 5.9.: Signals of the triggering electronics: (1) Fast H8500 triggering signal, (2) Timing Filter Amplifier output, (3) NIM triggering signal, (4) TTL triggering signal.

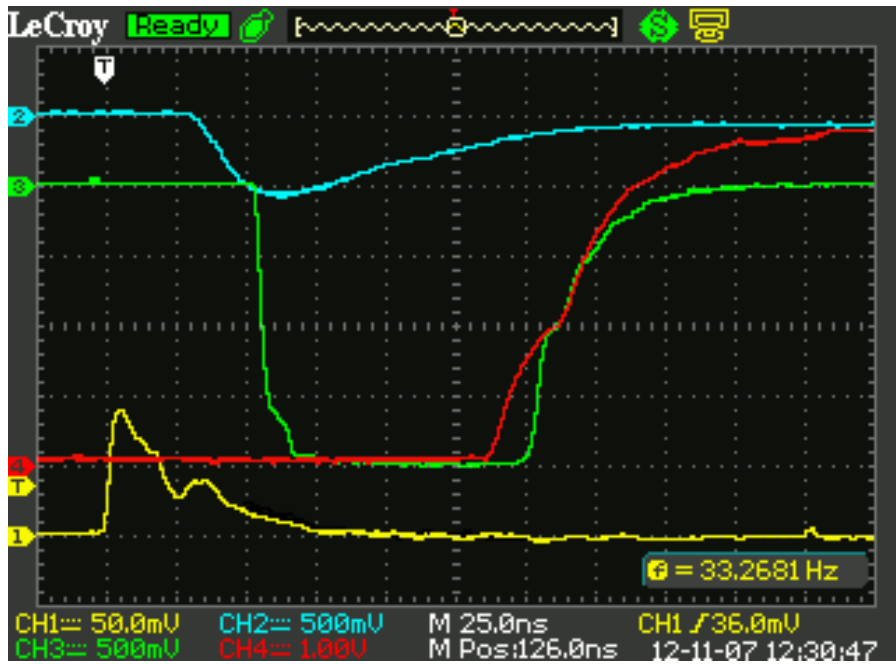
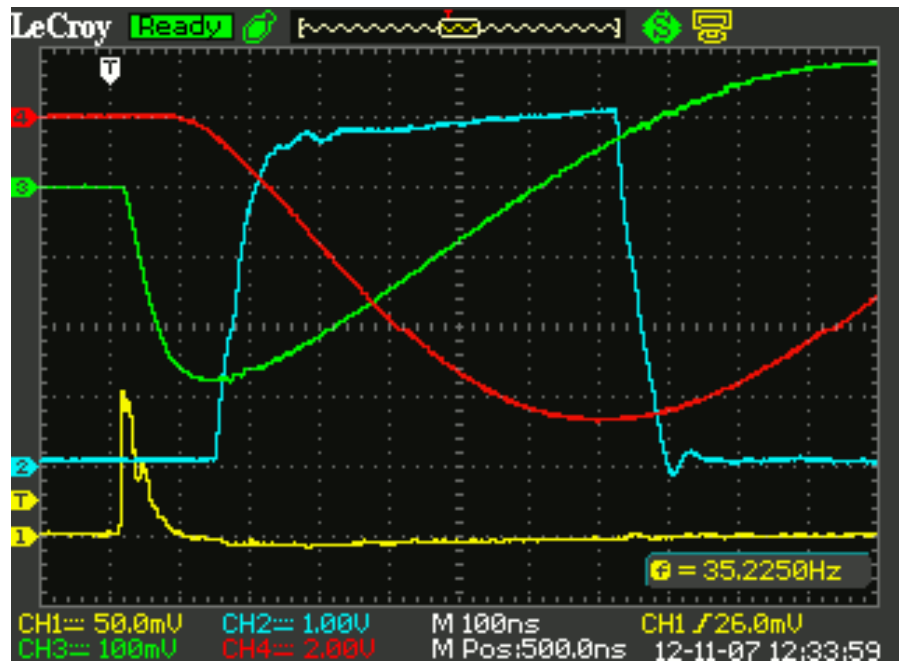
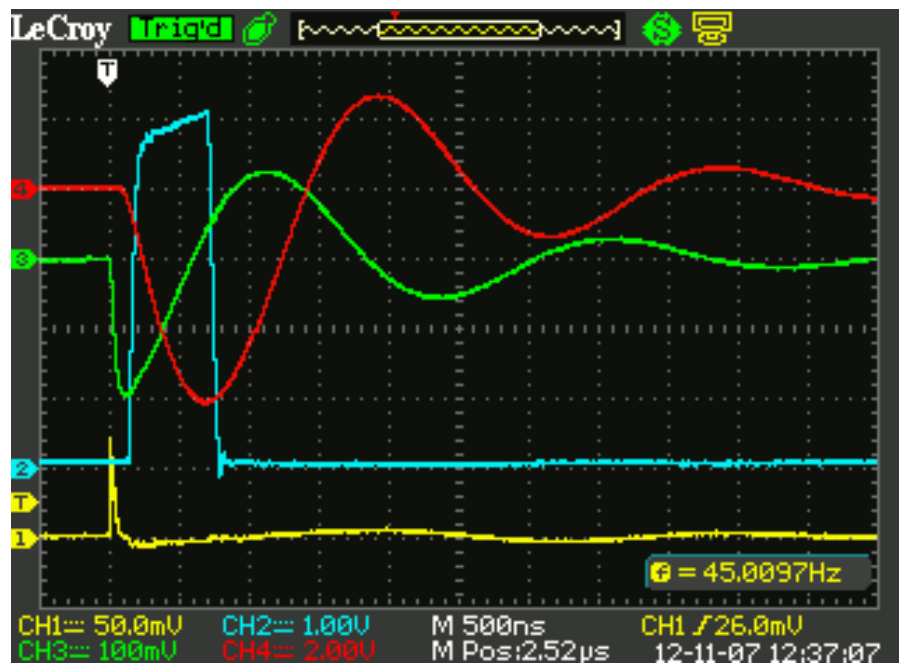


Figure 5.10.: Edges of signals of the triggering electronics: (1) Fast H8500 triggering signal, (2) Timing Filter Amplifier output, (3) NIM triggering signal, (4) TTL triggering signal.



(a) Edges of the triggering signals.



(b) Edges of the triggering signals with full analog signals.

Figure 5.11.: Signals of the triggering electronics: (1) Fast H8500 triggering signal, (2) TTL triggering signal, (3) Resistor Network signal, (4) Pre-amplifier signal.



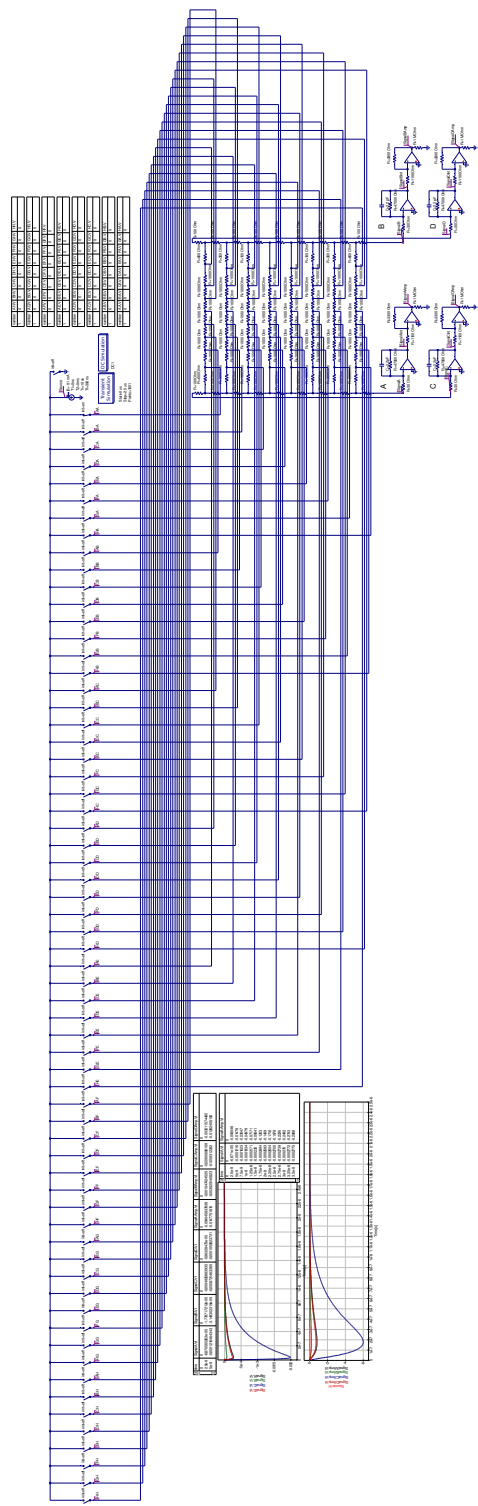


Figure 5.12.: Qucs [Quc] simulation schematic of resistor net and preamplifier.

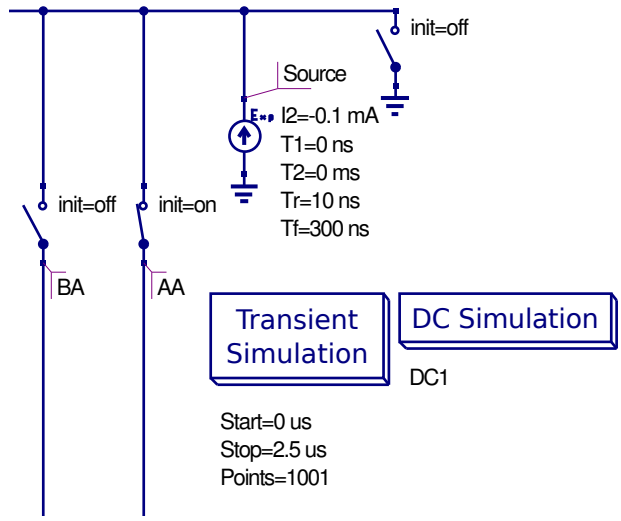


Figure 5.13.: Zoom of signal generator schematic and simulation parameters; exponential pulse shape, 10 ns rising time, 300 ns falling time,  $-100 \mu\text{A}$  maximum.

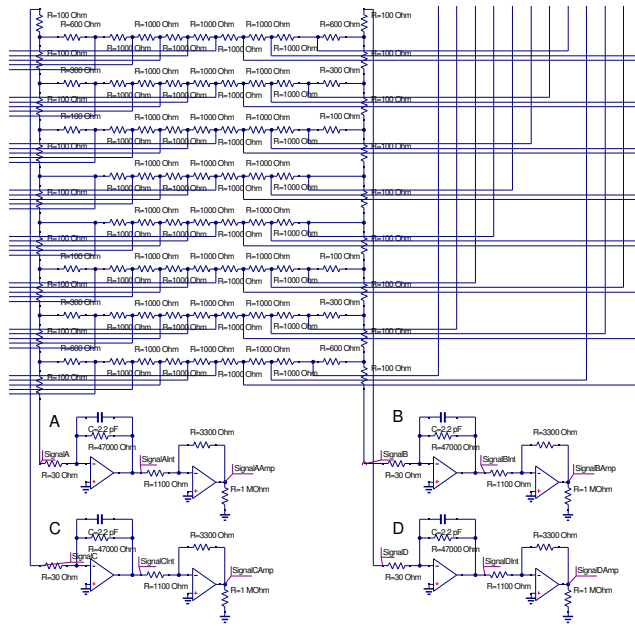
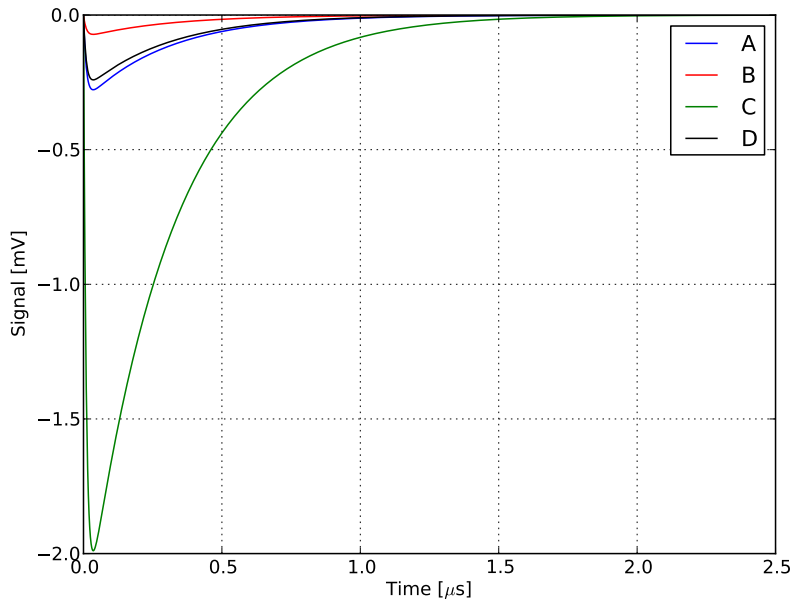
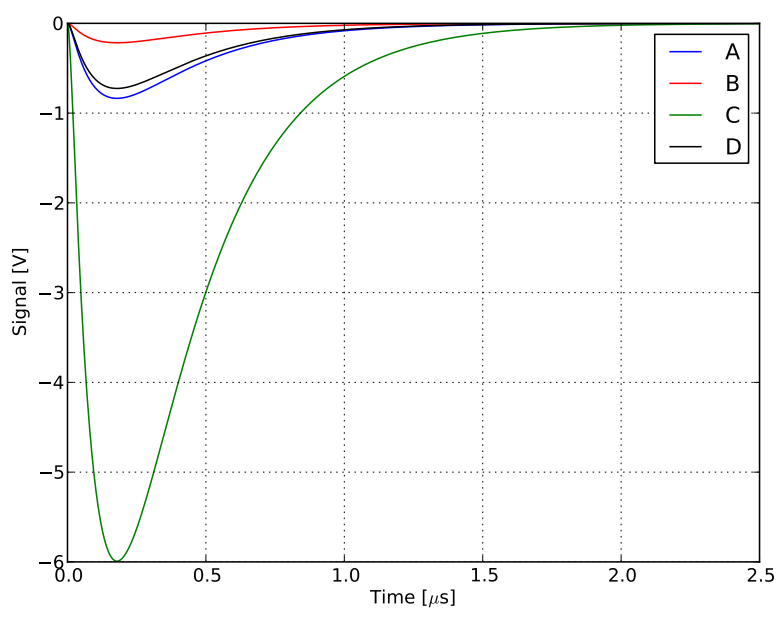


Figure 5.14.: Zoom of resistor net and preamplifier schematic.



(a) Resistor net outputs



(b) Preamplifier outputs

Figure 5.15.: Simulated analog signals of resistor net and preamplifier.

schematic. To simulate the incoming signal a transient simulation was performed with a current generator with an exponential pulse shape (Figure 5.13, 10 ns rising time, 300 ns falling time,  $-100 \mu\text{A}$  maximum). Signals were injected into the resistor net at the anodes connections, selecting the anodes with switches (switches examples in figure 5.13 on page 60, zoom on the resistor net in figure 5.14 on page 60). Qucs fails to simulate the oscillation following the PMT pulse but gives reasonable signals (Figure 5.15 on page 61) that were used to extract the anodes coordinates with equations (5.2) and (5.3) (figure 5.16 on page 64). Signal strength was also calculated in function of the position for each output channel to check the consistency of the result; figure 5.17 on page 65 shows an increase of the strength with the increase of the distance from the corner.

## 5.8. Current pulse generator

For calibration and testing purposes we developed a current pulse generator (Figure 5.18 on page 65) that simulates real photomultiplier signals. Pulses are generated by deriving TTL signals of a digital clock with a tunable frequency, such signals have a low quality rising edge that has to be cleaned with a fast comparator (MAX961) [Max]. Susequently they are filtered with a passive differentiator and with a diode to cut the negative pulse. The filter output is split and fed to an op amp (LM7171) [Lm7] in an inverting configuration to generate a Fast NIM signal, that is used for the NIM-TTL translator. The resulting pulse has a rising time of about 20 ns and a falling time of about 200 ns; in figure 5.19 on page 66 there are the signals extracted at the specified test points (Figure 5.18 on page 65). The second branch of the filter output is fed to an op amp in an non-inverting configuration, that is used to amplify the signal before passing it to a *Howland current pump* [How]. The Howland current pump has the propriety of offering an infinite output impedance if the four resistors are exactly matched. In our case the output current is

$$I_{\text{out}} = \frac{V_{\text{in}}}{10 \text{ k}\Omega} = \frac{8 \text{ V}}{10 \text{ k}\Omega} = 800 \mu\text{A} \quad (5.7)$$

where  $V_{\text{in}}$  is the input voltage of the Howland pump. The resulting pulse has a rising time of about 20 ns and a falling time of about 200 ns.

As in the simulation current pulsed were injected into the resistor net, at the anodes connections, and the dots positions were acquired with the whole system (Figure 5.20 on page 67). The dots positions are so narrow that they can hardly be seen on the plot with the naked eye, we can rely on the image projections on the sides, though. Signal strength was also plot in function of the position for each output channel; figure 5.21 on page 68 shows an increase of the strength with the increase of the distance from the corner, as in the simulation.

## 5.9. LED pulse generator

We developed also a LED pulse generator (Figure 5.22 on page 68) that simulates real scintillating light signals. Pulses are generated by deriving TTL signals of a digital clock with a tunable frequency, such signals have a low quality rising edge that has to be cleaned with a fast comparator (MAX961) [Max]. Susequently they are decoupled with an op amp voltage follower (LM7171) [Lm7] and filtered with a passive differentiator and with a diode to cut the negative pulse. The filter output is fed to an op amp used to drive a BF155 NPN transistor, which provides the necessary current for the green Light Emitting Diode (LED). The resulting pulse has a rising time of about 15 ns and a falling time of about 25 ns; in figure 5.23 on page 69 there are the signals extracted at the specified test points (Figure 5.22 on page 68).

The LED plastic package was flattened, polished and inserted in a 1 mm collimator, in order to produce a small spot of light on the PMT sensitive surface.

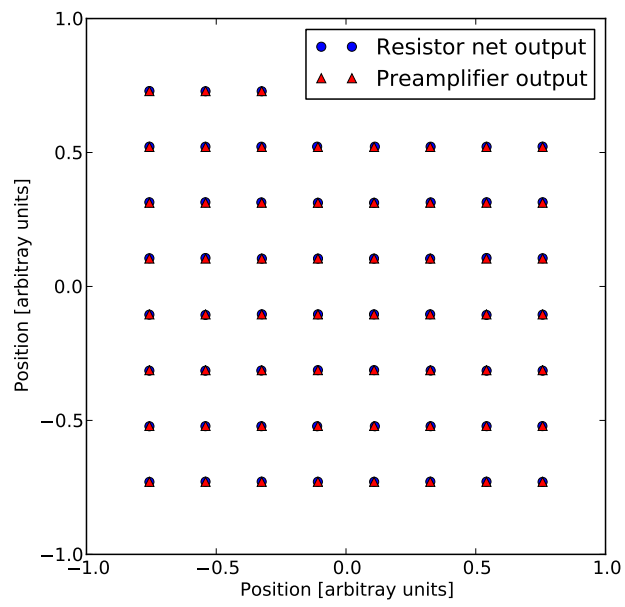


Figure 5.16.: Anodes coordinates reconstructed with equations (5.2) and (5.3) applied to simulated signal peak values.

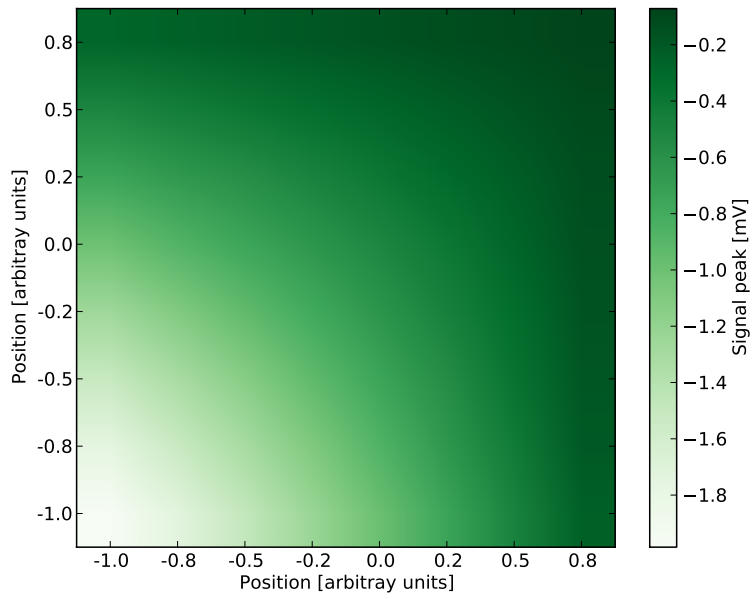


Figure 5.17.: Signal strength in function of the position for output channel A of simulated signals.

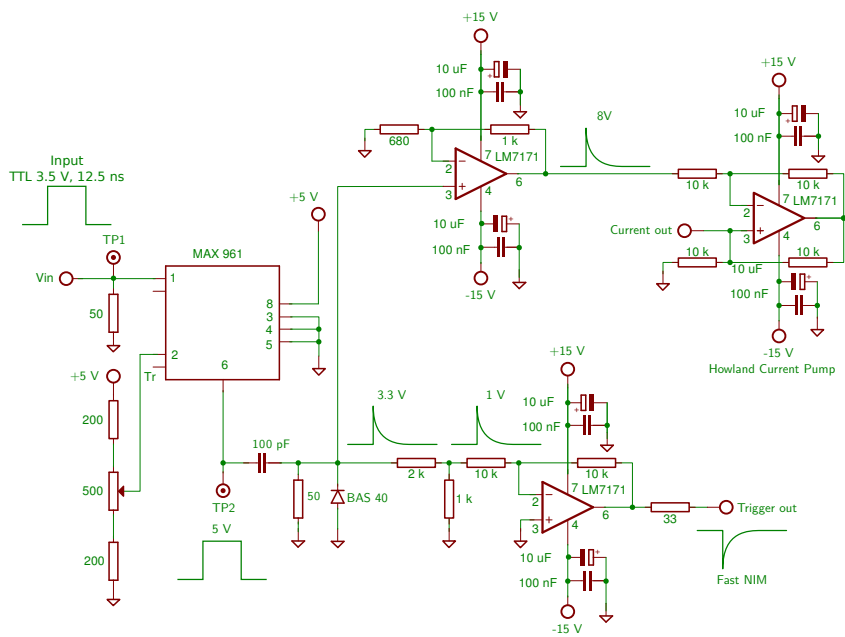


Figure 5.18.: Current Pulse generator

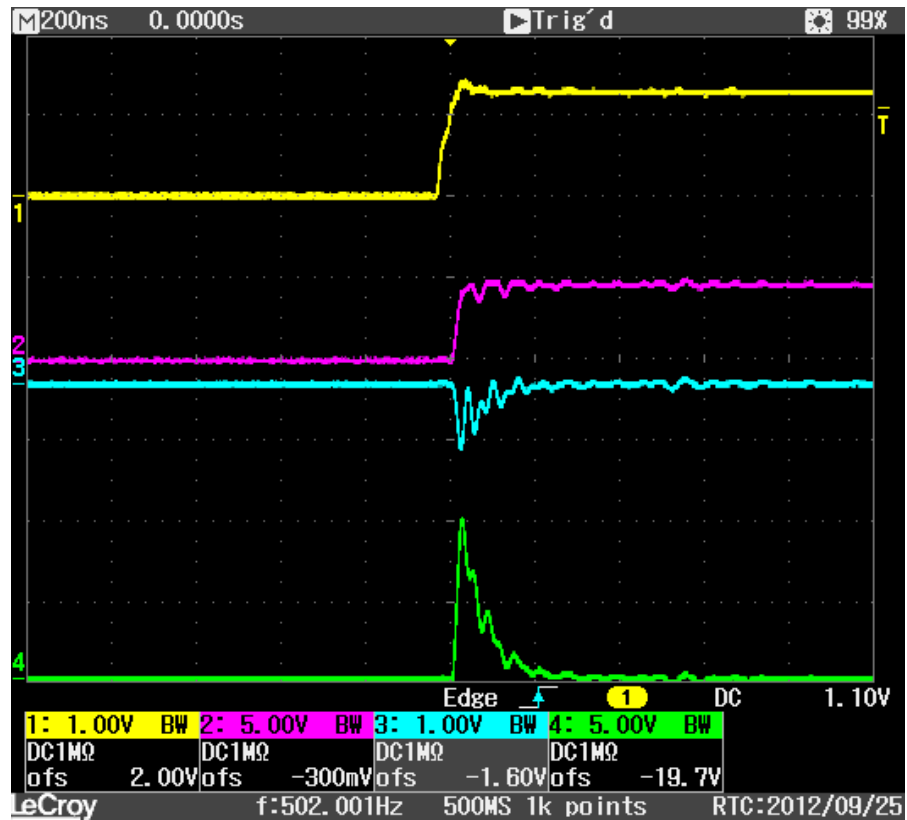


Figure 5.19.: Signals of the pulse generator (Figure 5.18 on the preceding page): (1) Input TTL signal from clock (variable frequency), test point 1; (2) Comparator output, test point 2; (3) Fast NIM trigger output; (4) Current pulse output.



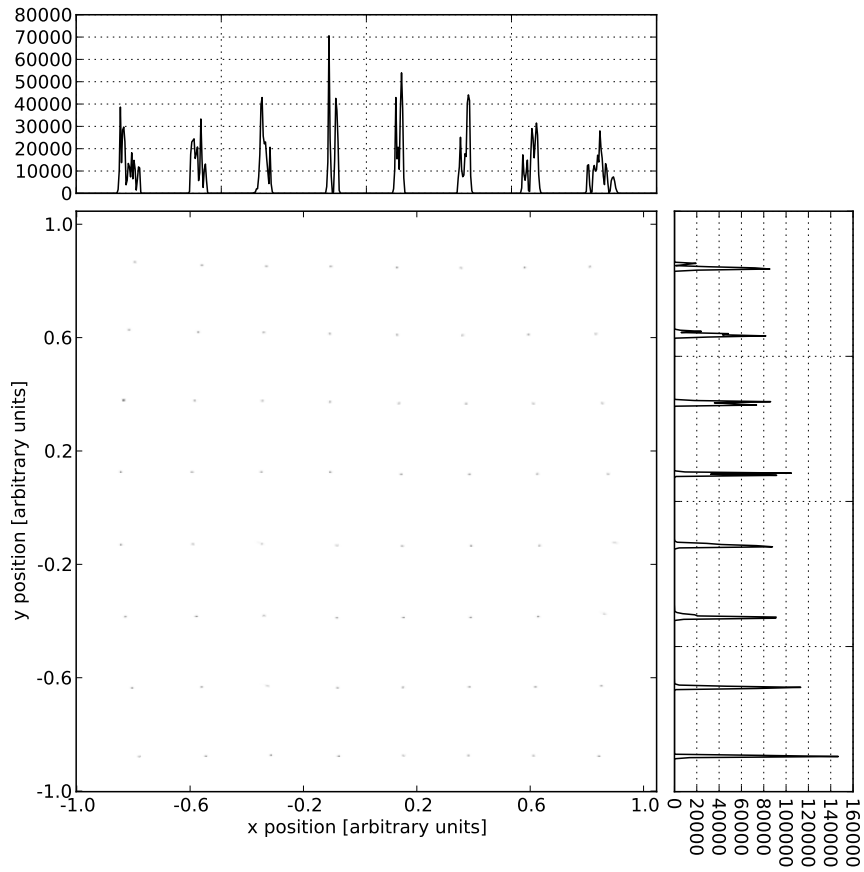


Figure 5.20.: Anodes coordinates reconstructed with equations (5.2) and (5.3) applied to real current signals of the developed current pulser.

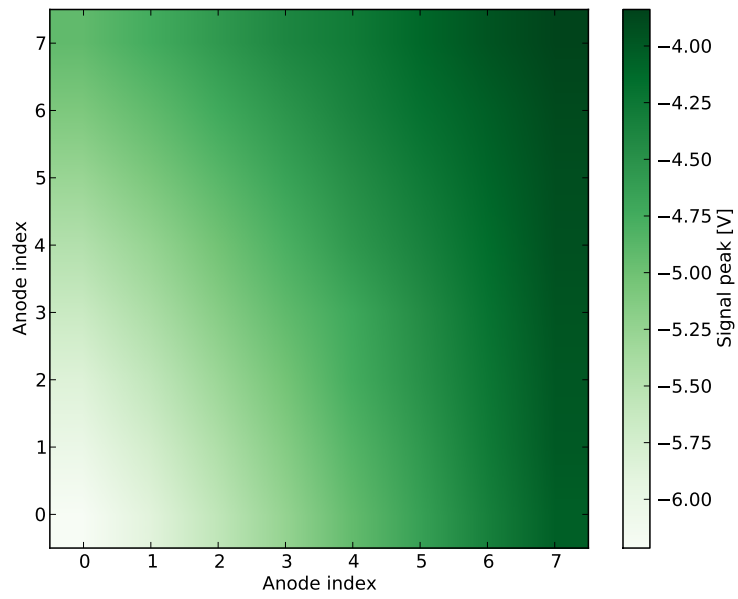


Figure 5.21.: Signal strength in function of the position for output channel A of real current signals of the developed current pulser.

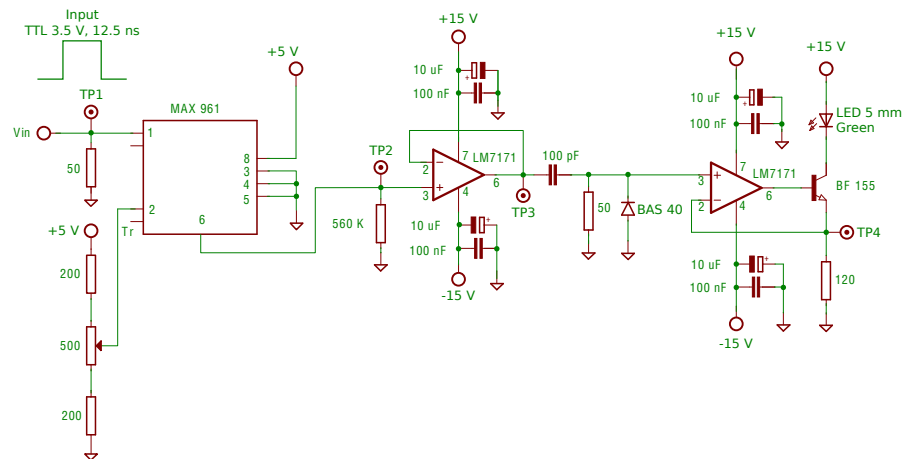


Figure 5.22.: LED Pulse generator

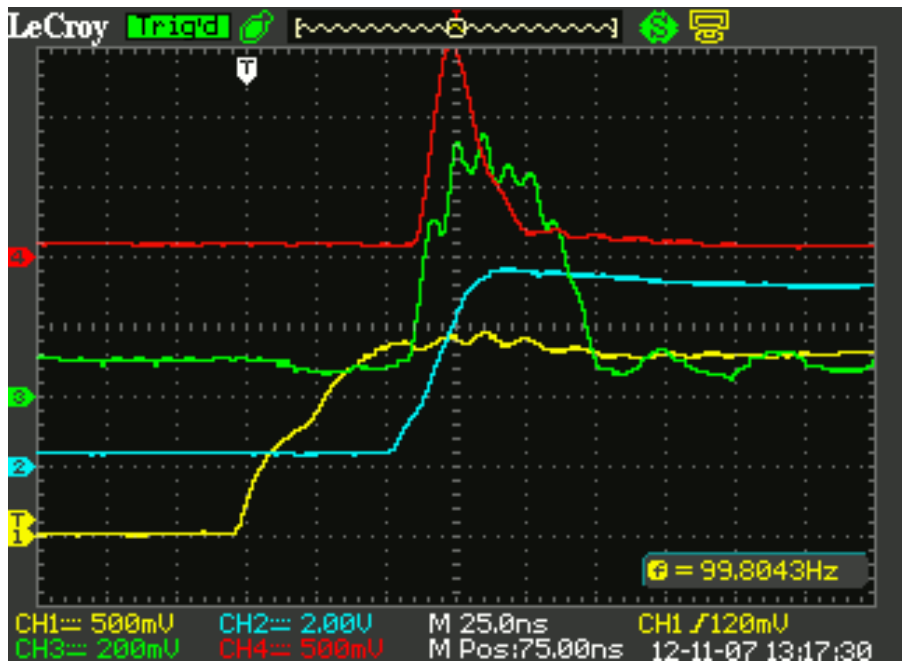


Figure 5.23.: Signals of the pulse generator (Figure 5.22 on the preceding page): (1) Input TTL signal from clock (variable frequency), test point 1; (2) Comparator output, test point 2; (3) Buffer output, test point 3; (4) Final pulse, test point 4.







## 6. Acquisition software

The acquisition software was written in LabVIEW [Lab] for its interface library with the ADC hardware. LabVIEW is a development environment that features an interface library for laboratory equipments and is able to simulate a lab environment. The programming is performed with the graphical language G, in which the user actually draws the connections between blocks that can perform certain functions. A LabVIEW program is divided into a front-panel, that is the Graphical User Interface, and a block diagram, that is the actual G program. In figure 6.1 on the next page we can see the front-panel of the acquisition software and in figure 6.2 on page 73 we can see the block diagram. The software is able to acquire the data but also to reconstruct the Tracker and Calorimeter images and spectra on-line, which is very useful for on-line system testing.

### 6.1. Hardware interface and Signals acquisition

The hardware interface is provided by the library DAQmx and it requires to be initialized with some blocks that define several parameters:

-  active ADCs, signal range, kind of measurement and analog inputs set-up;
-  trigger channel, active trigger edge, samples to be acquired per channel, maximum acquisition rate;
-  start the acquisition;
-  stops the acquisition and clears the communication channel with the hardware.

On the main acquisition cycle the block:

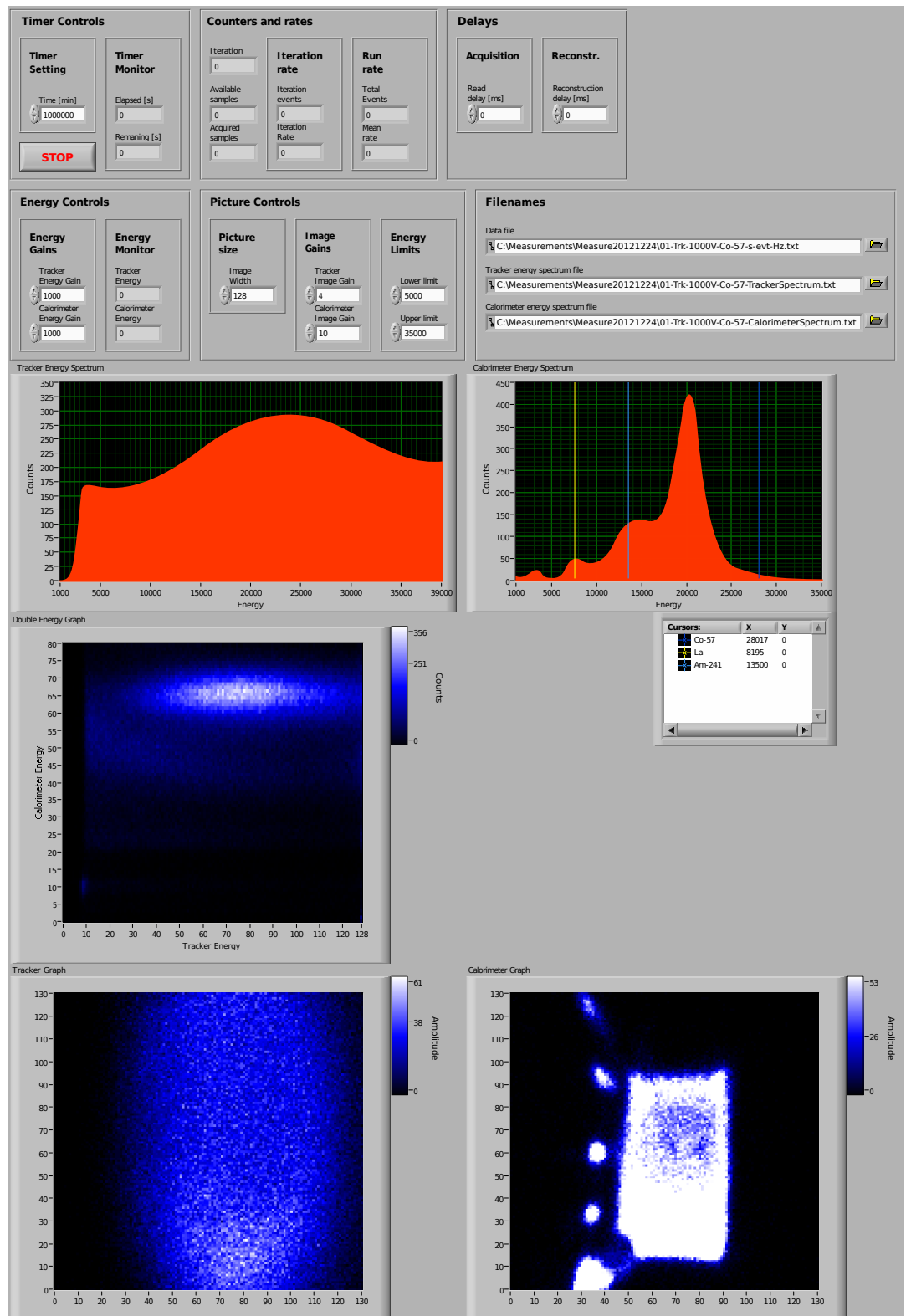


Figure 6.1.: Acquisition software front-panel.

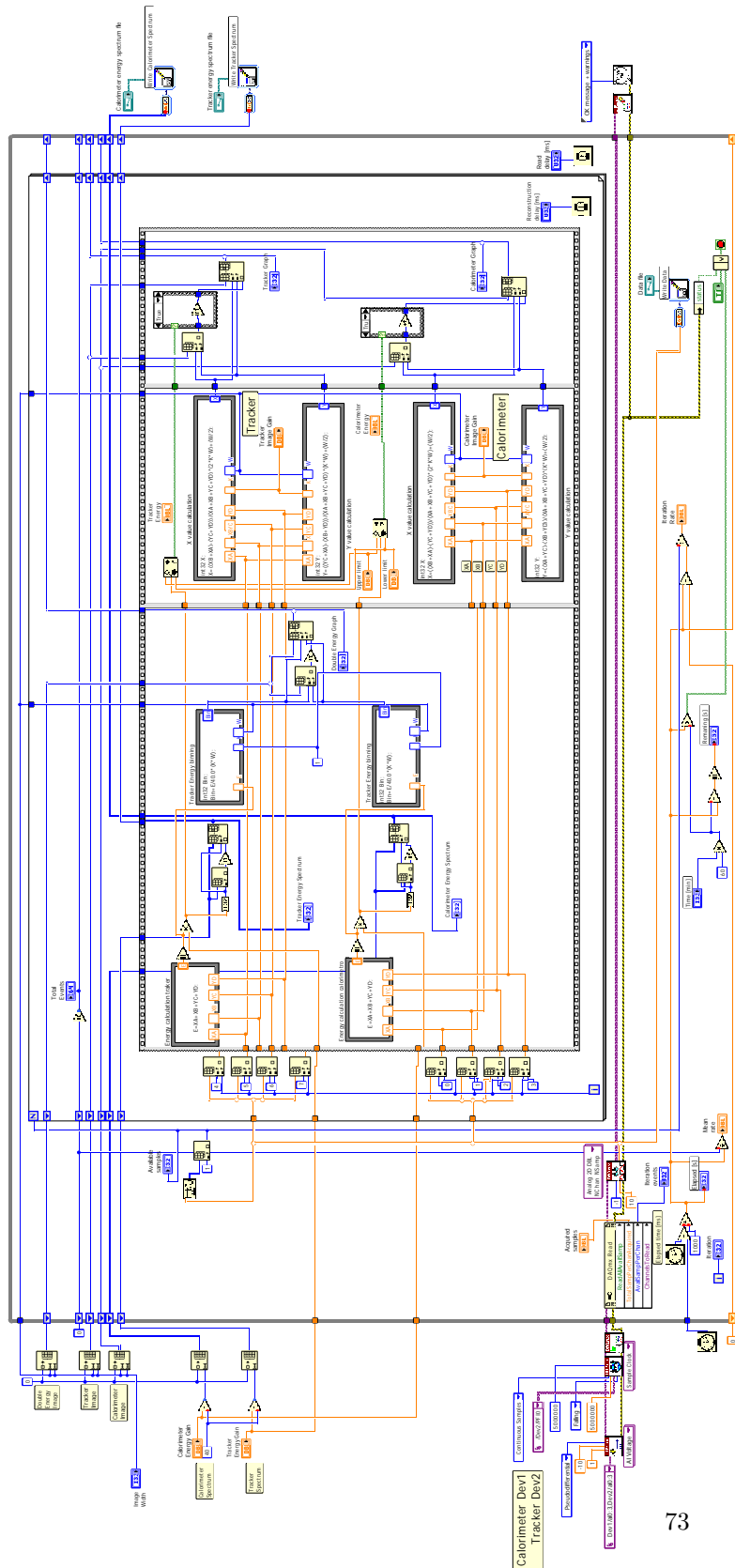


Figure 6.2.: Acquisition software block diagram.

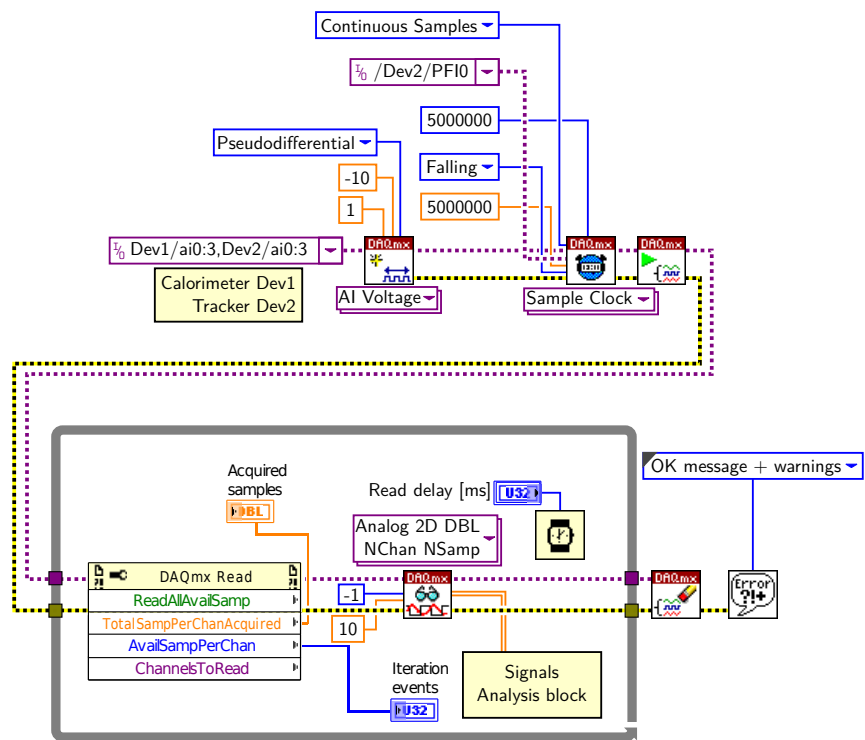


Figure 6.3.: Simplified block diagram showing only the hardware interface and iterations





is used to dump the hardware buffer in memory and set the timeout for this operation.

In figure 6.3 on the preceding page there is a simplified version of the block diagram that highlights just the hardware interface. On the top the hardware is initialized, then the control enters an infinite loop (main loop) in which the data are read from the hardware buffer. The main loop has a delay that is set in the front panel to pause the program between each reading of the data.

## 6.2. Signals analysis

Inside the main loop there is a second loop, a “for” loop that executes its instructions for each of the acquired events (the for loop is represented as a stack of sheets). Inside the loop the data enters as an array of eight values that are de-multiplexed in eight single signals that are analyzed. Inside the loop there is a control structure that guaranties the sequential execution the steps are:

1. Calculate the energies and fill the corresponding spectrum and bidimensional spectrum,
2. Calculate the coordinates,
3. Fill the image bidimensional histograms.

There is a second delay inside the reconstruction loop to avoid an overloading of the system.

## 6.3. Data storing

During the data acquisition the signals are stored, as raw numbers, in a file at each acquisition loop, in order to be able to abruptly stop the acquisition without losing data. The spectra are saved only at the end of the acquisition, because they can easily be recalculated from the raw data.



## 7. Detectors calibration and characterization

Energy Calibrations of the detectors were performed with two point-like calibration sources:

- $^{241}\text{Am}$ : 59 keV gamma-rays;
- $^{57}\text{Co}$ : 122 keV gamma-rays.

For spatial calibration, a custom-made and a commercial lead collimators were used:

- a parallel holes collimator, holes diameter 0.5 mm, thickness 2 cm;
- a single hole collimator, hole diameter 1 mm, thickness 1 mm.

### 7.1. Calorimeter calibration

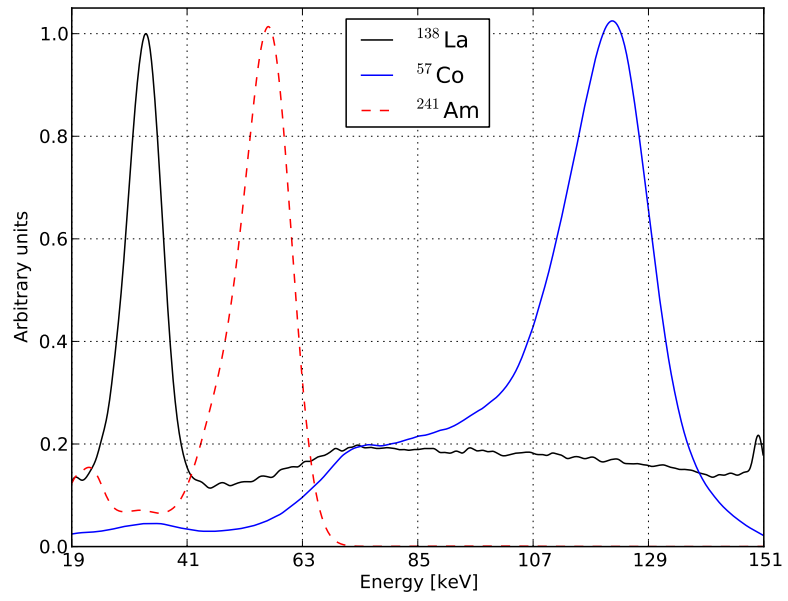
#### 7.1.1. Energy calibration

The calorimetric part of the whole detector was calibrated with the two point-like sources and using the intrinsic radioactivity of  $^{138}\text{La}$  of the  $\text{LaBr}_3$  scintillator. The energy resolution is about 18% at the 122 keV line.

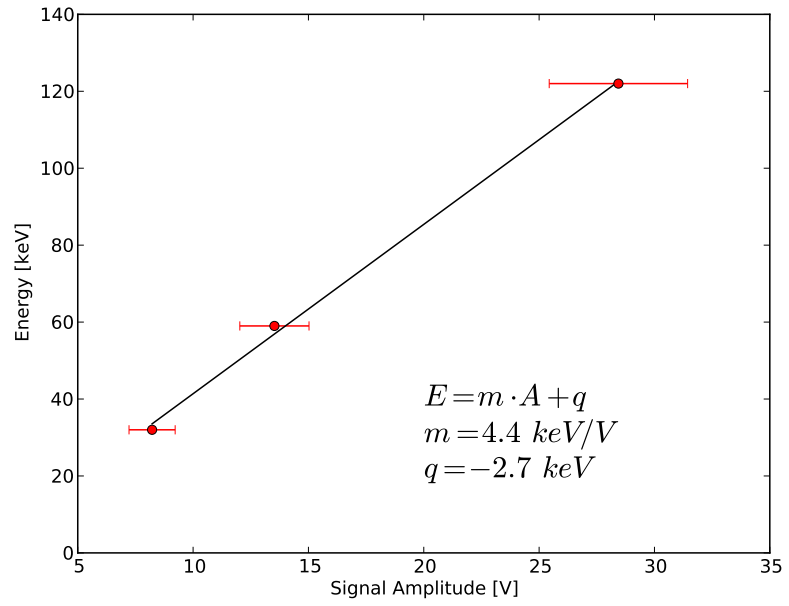
#### 7.1.2. Photomultiplier spatial linearization

Using the LED pulser (Section 5.9 on page 63) and an automatic positioning system, we shined the LED light directly on the Hamamatsu 8500, in a grid with spacing of 5 mm, to verify the spatial linearity and uniformity. Figure 7.2 on page 79 shows the results, in which we can see that the image is not uniform and there are artifacts. The resolution varies depending on the distance from the center and goes from 1 mm to 3 mm. The grid shows a lack of linearity that would lead to poor Compton images if not suitably elaborated.

To linearize the dots positions we developed an algorithm that interpolates the peaks positions with spline functions [Kiu10; JOP+01] and then linearizes the whole image. With this technique some new artifacts are added on the edges of the image, but on those region the dots resolution is worse and this may not be the most important source of uncertainty. To explain the image artifacts we developed also a Monte Carlo algorithm that simulates the seen effects, see section 8 on page 89.

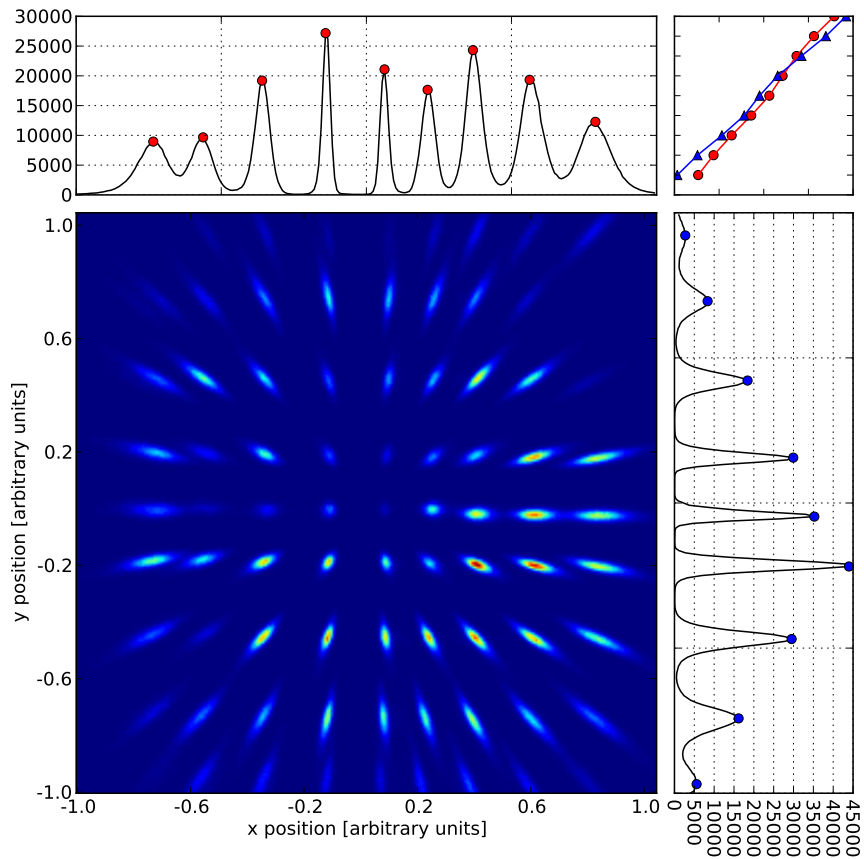


(a)

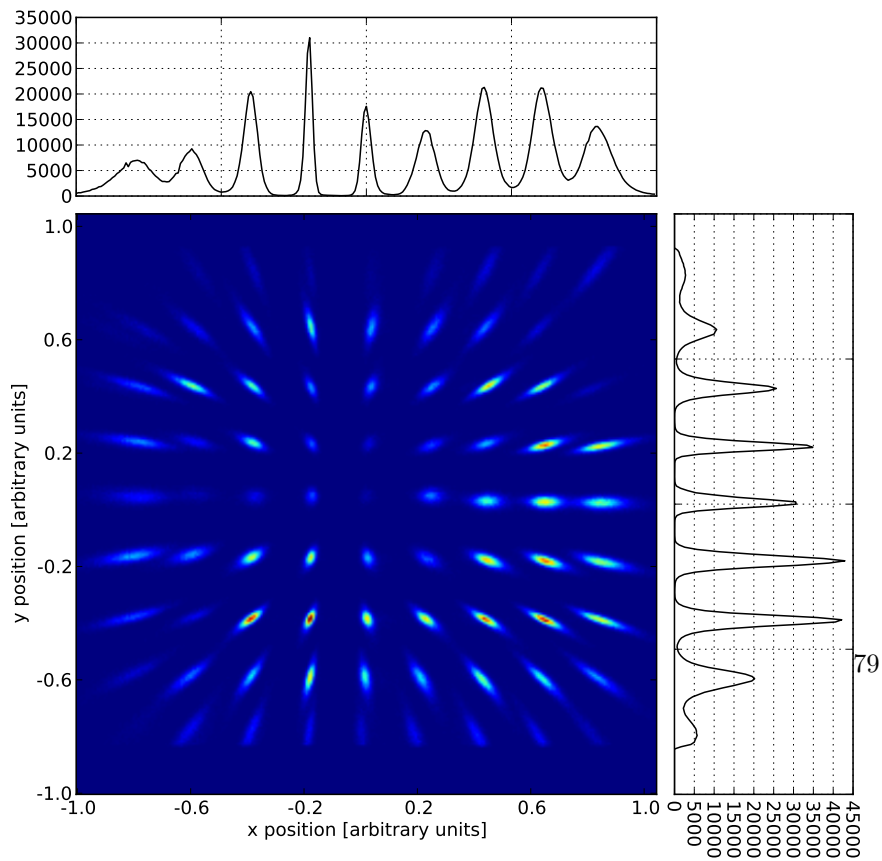


(b)

Figure 7.1.: Calorimeter calibration spectra and regression line.



(a) Raw version with spline interpolation



(b) Linearized version

Figure 7.2.: Dots generated in an uniform mesh with a LED and acquired with the Calorimeter.

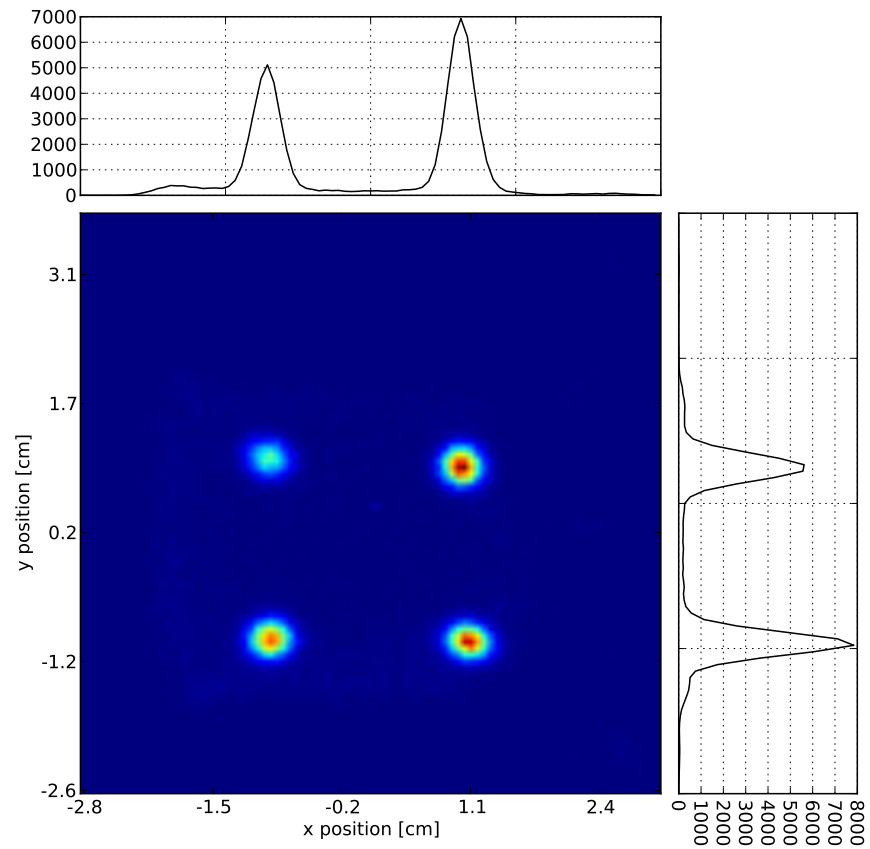


Figure 7.3.: Dots generated with a  $^{57}\text{Co}$  source and acquired with the Calorimeter.

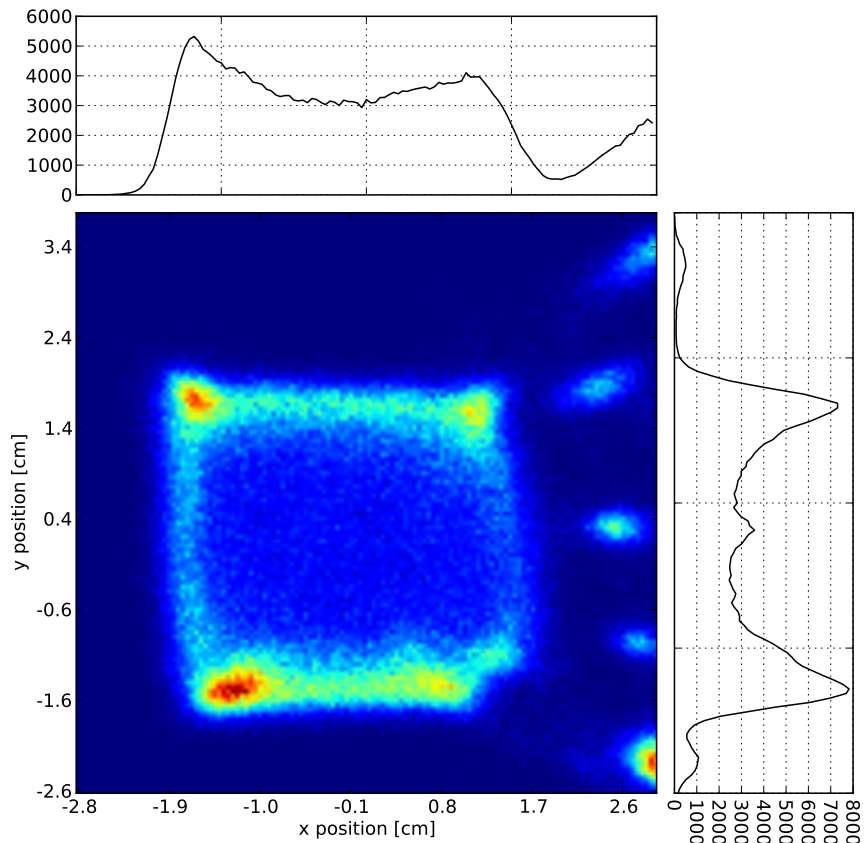


Figure 7.4.: Calorimeter uniformity.

### 7.1.3. Scintillator spatial calibration

A spatial calibration was performed with the system PMT+Scintillator using a collimated  $^{57}\text{Co}$  positioned in four spots with the automatic positioning system. The image, in figure 7.3 on the preceding page, shows a resolution of 2 mm which unfortunately is a little more than the double of the sub-millimeter resolution that can be obtained with a similar apparatus [Pan+11; Pan+09].

### 7.1.4. Uniformity

Figure 7.4 shows us the uniformity of the Calorimeter and tells us that the usable surface of the detector is about  $3\text{ cm} \times 3\text{ cm}$ , outside that area artifacts become important. Some artifacts and distortions may be due to the crystal breaks and defects (Figure 2.5 on page 17). This measurement was performed following the indications of the National Electrical Manufacturers Association (NEMA) Standard Publication NU 1-2001 [Nem].

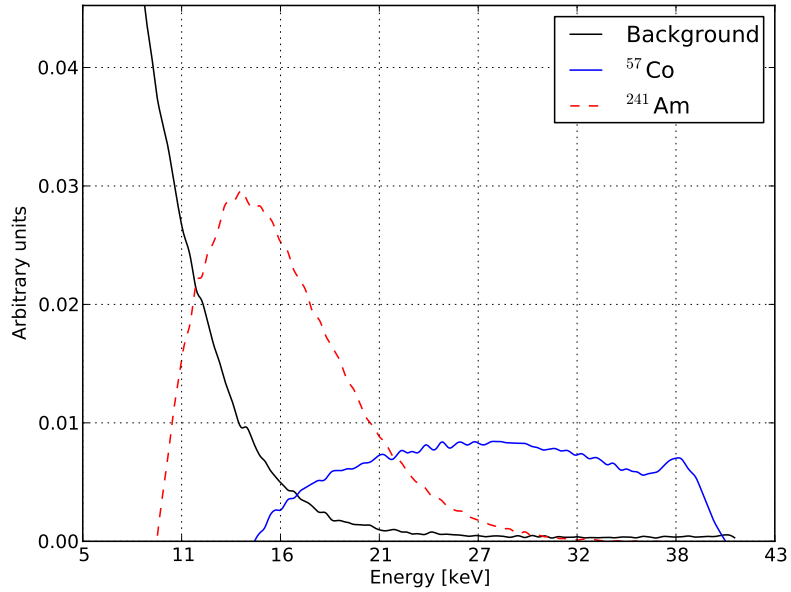


Figure 7.5.: Tracker calibration spectra.

## 7.2. Tracker calibration

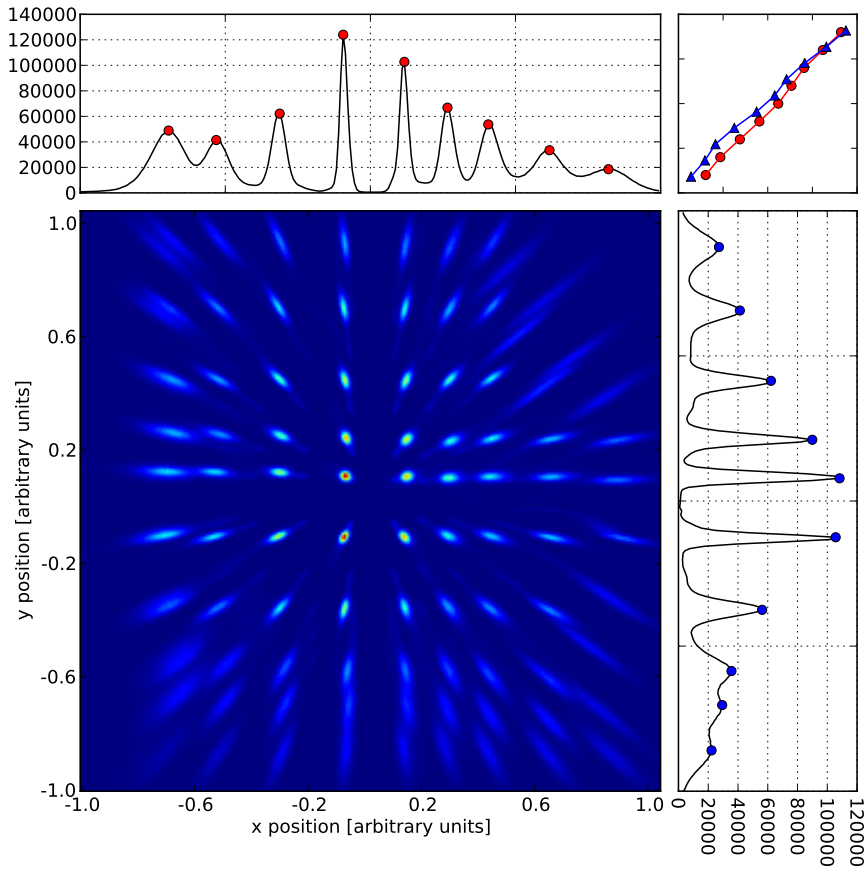
### 7.2.1. Energy calibration

The Tracker was calibrated using a single source, the only one showing a detectable Compton edge among those at our disposal. The source signals are overwhelmed by the low energy noise and the spectrum is not reliable for a Compton edge determination. In figure 7.5 we can see the two sources spectra with the background subtracted and the background itself to give an idea of the superposition region with the source. With only one point of calibration we were unable to determine potential offsets. However we were not so interested in the energy resolution and performance of the tracking part, being these latter assessed through the calorimeter. To calibrate with the Compton edge we used the technique described in [Hri+90].

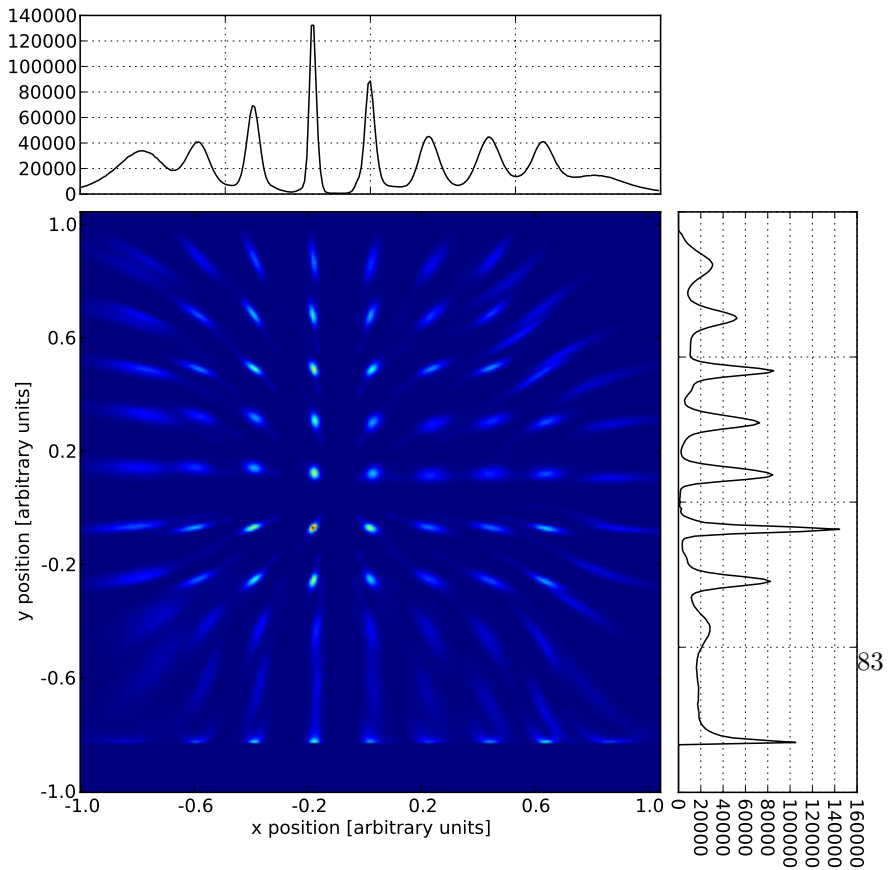
### 7.2.2. Photomultiplier spatial linearization

Using the same LED pulser as for the Calorimeter, we acquired the dot grid with the Tracker, and obtained similar results (Figure 7.6 on the next page). The LED had to be dimmed because of the higher amplification of the Tracker circuit. The resolution varies depending on the distance from the center and goes from 1 mm to 4 mm. Artifacts are worse, though, because the circuit was working on its dynamic range limit and the higher amplification generated too much low energy noise.





(a) Raw version with spline interpolation



(b) Linearized version

Figure 7.6.: Dots generated in an uniform mesh with a LED and acquired with the Tracker.

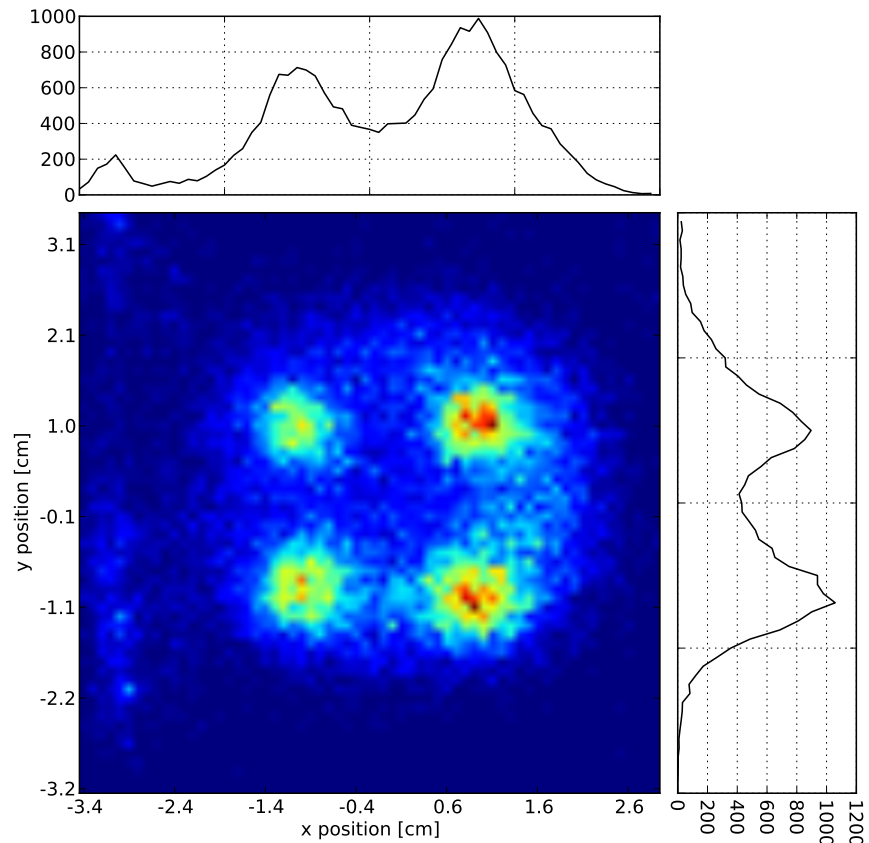


Figure 7.7.: Dots generated with a  $^{57}\text{Co}$  source and acquired with the Tracker.

### 7.2.3. Continuous scintillator spatial calibration

The same set-up for the spatial calibration of the Calorimeter was used for the Tracker with the continuous scintillator. The image, in figure 7.7, shows a resolution of 5 mm.

### 7.2.4. Continuous scintillator uniformity

Figure 7.8 on the next page shows us the uniformity of the Tracker with the continuous scintillator. The results are better than the Calorimeter and the usable surface is about the whole scintillator.

### 7.2.5. Segmented scintillator spatial calibration and uniformity

Figure 7.8 on the facing page shows us the uniformity of the Tracker with the segmented scintillator. Obviously, being segmented, we just used the uniformity image also for the spatial calibration. The image was a little

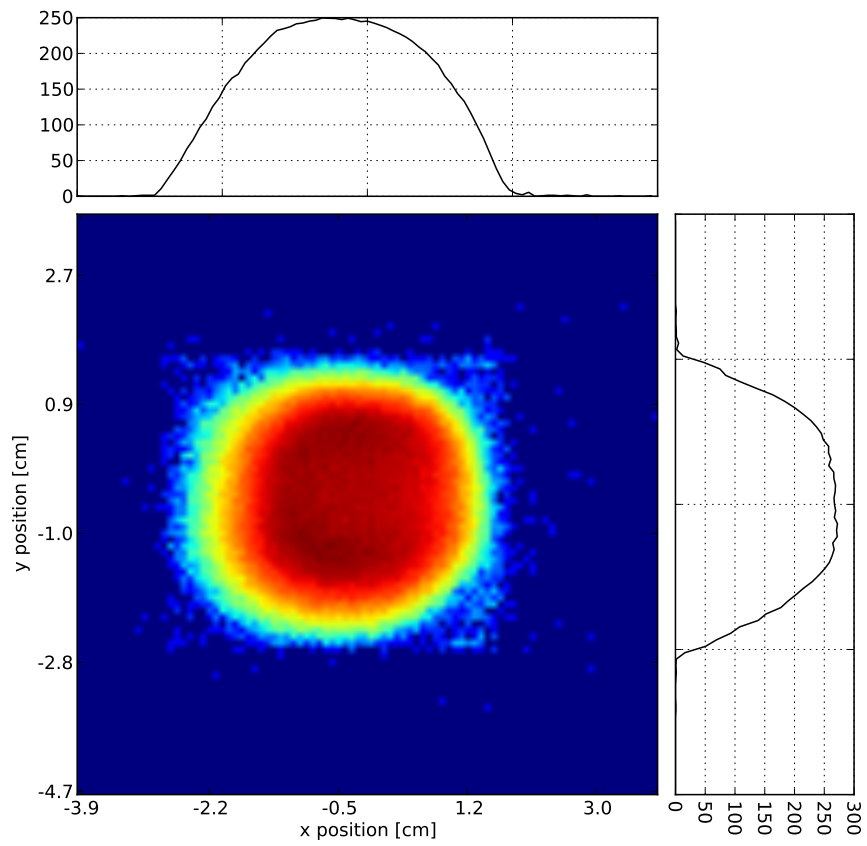
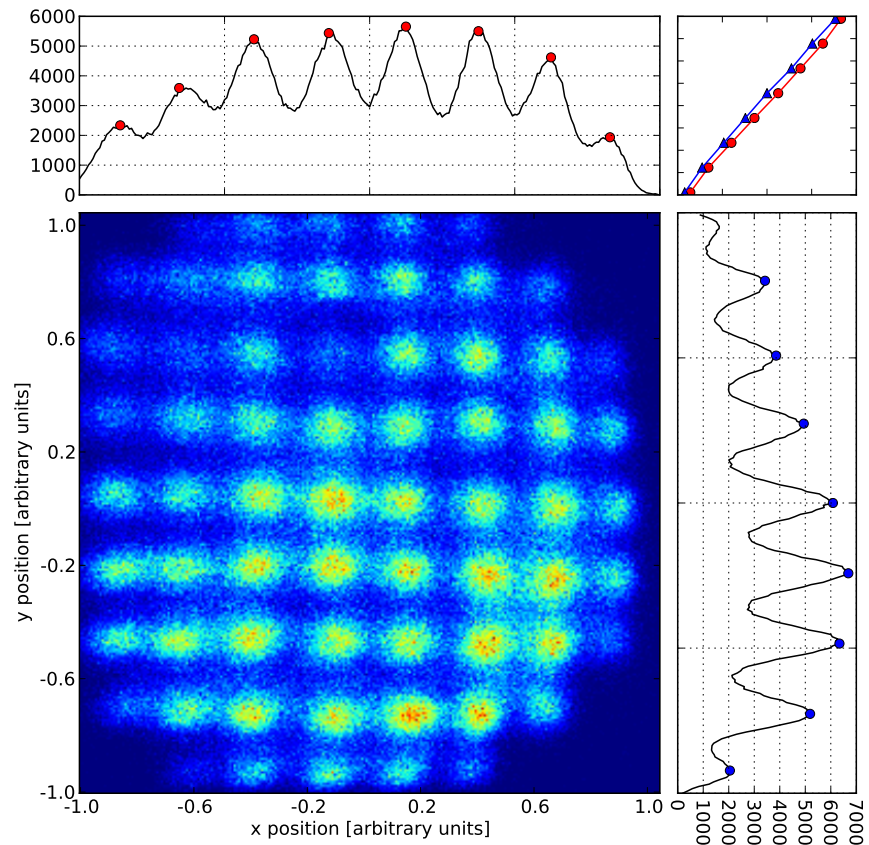
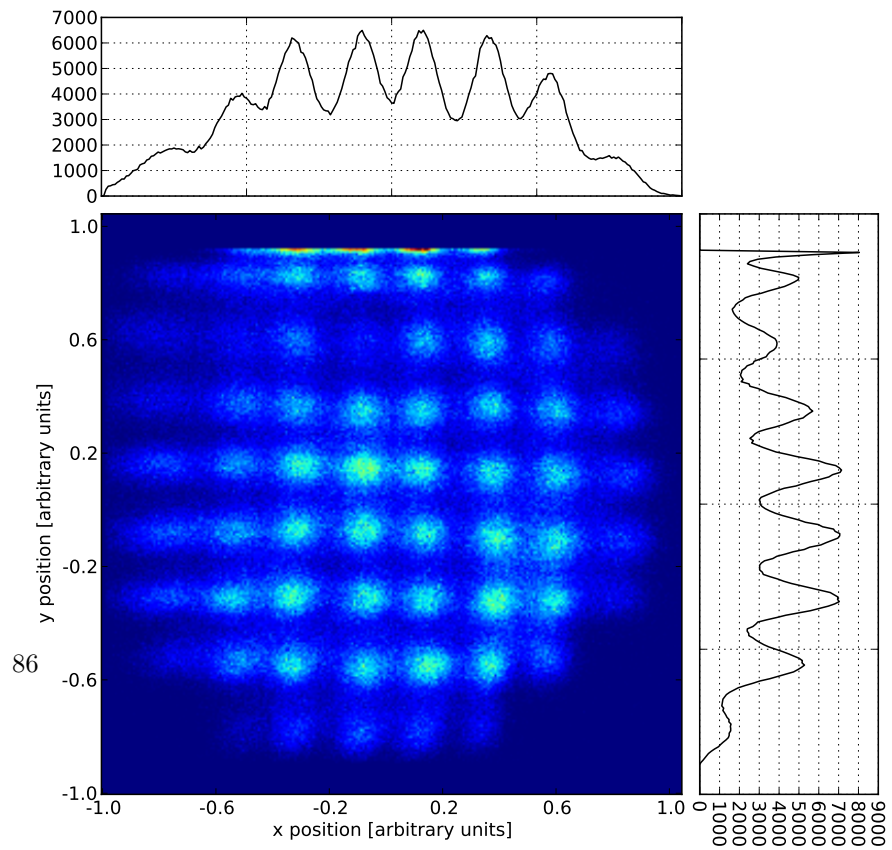


Figure 7.8.: Tracker uniformity with the continuous scintillator.



(a) Raw version with spline interpolation



(b) Linearized version

Figure 7.9.: Uniformity image of the Tracker with the segmented scintillator.

sheared (slanted toward one direction) and it was straightened using a *shear matrix* of the form [Wei]

$$T(k) = \begin{pmatrix} 1 & k \\ 0 & 1 \end{pmatrix} \quad (7.1)$$

where  $k$  is defined as

$$k = \arctan(\delta) \quad (7.2)$$

where  $\delta$  is the slanting angle. The single pillars (4 mm×4 mm) are easily distinguished, they show a good spatial linearity, even before the spline linearization (Figure 7.9 on the preceding page), and almost the whole extent of the scintillator can be seen.



## 8. Image formation model

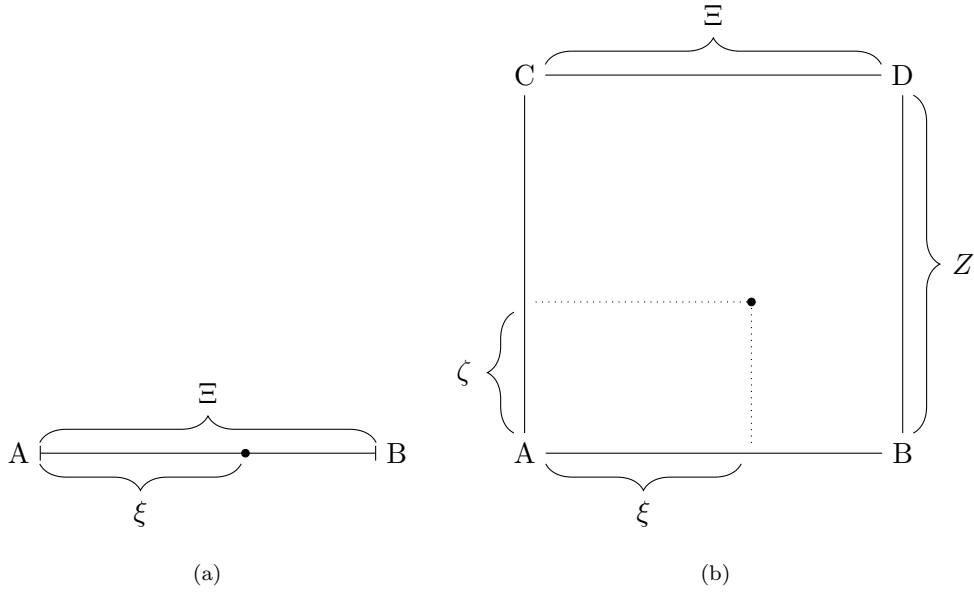


Figure 8.1.: Diagrams of a monodimensional coordinate system and a bidimensional one.

To analyze the spatial calibration images, we developed a simple Monte Carlo code to simulate the preamplifier signals. We can define an equation for a monodimensional coordinate, in much the same way as in equations (5.2) and (5.3) on page 48:

$$x = \frac{V_A - V_B}{V_A + V_B} \quad (8.1)$$

Picturing the situation in figure 8.1 we can see that if we define  $V_A$  and  $V_B$  as

$$V_A = \xi, \quad V_B = \Xi - \xi, \quad (8.2)$$

we get the right solution for equation 8.1:

$$x = \frac{\xi + \xi - \Xi}{\Xi} = 2 \frac{\xi}{\Xi} - 1; \quad (8.3)$$

that is a coordinate in the interval  $x \in [-1, 1]$ .

Extending the reasoning to a bidimensional case we have:

$$V_A = \xi + \zeta, \quad V_B = \Xi - \xi + \zeta, \quad V_C = \xi + Z - \zeta, \quad V_D = \Xi - \xi + Z - \zeta, \quad (8.4)$$

that gives us

$$x = \frac{2\xi + Z - (2\Xi - 2\xi + Z)}{2\Xi + 2Z} = 2 \frac{\xi}{\Xi + Z} - \frac{\Xi}{\Xi + Z} \quad (8.5)$$

and

$$y = \frac{2\zeta + \Xi - (2Z - 2\zeta + \Xi)}{2\Xi + 2Z} = 2 \frac{\zeta}{\Xi + Z} - \frac{Z}{\Xi + Z}; \quad (8.6)$$

that are coordinates in the intervals

$$x \in \left[ -\frac{\Xi}{\Xi + Z}, \frac{\Xi}{\Xi + Z} \right], \quad y \in \left[ -\frac{Z}{\Xi + Z}, \frac{Z}{\Xi + Z} \right]. \quad (8.7)$$

Now that we have a model for generating the four resistor net signals, we can produce an image of a grid of point-like sources 5 mm apart, see figure 8.2 on the next page for an example image with a spatial resolution of 0.25 mm (0.5%).

The star-like effect that can be seen on the spatial calibration measurements can be modeled by a casual variation of an offset in the signals. Recalling equations (5.2) and (5.3) on page 48, we see that if we add an offset to the signals the effect is a multiplication factor in the formula result, because the offset gets completely cancelled on the numerator while it is kept in the denominator. Thus, adding a casual offset to the simulated data we should see a smearing along directions coming from the center of the image. Those star-like formations are more pronounced in the image periphery, because those areas are more subject to a scale transformation being farther from the center. In figure 8.3 on page 92 we see the same grid of point-like sources smeared by a gaussian offset with  $\sigma = 3\%$ .

The simulated effect well describes the star-like formations of the real data, but fails to describe the effect on the corners. Real data are not laid on a regular grid on the corner and move toward the center. When a signal is generated near the output connection has its maximum height (Figure 5.21 on page 68), and thus the corners are critical regions because the signals can saturate the preamplifier. A possible solution for the simulation is to introduce a trim on the data to imitate the saturation. Trimming the signals will move the points toward the center, because their values are lowered toward their average. In figure 8.4 on page 93 we see the same grid of point-like sources smeared by a gaussian offset with  $\sigma = 3\%$  and with a saturation effect at the 80% of the maximum signal. Now the simulation is able to correctly reproduce the real data artifacts.



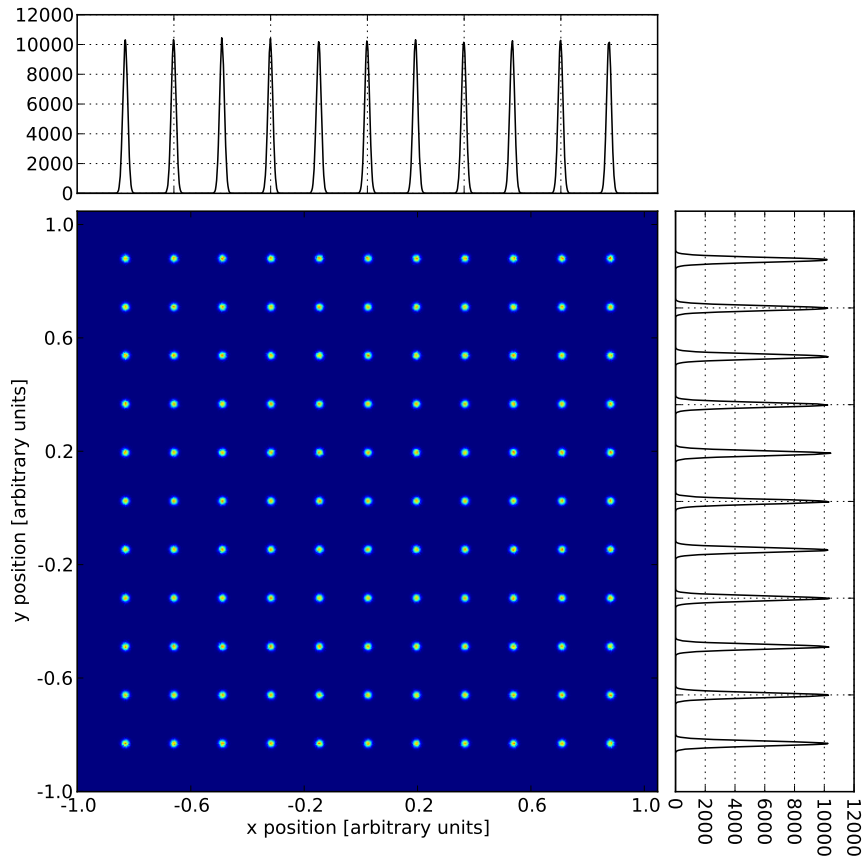


Figure 8.2.: Monte Carlo generated signals of a grid of point-like sources 5 mm apart, spatial resolution is 0.25 mm (0.5%).

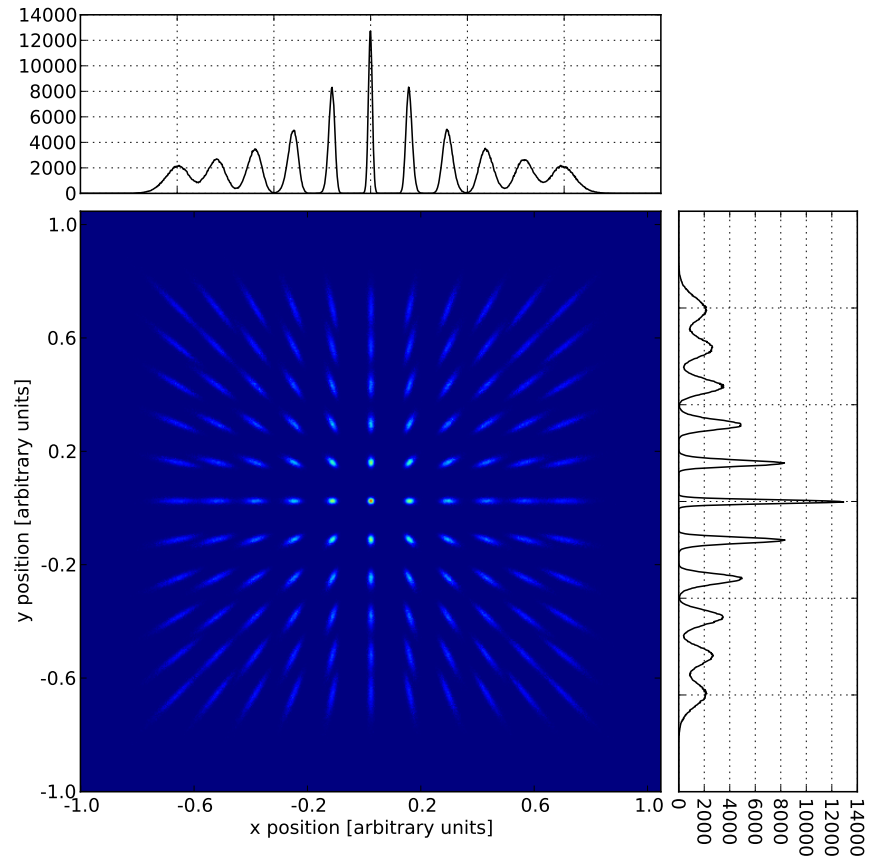


Figure 8.3.: Monte Carlo generated signals of a grid of point-like sources 5 mm apart, spatial resolution is 0.25 mm (0.5%) and a gaussian offset is added to the signals, with  $\sigma = 3\%$ .

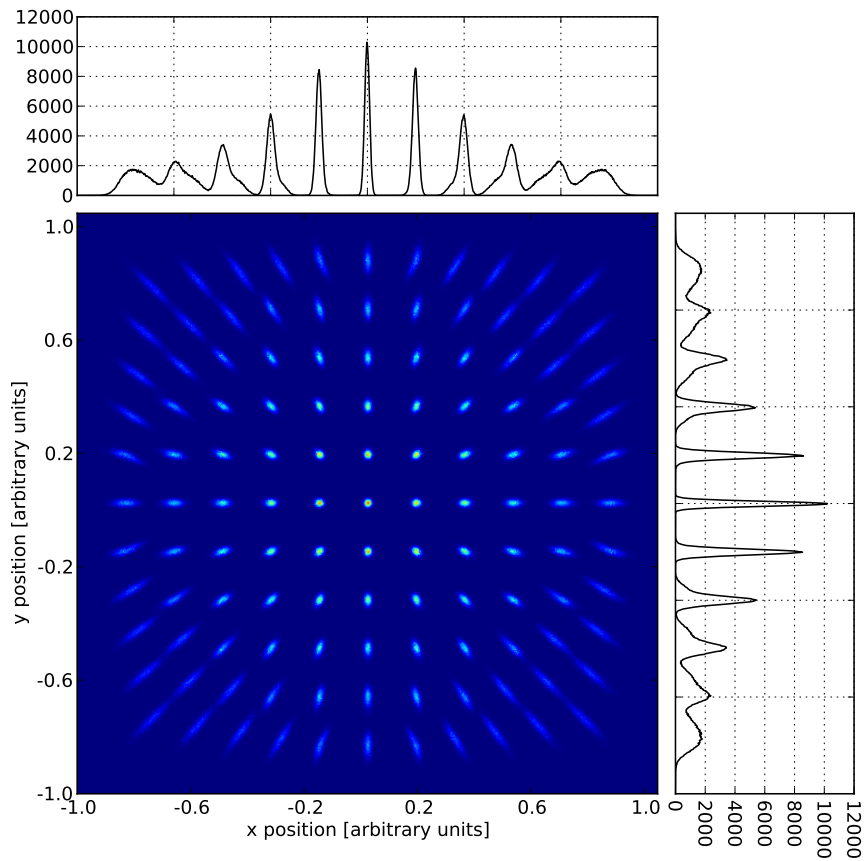


Figure 8.4.: Monte Carlo generated signals of a grid of point-like sources 5 mm apart, spatial resolution is 0.25 mm (0.5%), gaussian offset is added to the signals, with  $\sigma = 3\%$ , and a saturation effect at the 80% of the maximum signal.



## 9. Collimated images

The detector was also used as a traditional gamma camera employing a parallel holes lead collimator. The lead collimator has 0.5 mm hexagonal holes, 0.2 mm septa, and it is 20 mm thick. We mounted this good collimator on the Calorimeter and disabled the Tracker, using only the inorganic scintillator as the gamma detector. In figure 9.1 on the following page we can see an image of a point-like source, the resolution is 3 mm. In figure 9.2 on page 97 we can see an image of a circumference-like source of radius 10 mm, the resolution is still 3 mm.

Although the apparatus main objective is Compton imaging, we can use it as a traditional collimated gamma camera with a resolution suitable for small animal imaging, such as rats and rabbits. Plus, substituting the plastic scintillator with another  $\text{LaBr}_3$  scintillator, the system could be applied for Positron Emission Tomography imaging, because it is designed to acquire on the coincidences between the two detectors.

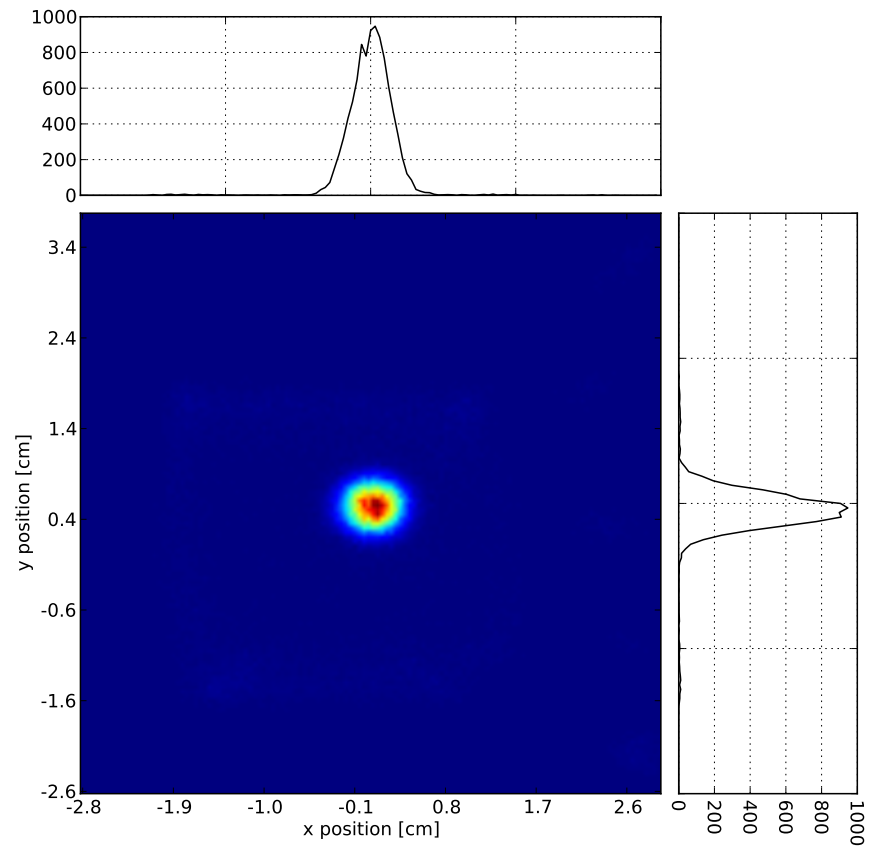


Figure 9.1.: Point-like  $^{57}\text{Co}$  source in front of the Calorimeter with a parallel holes lead collimator.

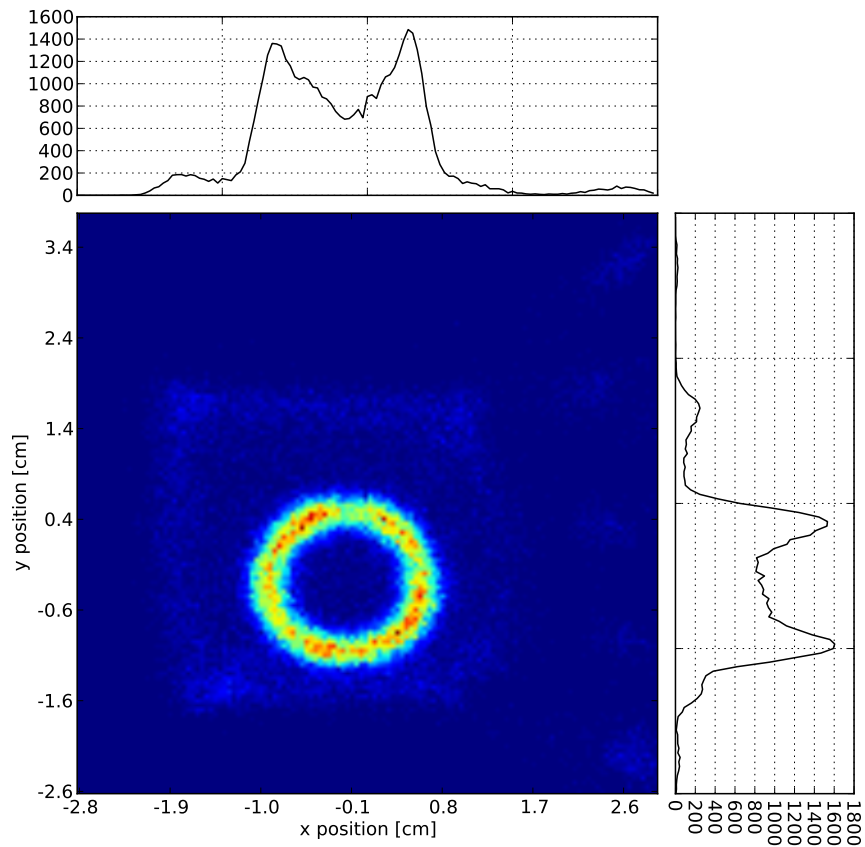


Figure 9.2.: Circumference-like  $^{57}\text{Co}$  source (radius 10 mm) in front of the Calorimeter with a parallel holes lead collimator.





## 10. Images using Compton scattered gamma-rays

Measurements of images using Compton scattered gamma-ray were taken with the same conditions of the Geant4 simulation, as in chapter 4 on page 39.

### 10.1. Detector spectra during coincidences

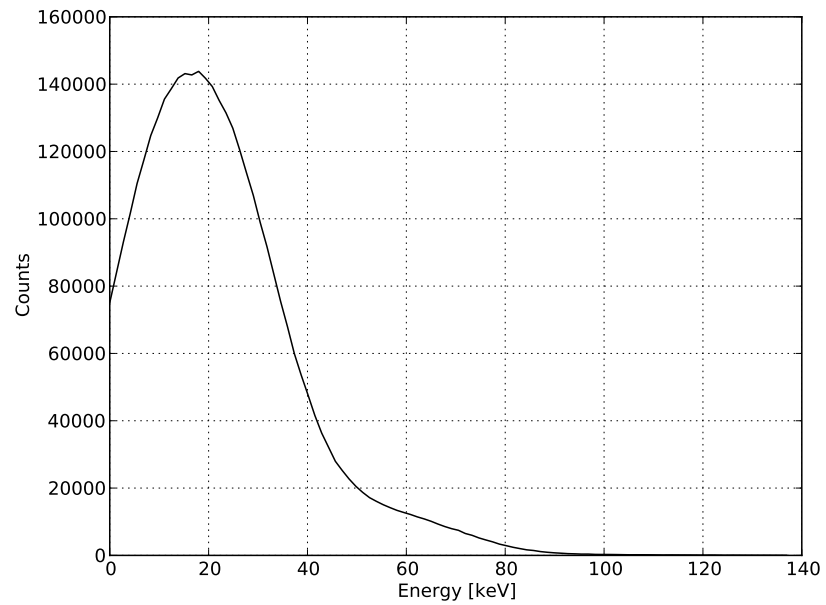
Obviously energy spectra change between data acquisitions with or without the coincidence activated. When the coincidence is activated the Calorimeter full-energy peak disappears and an excess of lower energy events becomes evident. The Tracker, on the other hand, does not show much difference because what is measured are still Compton interactions. In figure 10.1 on the next page there are some Geant4 simulations for the coincidence set-up and in figure 10.2 on page 101 there are real data taken with a  $^{57}\text{Co}$  source. The spectra look different but have a similarity, especially because the gamma energies are different and our Geant4 simulation was not aimed to a full detector reconstruction, but only to a reconstruction of Compton events.

### 10.2. Bidimensional energy spectrum

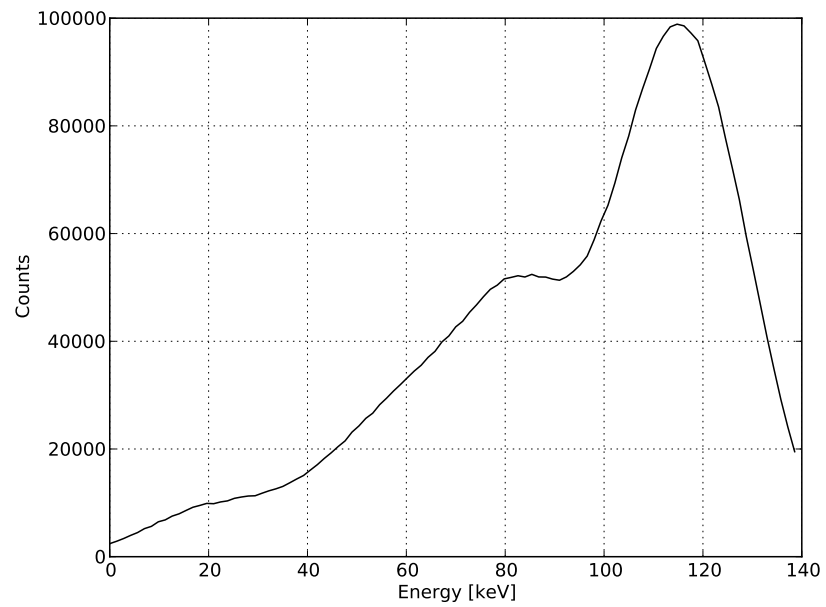
On the simulation we had the certainty that the selected gamma-rays underwent a Compton interaction inside the Tracker. In the real-life experiment we have to select the interesting events. Besides taking the coincidence between the detectors we developed a selection algorithm that takes into account the detectors energies. The selection is required because random coincidences add noise to the final image, thus reducing the quality. How should the selection look like? The relationship between the energies is

$$E = E_e + E' \quad \rightsquigarrow \quad E_e = E - E' \quad (10.1)$$

where  $E'$  is the energy measured by the Calorimeter and  $E_e$  is the energy measured by the Tracker. Thus the relationship is represented by a line that starts at the point  $(E, 0)$  and goes to the point  $(E - E_e^{\max}, E_e^{\max})$ . Plotting  $E_e$  versus  $E'$  gives us an insight of the relationship that the two energies should have and by selecting just the Compton region We used the Geant4 simulation to predict the bidimensional plot, adding an 18% energy uncertainty in both the detectors (although we suppose that the Tracker has a worse resolution). In figure 10.1 on the next page there are the simulated spectra and in figure 10.3 there is the bidimensional spectrum. On the bidimensional spectrum

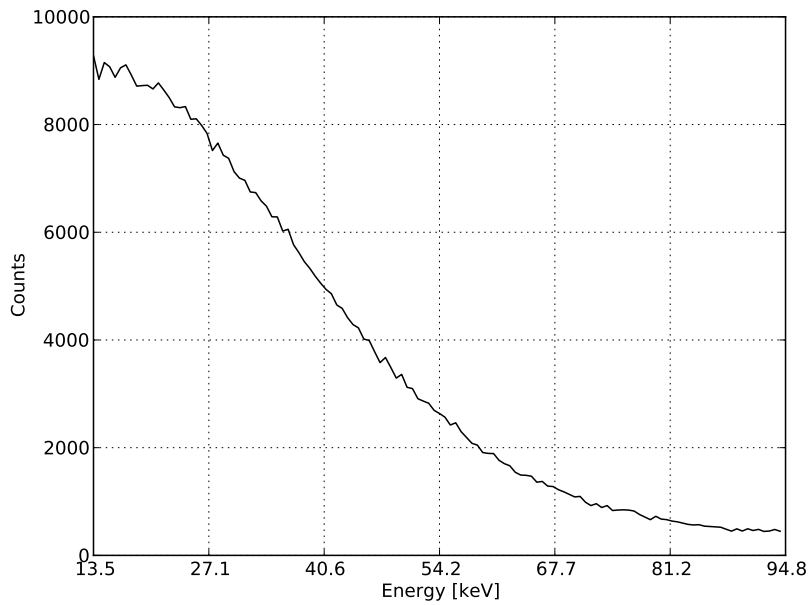


(a)

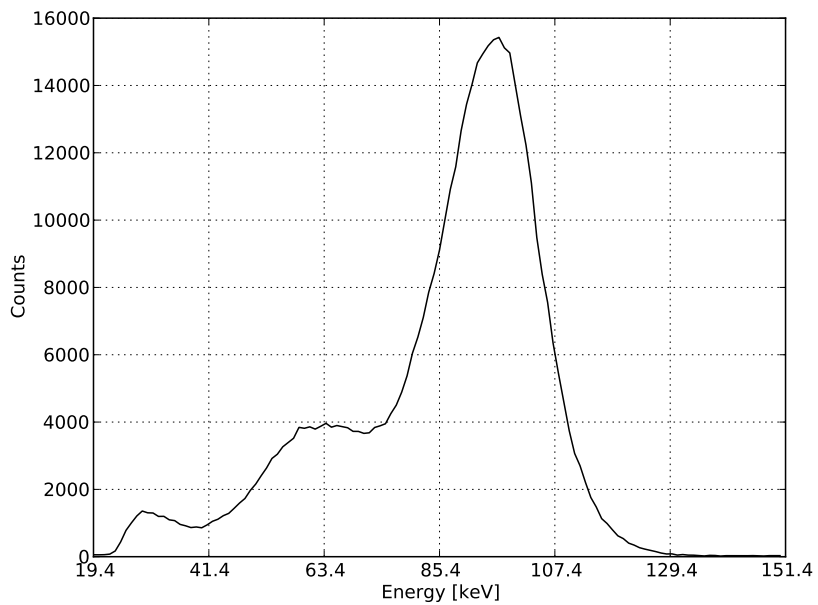


(b)

Figure 10.1.: Detectors spectra simulated with Geant4 for a 142 keV gamma source, energy uncertainty 18%.



(a)



(b)

Figure 10.2.: Detectors spectra of real data for a 122 keV gamma from a  $^{57}\text{Co}$  source, energy uncertainty 18%.

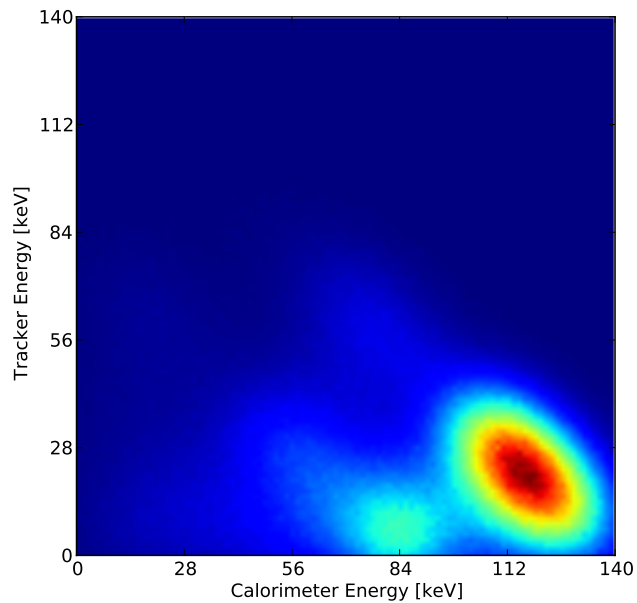


Figure 10.3.: Bidimensional energy histogram simulated with Geant4 for a 142 keV gamma source, energy uncertainty 18%.

there is an unexpected region under the main Compton region that is caused by the low-energy effects.

In figure 10.4 on the next page we can see an example of a bidimensional energy histogram obtained with real data from 122 keV gamma-rays of a  $^{57}\text{Co}$  source, on which we can isolate five distinct regions:

- (a) main Compton region;
- (b) second Compton region;
- (c) random coincidences with the Calorimeter full-energy;
- (d) random coincidences with the Calorimeter's  $^{138}\text{La}$  intrinsic radioactivity;
- (e) Tracker overflow with higher energy Compton interactions.

### 10.3. Compton Images

In figure 10.5 on page 104 we can see an image taken with a quasi-point-like  $^{57}\text{Co}$  source, 1 mm wide.

On the bidimensional spectrum a region around the Compton scattering peak was selected, with amplitude equal to the FWHM of the peak. The image shows different resolutions along the different directions, due to the

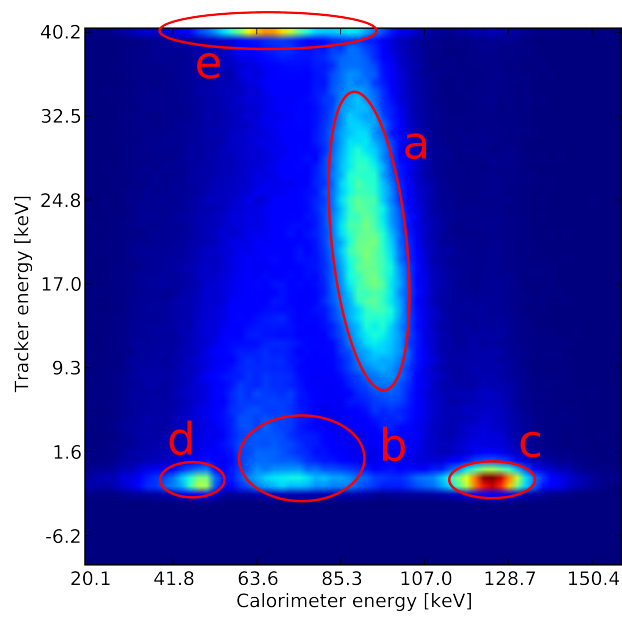


Figure 10.4.: Bidimensional energy histogram of real data for a 122 keV gamma from a  $^{57}\text{Co}$  source. (a) main Compton region, (b) second Compton region, (c) random coincidences between the Calorimeter full-energy peak and the Tracker, (d) random coincidences with the Calorimeter's  $^{138}\text{La}$ , (e) Tracker overflow with higher energy Compton interactions.

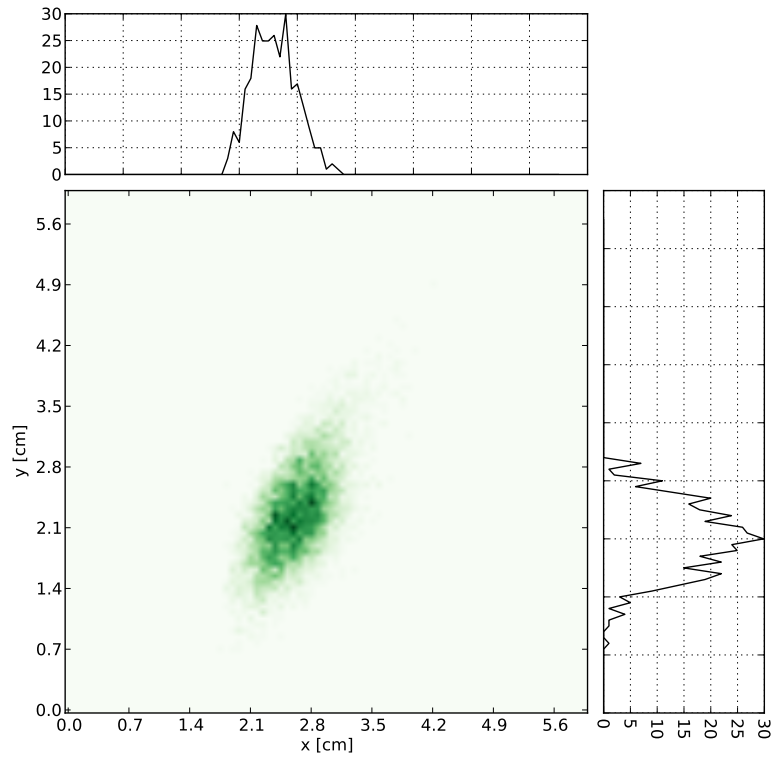


Figure 10.5.: Real Compton images of a quasi-point-like  $^{57}\text{Co}$  source, projected on the Tracker plane, selection on bidimensional spectrum FWHM wide.

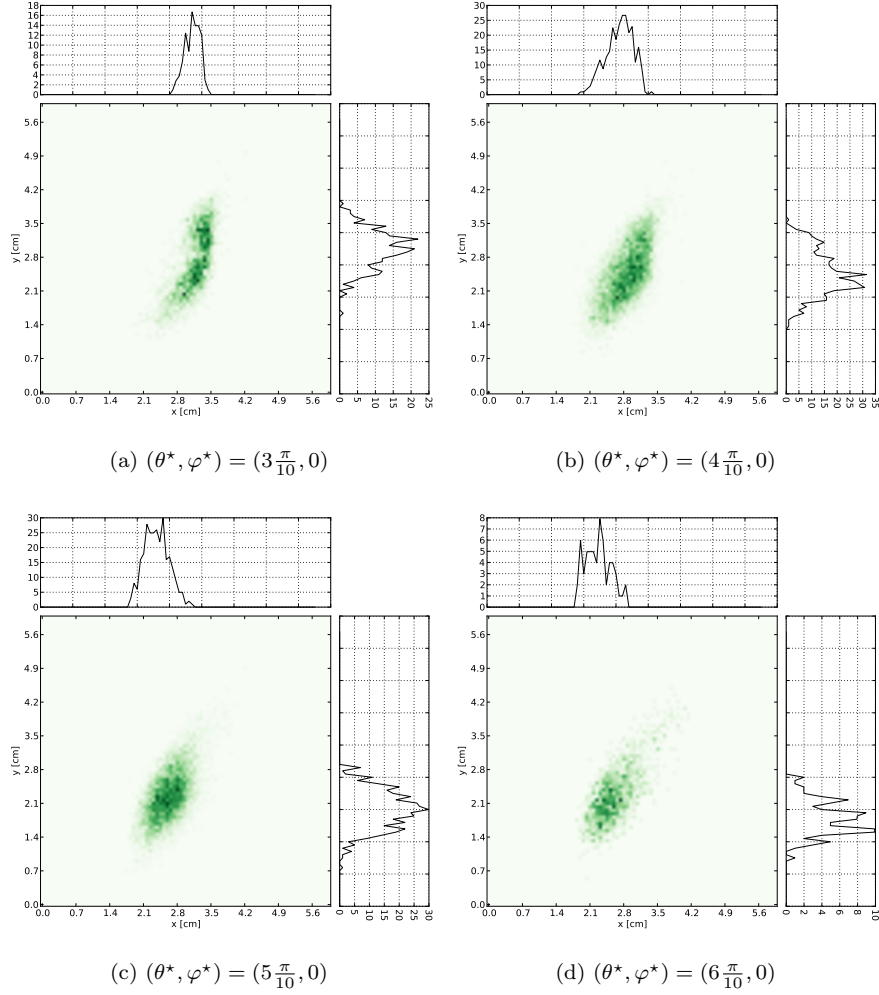


Figure 10.6.: Real Compton images of a quasi-point-like  $^{57}\text{Co}$  source, projected on the Tracker plane along different directions, selection on bidimensional spectrum FWHM wide.

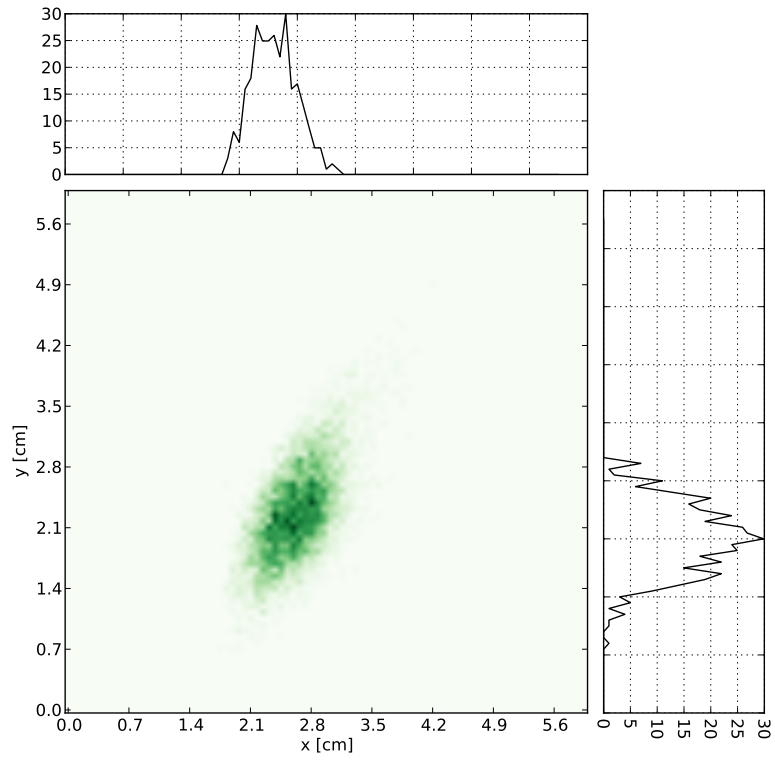


Figure 10.7.: Real Compton images of a quasi-point-like  $^{57}\text{Co}$  source, projected on the Tracker plane, selection on bidimensional spectrum FWHM/2 wide.



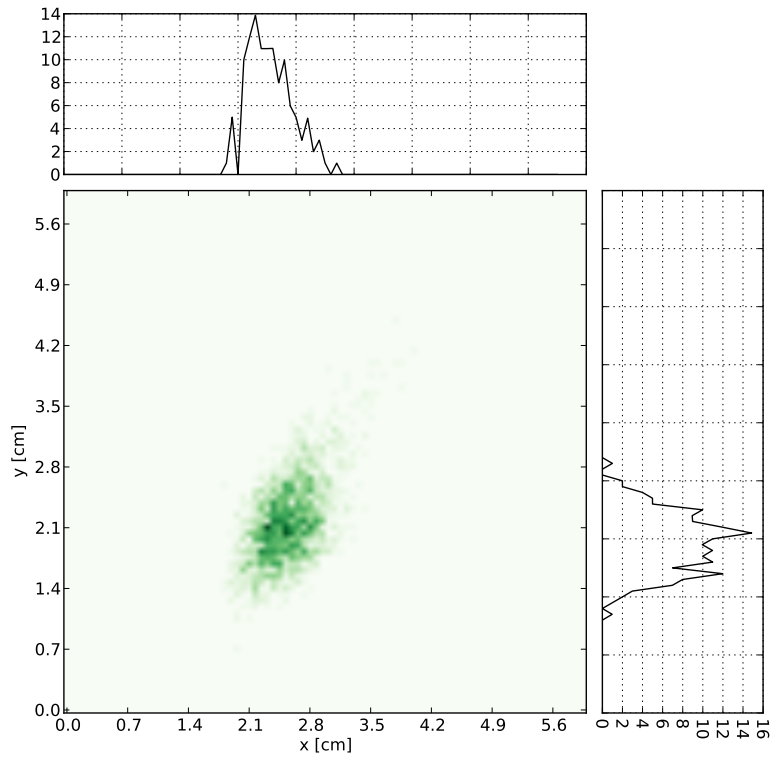


Figure 10.8.: Real Compton images of a quasi-point-like  $^{57}\text{Co}$  source, projected on the Tracker plane, selection on bidimensional spectrum FWHM/3 wide.

asymmetric geometry of the detector prototype. Along the  $x$  axis the FWHM is 8 mm and along  $y$  it is 9 mm. Taking into account that the source is 1 mm wide, on the  $x$  direction the resolution should be reduced by 1 mm, while on the  $y$  direction its dimensions are projected on the tracker plane inducing an apparent dimension of about 1.5 mm. The resolutions transform then into a comparable value of 7 mm. In figure 10.6 on page 105 we can see the source projected along different directions on the Tracker plane. In figure 10.7 on page 106 we can see the same image but with a tighter selection on the bidimensional spectrum, width is FWHM/2. Obviously the statistics is worse but the resolution is improved to 7 mm and 8 mm, for  $x$  and  $y$  respectively, that transform into 6 mm. The last image (Figure 10.8 on the previous page) shows an even tighter selection, FWHM/3 wide, and a resolution comparable to the preceding image.

## 11. Conclusions

In this thesis we present the R&D of a Compton Camera (CC) for small object imaging. The CC concept requires two detectors to obtain the incoming direction of the gamma ray. This approach, sometimes named “Electronic Collimation”, differs from the usual technique that employs collimators for physically selecting gamma rays of a given direction. The challenge we had to face was the development of high precision energy and position measurement methods, a very accurate camera simulation, and an original reconstruction algorithm.

The first detector constitutes the scattering volume in which gamma-rays undergo the Compton interaction, while the second detector completely absorbs the scattered gamma-rays. The latter detector is a photomultiplier coupled to a high-Z inorganic scintillator. The former detector is usually a very thin silicon detector that exhibits both a good spatial resolution and energetic resolution [rossi2011; Fon+11]. We propose a new concept to dramatically reduce the research and development costs, in this work we substituted the silicon tracker with a plastic scintillator coupled to a photomultiplier. We could use the same readout electronics for both Tracker and Calorimeter and reduce the electronics complexity and costs. The plastic scintillator is the optimum choice for a scintillator because it has the maximum probability of Compton interactions for gamma-rays.

The Monte Carlo simulation was developed with the toolkit Geant4 and its results were presented in international conferences [Ros+11a; Ros+11b; Fon+11]. The original algorithm is used to reconstruct the images by analyzing the Compton interactions of gamma-rays inside the detector. Due to the peculiarities of the interaction, the experimental data have to be elaborated before producing images. The algorithm can be used for on-line reconstruction because the code was written as much optimized as possible, but at the same time it was written in a high-level language and thus does not rely on a particular architecture or operating system. We are able to produce images that are projections of the source biodistribution on a plane along different directions, using only one acquisition because we infer the directions of the gamma-rays. The algorithm as well was presented in international conferences [Ros+11a; Ros+11b; Fon+11]. The resolution obtained on simulated images is not isotropic, on the  $x$  direction it is 2 mm and on the  $y$  direction it is 4 mm. This resolution represents a lower bound for the experimental images, and it is mostly due to the Doppler effect caused by electrons tighter bound to the scattering material.

To improve the image quality we also developed the original technique of the analysis of the bidimensional spectrum of the detected energies. Studying such spectrum we are able to select only the region of interest that corresponds to the Compton interaction. We also showed how different selections of regions

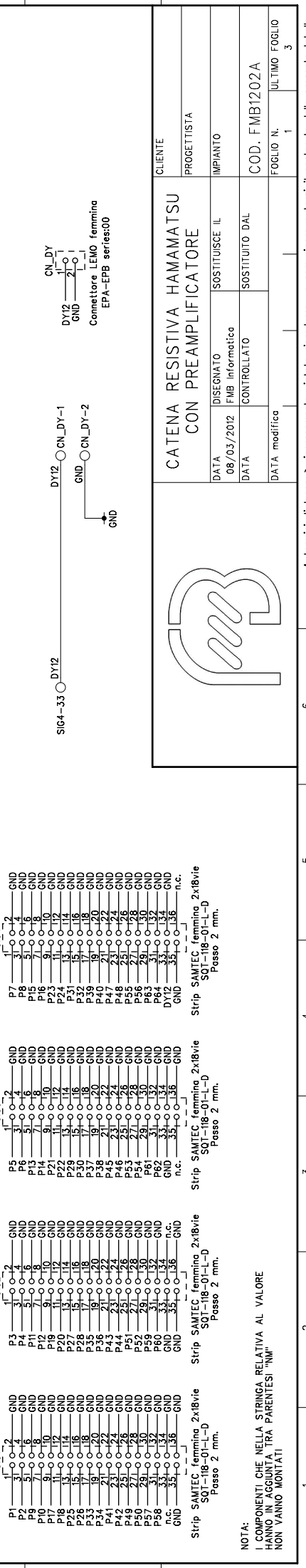
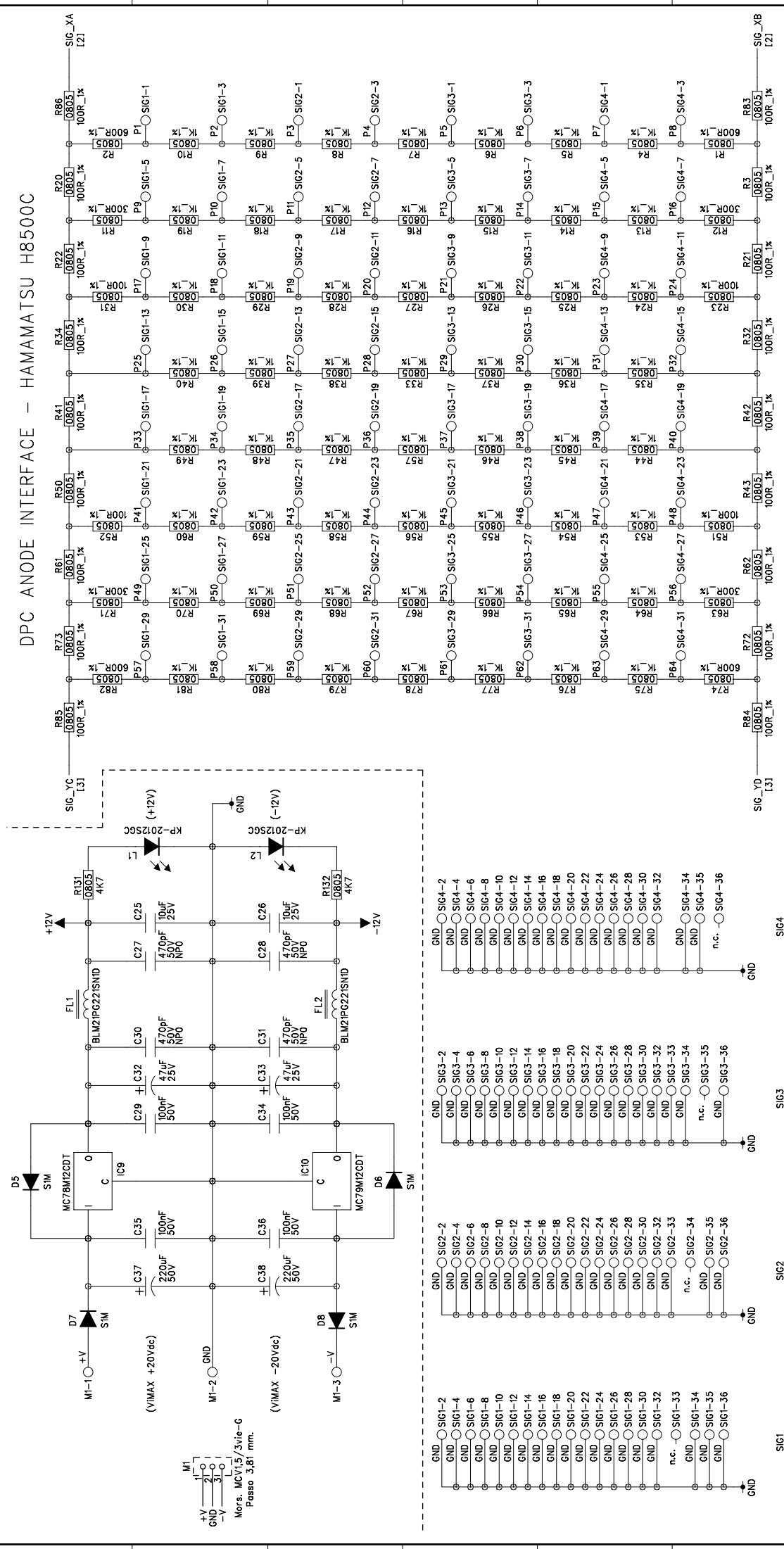
of interest induce an improvement of the image resolution of experimental data.

The experimental apparatus was built and tested in the Laboratory for Radiopharmaceuticals and Molecular Imaging (*Laboratorio di Radiofarmaci ed Imaging Molecolare*, LRIM) at the National Laboratories of Legnaro (PD), Italy (*Laboratori Nazionali di Legnaro*, LNL). To construct it we used some custom-made electronics realized with the collaboration of an external company (FMB Informatica s.n.c., Bassano del Grappa, VI, Italy). Employing a Charge Multiplexing circuit we were able to reduce the number of analog channels from 128 to only 8, and thus we reduced the acquisition complexity. The detector electronics is very compact, cheap and easily transportable. The realized prototype is suitable only for small objects imaging due to his small size of 5 cm, but it has been designed as a modular component that can be extended, putting more modules side by side. We demonstrated that the detector and acquisition system can be used both as a traditional collimated gamma-camera and as a Compton camera. Using it as a collimated camera we were able to achieve a resolution of 3 mm, for a quasi-point-like  $^{57}\text{Co}$  source at 2.5 cm from the detector. This resolution is suitable to small animal imaging, such as rats, rabbits, *etcetera*, and it is suitable to small human organs imaging, such as thyroid or prostate. Using the prototype as a Compton camera we were able to achieve a resolution of 6 mm, with the same geometry as before, that is still applicable for small animal imaging and human imaging. The bonus of the Compton approach is the higher statistics available because of the lack of a collimator, and the possibility of using higher energy sources than the traditional sources used in Diagnostic Nuclear Medicine.

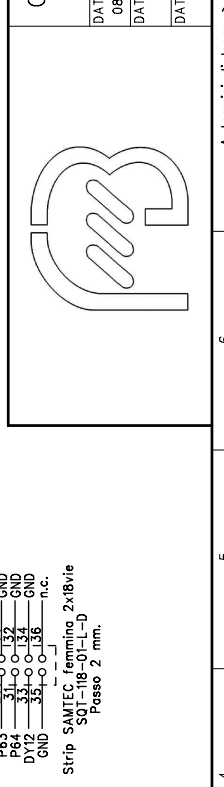
The obtained resolution can still be improved with thinner scintillators or with highly segmented scintillators (less than a millimeter stride). The Charge Multiplexing circuit can also be used with position sensitive photomultipliers with a higher subdivision than the used Hamamatsu 8500, that is subdivided in 64 parts, such as the Hamamatsu 9500, 256 parts. Further investigations are required for determining the implications of the exploit of a higher segmented photomultiplier. We also want to determine the dependency of the resolution depending on the distance from the detector and on the geometry of the detectors. With the reconstructed images we can also employ Tomographic 3D reconstruction algorithms for the reconstruction of the biodistribution of radioactive sources. The prototype was designed to be a modular element that can be extended placing more similar detectors side by side.

## A. Charge Multiplexing and Preamplifier PCB

# DPC ANODE INTERFACE - HAMAMATSU H8500C



CLIENTE	
PROGETTISTA	
CATENA RESISTIVA HAMAMATSU CON PREAMPLIFICATORE	
DATA	08/03/2012
DESIGNATO	FMB Informatico
SOSTITUISCE IL	
DATA	CONTROLLATO
SOSTITUITO DAL	
DATA	modificata
COD. FMB1202A	
FOLIO N.	1
ULTIMO FOGLIO	3



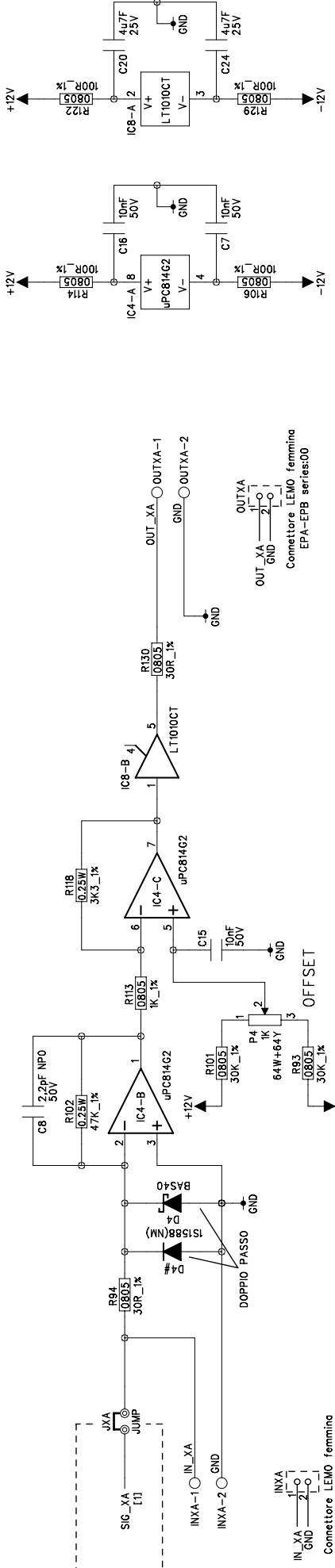
Strip SAMTEC femmina 2x8vBe  
SO1-118-0J-L-D  
Passo 2 mm.

Strip SAMTEC femmina 2x8vBe  
SO1-118-0J-L-D  
Passo 2 mm.

Strip SAMTEC femmina 2x8vBe  
SO1-118-0J-L-D  
Passo 2 mm.

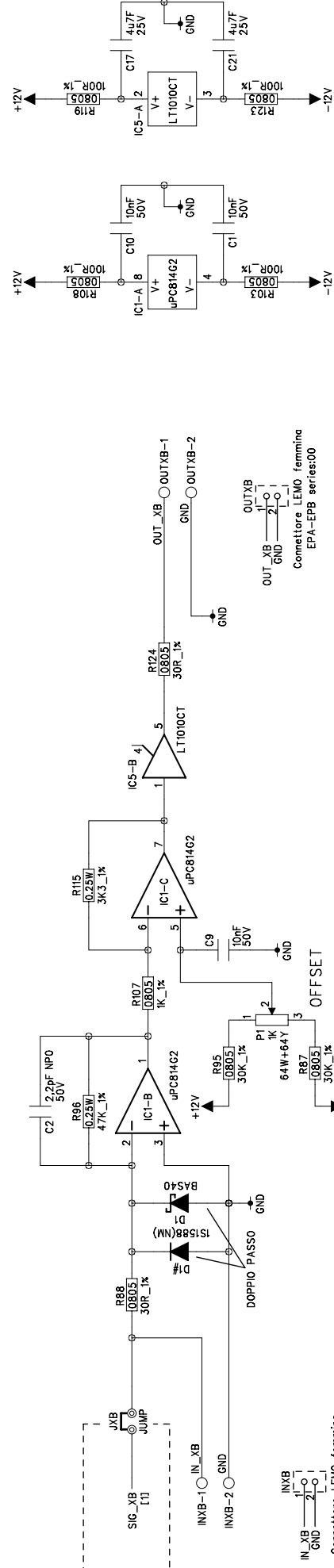
Strip SAMTEC femmina 2x8vBe  
SO1-118-0J-L-D  
Passo 2 mm.

NOTA:  
I COMPONENTI CHE NELLA STRINGA RELATIVA AL VALORE  
HANNO IN AGGIUNTA TRA PARENTESI "MM"  
NON VANNO MONTATI



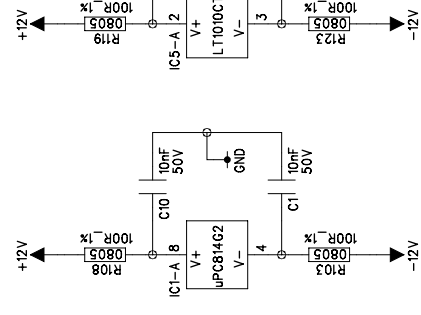
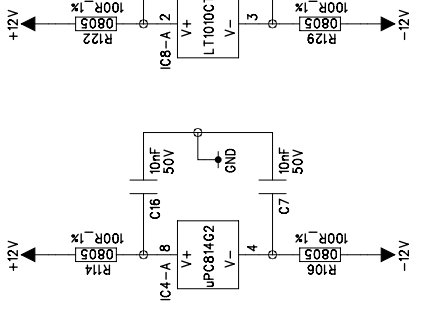
IN\_XA  
 1-0  
 GND 2-1  
 Connettore LEMO femmina  
 EPA-EPB series:00 (NM)

OUTXA  
 1-0  
 GND 2-1  
 Connettore LEMO femmina  
 EPA-EPB series:00

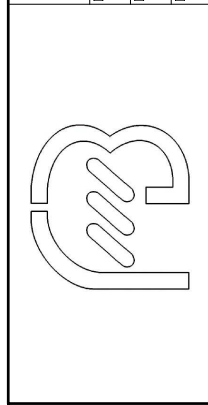


IN\_XB  
 1-0  
 GND 2-1  
 Connettore LEMO femmina  
 EPA-EPB series:00 (NM)

OUTXB  
 1-0  
 GND 2-1  
 Connettore LEMO femmina  
 EPA-EPB series:00



CLIENTE		CATENA RESISTIVA HAMAMATSU CON PREAMPLIFICATORE	
PROGETTISTA			
IMPIANTO	SOSTITUISCE IL		
DATA	08/03/2012	FMB Informatico	
DATA	CONTROLLATO		SOSTITUITO DAL
DATA	modifico		COD. FMB1202A
FOLGIO N.	2	ULTIMO	FOLGIO
			3

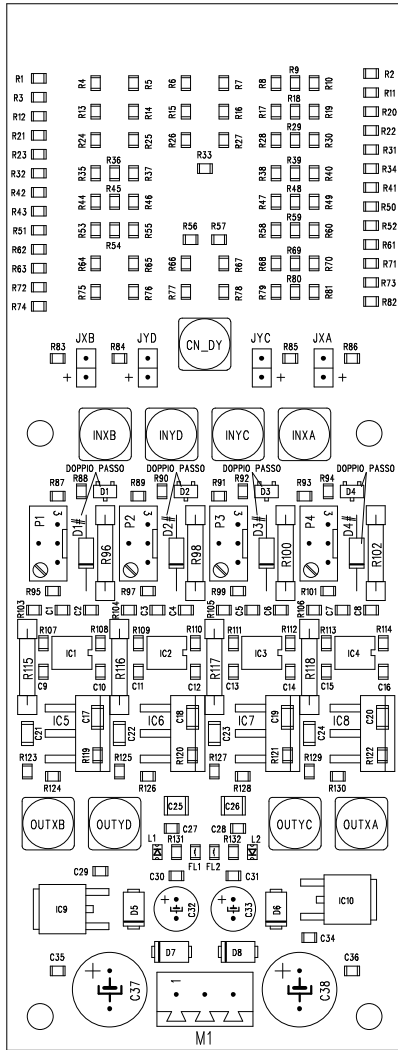


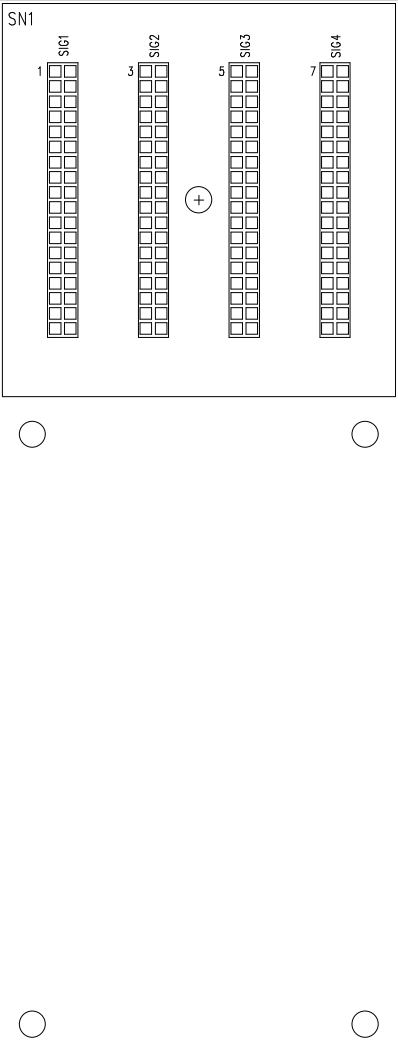
NOTA:  
 I COMPONENTI CHE NELLA STRINGA RELATIVA AL VALORE  
 HANNO IN AGGIUNTA TRA PARENTESI "NM"  
 NON VANNO MONTATI

A termini di legge è rigorosamente vietato riprodurre o comunicare a terzi il contenuto della presente tabella.

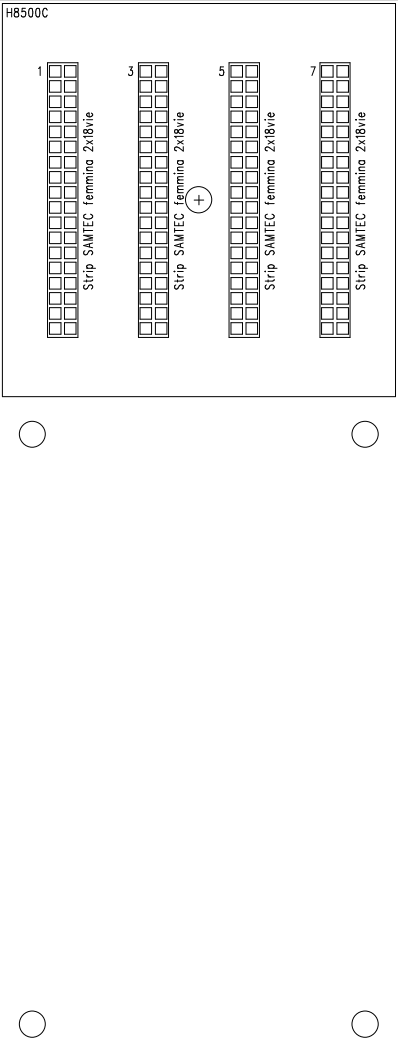




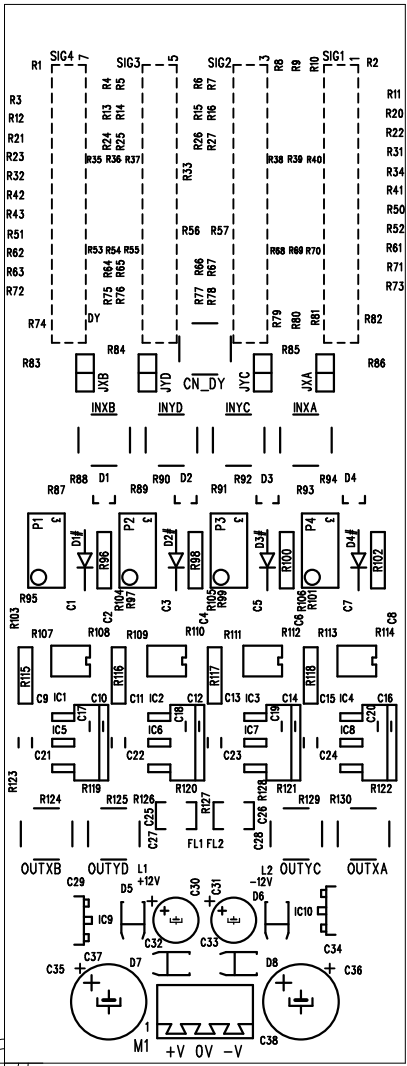




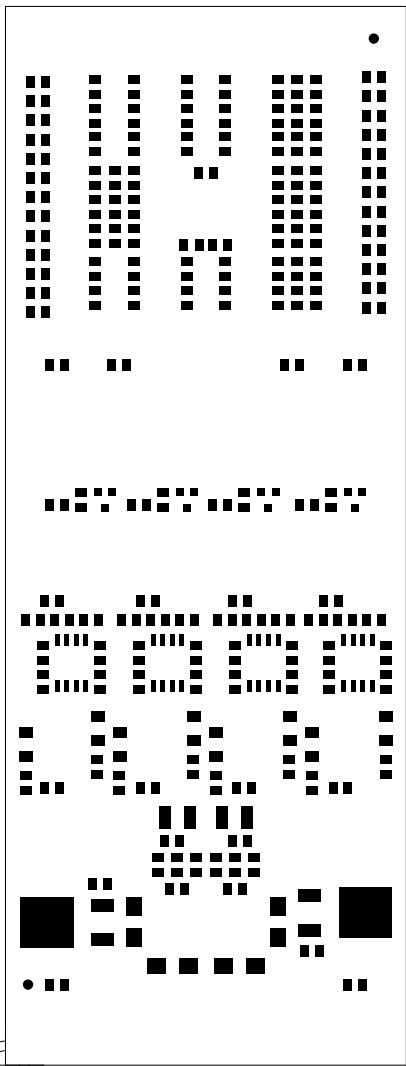




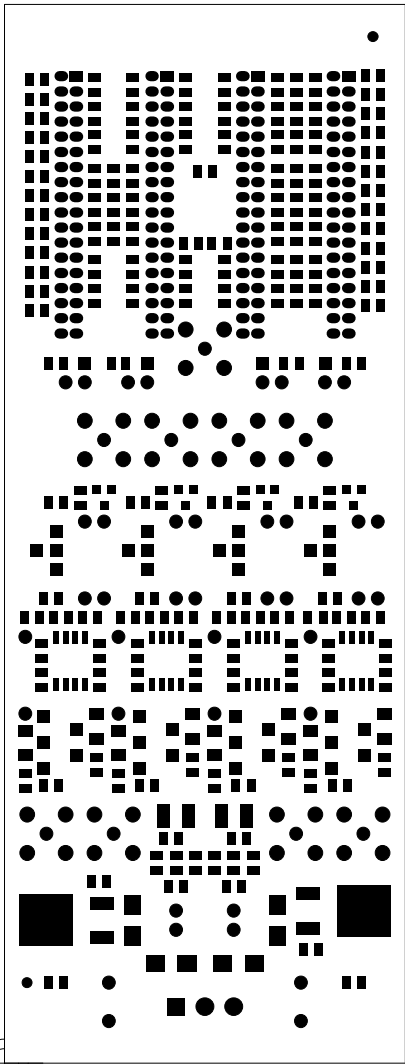
 FMB Informatica	DESCRIZIONE: SERIGRAFIA (TOP)	
	CLIENTE: INFN	
	CODICE : FMB1202A	
	NOTE: RAME=35um. FR4/SPESSORE C.S. 1,6mm	DATA: 08/03/2012



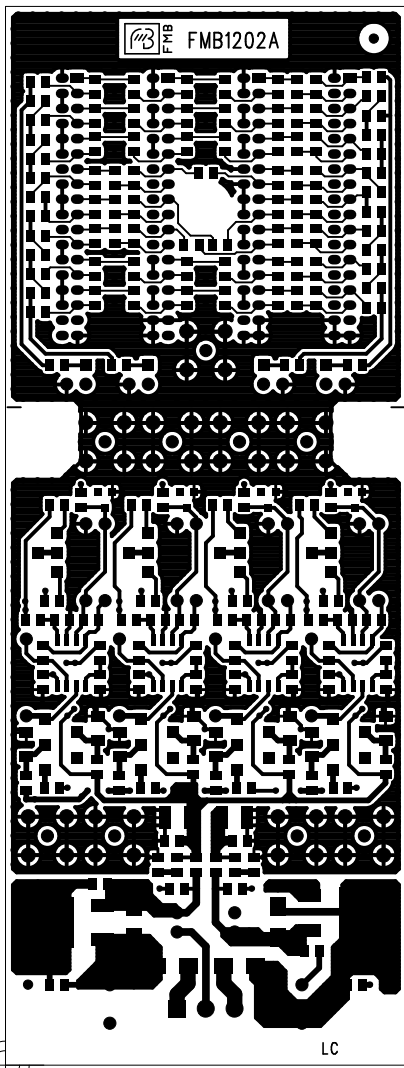
 FMB Informatica	DESCRIZIONE:	
	PASTA SALDANTE SMD (TOP)	
	CLIENTE: INFN	
	CODICE : FMB1202A	
	NOTE: RAME=35um. FR4/SPESSORE C.S. 1,6mm	DATA: 08/03/2012



 FMB Informatica	DESCRIZIONE:	
	SOLDER MASK (TOP)	
	CLIENTE: INFN	
	CODICE : FMB1202A	
	NOTE: RAME=35um. FR4/SPESSORE C.S. 1,6mm	DATA: 08/03/2012

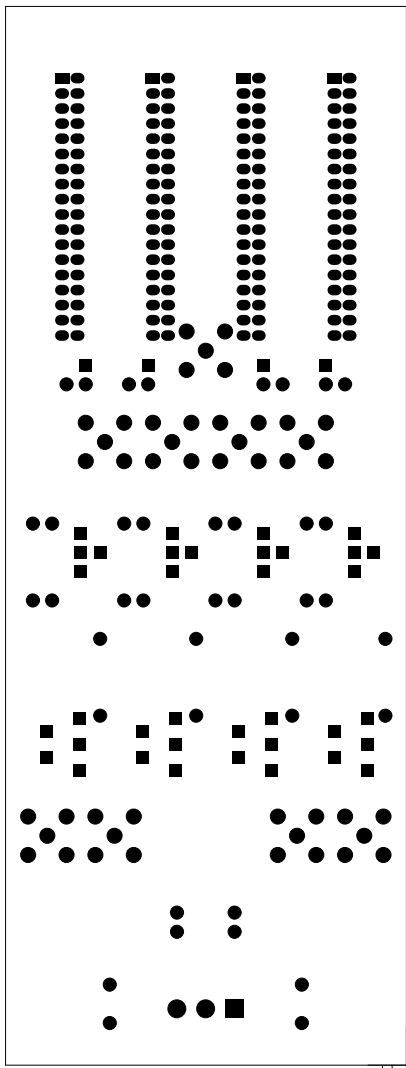



 FMB Informatica	DESCRIZIONE:	
	PISTE LATO COMPONENTI	
	CLIENTE: INFN	
	CODICE :FMB1202A	
NOTE: RAME=35um.	DATA:	
FR4/SPESSORE C.S. 1,6mm	08/03/2012	

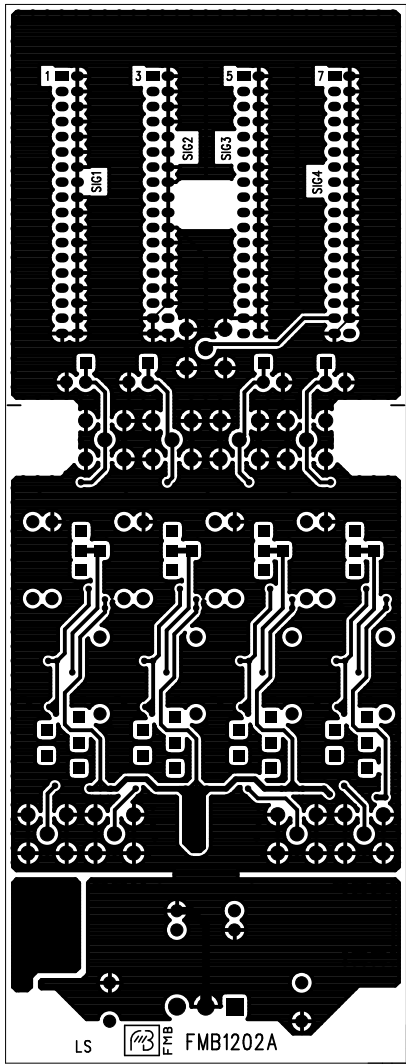




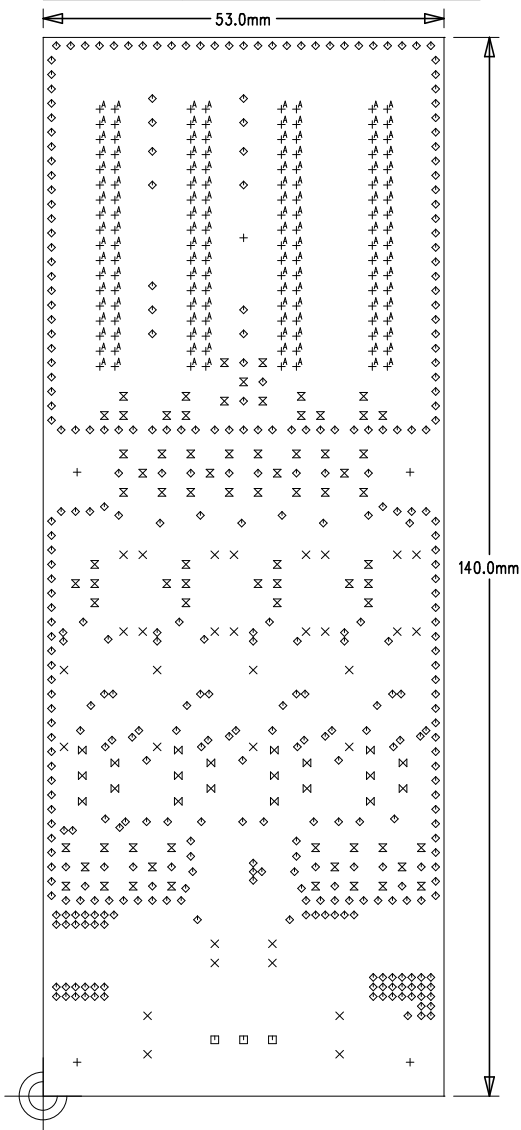
FMB Informatica		FR4\SPECORE C.2.1,8mm	
NOTE: RAME=32mm.		DATA: 08\03\2012	
CODICE: FMB1202A		CLIENTE: INFN	
SOLDER MASK (BOTTOM)		DESCRIZIONE:	



FMB Informatica		FMB Informatica	
		DESCRIZIONE: PISTE LATO SALDATURE	
CLIENTE: INFN		CODICE: FMB1202A	
DATA: 08\03\2012	NOTE: RAME=35um. FR4\SPEC20RE C.2. 1,6mm		



 FMB Informatica	DESCRIZIONE:	
	PIANO DI FORATURA	
	CLIENTE: INFN	
	CODICE : FMB1202A	
	NOTE: RAME=35um.	DATA:
	FR4/SPESSORE C.S. 1,6mm	08/03/2012



SIZE	QTY	SYM	PLATED	TOL
17.7	364	◇	YES	+/-0.0
31.5	32	×	YES	+/-0.0
35.4	144	+ <sup>A</sup>	YES	+/-0.0
39.4	73	⊗	YES	+/-0.0
43.3	20	⊠	YES	+/-0.0
47.2	3	□	YES	+/-0.0
137.8	5	+	NO	+/-0.0



## Bibliography

- [74h] *74HC4538, 74HCT4538; Dual retriggerable precision monostable multivibrator*. Datasheet (cit. on p. 53).
- [AA+06] M. Allen-Auerbach et al. *Diagnostic Nuclear Medicine*. Ed. by C. Schiepers. Springer, 2006 (cit. on p. 3).
- [Ago+03] S. Agostinelli et al. “Geant4—A simulation toolkit”. In: *Nuclear Instruments and Methods in Physics Research Section A: Accelerators, Spectrometers, Detectors and Associated Equipment* 506.3 (2003), pp. 250–303. ISSN: 0168-9002. DOI: 10.1016/S0168-9002(03)01368-8. URL: <http://www.sciencedirect.com/science/article/pii/S0168900203013688> (cit. on p. 39).
- [All+06] J. Allison et al. “Geant4 developments and applications”. In: *Nuclear Science, IEEE Transactions on* 53.1 (2006), pp. 270–278. ISSN: 0018-9499. DOI: 10.1109/TNS.2006.869826 (cit. on p. 39).
- [Ber+05] M.J. Berger et al. *ESTAR, PSTAR, and ASTAR: Computer Programs for Calculating Stopping-Power and Range Tables for Electrons, Protons, and Helium Ions (version 1.2.3)*. National Institute of Standards and Technology, Gaithersburg, MD (USA). 2005. URL: <http://physics.nist.gov/Star> [2013-01-05] (cit. on p. 15).
- [BK70] C. J. Borkowski and M. K. Kopp. “Some Applications and Properties of One- and Two-Dimensional Position-Sensitive Proportional Counters”. In: *IEEE Trans. Nucl. Sci.* 17.3 (1970), pp. 340–349 (cit. on p. 45).
- [BS90] R. Brechner and M. Sigh. “Iterative Reconstruction of Electronically Collimated SPECT Images”. In: *IEEE Trans. Nucl. Sci.* 37.3 (1990), pp. 1328–1332 (cit. on p. 21).
- [Can96] M. Candilera. *Algebra Lineare e Geometria*. Edizioni Libreria Progetto, 1996 (cit. on pp. 8, 25).
- [CND07] Valentino Orsolini Cencelli, Francesco de Notaristefani, and Enrico D’Abramo. “High-speed readout for the H8500 flat panel PSPMT”. In: *Nuclear Instruments and Methods in Physics Research Section A: Accelerators, Spectrometers, Detectors and Associated Equipment* 571.1–2 (2007). Proceedings of the 1st International Conference on Molecular Imaging Technology, EuroMedIm 2006, pp. 389–391. ISSN: 0168-9002. DOI: 10.1016/j.nima.2006.10.116. URL: <http://www.sciencedirect.com/science/article/pii/S0168900206019140> (cit. on p. 19).

- [Com23] Arthur H. Compton. “A Quantum Theory of the Scattering of X-Rays by Light Elements”. In: *Phys. Rev.* 21.5 (1923), pp. 483–502 (cit. on p. 21).
- [Dou09] Geoff Dougherty. *Digital Image Processing for Medical Applications*. Cambridge University Press, 2009 (cit. on p. 3).
- [DS82] D. Doria and M. Singh. “COMparison od Reconstruction Algorithms for an Electronically Collimated Gamma Camera”. In: *IEEE Trans. Nucl. Sci.* NS-29.1 (1982), pp. 447–451 (cit. on p. 21).
- [DZ09] G. D. Domenico and G. Zavattini. *Technetium-99m radiopharmaceuticals: Status and trends*. IAEA Radioisotopes and Radiopharmaceuticals Series 1. IAEA, 2009 (cit. on p. 4).
- [Fig+05] S.D. Figueroa et al. “Performance characteristics of an integrated small animal SPECT/CT unit”. In: *Nuclear Science Symposium Conference Record, 2005 IEEE*. Vol. 3. 2005, 5 pp. DOI: 10.1109/NSSMIC.2005.1596659 (cit. on p. 19).
- [Fon+11] C. L. Fontana et al. “Tomographic back-projection algorithm for “incomplete” Compton x-rays detector”. In: *AIP Conference Proceedings* 1336 (2011), p. 197 (cit. on pp. 13, 21, 109).
- [Gf05] Chris Guy and Dominic ffytche. *An Introduction to The Principles of Medical Imaging*. Imperial College Press, 2005 (cit. on p. 2).
- [Gue04] A. del Guerra. *Ionizing Radiation Detectors for Medical Imaging*. World Scientific, 2004 (cit. on p. 7).
- [H10] *Flat panel type multianode photomultiplier tube assembly H10966 series*. Datasheet (cit. on p. 19).
- [Ham] *Photomultiplier Tubes, Basics and Applications*. Tech. rep. Hamamatsu Photonics, 2006 (cit. on p. 7).
- [HH89] Paul Horowitz and Winfield Hill. *The Art of Electronics*. Cambridge University Press, 1989 (cit. on p. 51).
- [HLS90] T. Hebert, R. Leahy, and M. Singh. “Three Dimensional Maximum-Likelihood Reconstruction for an Electronically Collimated Single-Photon-Emission Imaging System”. In: *Optical Society of America* 7.7 (1990), pp. 1305–1313 (cit. on p. 21).
- [How] *AN-1515 A Comprehensive Study of the Howland Current Pump*. Tech. rep. SNOA474. Texas Instruments, 2008 (cit. on p. 62).
- [Hri+90] A.V. Hristova et al. “Compton edge energy calibration of organic detectors”. In: *International Journal of Radiation Applications and Instrumentation. Part A. Applied Radiation and Isotopes* 41.9 (1990), pp. 887–889. ISSN: 0883-2889. DOI: 10.1016/0883-2889(90)90068-R. URL: <http://www.sciencedirect.com/science/article/pii/088328899090068R> (cit. on p. 82).

- [JOP+01] Eric Jones, Travis Oliphant, Pearu Peterson, et al. *SciPy: Open source scientific tools for Python*. 2001–. URL: <http://www.scipy.org/> (cit. on p. 77).
- [Kiu10] Jaan Kiusalaas. *Numerical Methods in Engineering with Python*. 2nd edition. Ca, 2010 (cit. on p. 77).
- [KN28] Oskar Klein and Yoshio Nishina. “Über die Streuung von Strahlung durch freie Elektronen nach der neuen relativistischen Quantendynamik von Dirac”. In: *Zeitschrift für Physik* 52.11-12 (1928), pp. 853–868 (cit. on p. 21).
- [Kno10] G. F. Knoll. *Radiation Detection and Measurement*. John Wiley & Sons, 2010 (cit. on p. 4).
- [Ku66] H. H. Ku. “Notes on the use of propagation of error formulas”. In: *J. Res. Nat. Bur. Stand. Sec. C: Eng. Inst.* 70C.4 (1966), p. 263 (cit. on p. 24).
- [Lab] *LabVIEW, Laboratory Virtual Instrumentation Engineering Workbench*. URL: <http://www.ni.com/labview/> (cit. on p. 71).
- [Lm7] *LM7171 Very High Speed, High Output Current, Voltage Feedback Amplifier*. Datasheet (cit. on pp. 62, 63).
- [Loe+02] E.V.D van Loef et al. “Scintillation properties of LaBr<sub>3</sub>:Ce<sup>3+</sup> crystals: fast, efficient and high-energy-resolution scintillators”. In: *Nuclear Instruments and Methods in Physics Research Section A: Accelerators, Spectrometers, Detectors and Associated Equipment* 486.1–2 (2002). Proceedings of the 6th International Conference on Inorganic Scintillators and their Use in Scientific and Industrial Applications, pp. 254–258. ISSN: 0168-9002. DOI: 10.1016/S0168-9002(02)00712-X. URL: <http://www.sciencedirect.com/science/article/pii/S016890020200712X> (cit. on p. 17).
- [LR09] C. Leroy and P. G. Rancoita. *Principles of Radiation Interaction in Matter and Detection*. World Scientific, 2009 (cit. on p. 3).
- [Lt1] *Fast ±150mA Power Buffer LT1010*. Datasheet (cit. on p. 51).
- [Max] *MAX961 Single/Dual/Quad, Ultra-High-Speed, +3V/+5V, Beyond-the-Rails Comparators*. Datasheet (cit. on pp. 62, 63).
- [Mos+08] G. Moschini et al. *A Cyclotron Isotope Production Center For Biomedical Research*. Tech. rep. INFN-LNL-225. ISBN 978-88-7337-013-0. National Laboratories of Legnaro LNL (Italy), 2008 (cit. on p. 2).
- [Naq+93] A.A. Naqvi et al. “Energy resolution of NE102A and NE230 scintillators for monoenergetic gamma rays”. In: *Nuclear Instruments and Methods in Physics Research Section A: Accelerators, Spectrometers, Detectors and Associated Equipment* 324.1–2 (1993), pp. 223–225. ISSN: 0168-9002. DOI: 10.1016/0168-9002(93)90980-V. URL: <http://www.sciencedirect.com/science/article/pii/016890029390980V> (cit. on p. 13).

- [Ne1] *BC-400,BC-404,BC-408,BC-412,BC-416 Premium Plastic Scintillators*. Datasheet (cit. on p. 13).
- [Nem] *NEMA Standards Publication NU 1-2001, Performance Measurements of Scintillation Cameras*. National Electrical Manufacturers Association (cit. on p. 81).
- [OBC97] C.E. Ordonez, A. Bolozdynya, and W. Chang. “Doppler broadening of energy spectra in Compton cameras”. In: *Nuclear Science Symposium, 1997. IEEE*. Vol. 2. 1997, 1361–1365 vol.2. DOI: 10.1109/NSSMIC.1997.670574 (cit. on pp. 24, 39, 40).
- [Olc+05] Peter Demetri Olcott et al. “Compact Readout Electronics for Position Sensitive Photomultiplier Tubes”. In: *IEEE Trans. Nucl. Sci.* 52.1 (2005), pp. 21–27 (cit. on pp. 19, 45).
- [Pan+04] R Pani et al. “Imaging detector designs based on flat panel PMT”. In: *Nuclear Instruments and Methods in Physics Research Section A: Accelerators, Spectrometers, Detectors and Associated Equipment* 527.1–2 (2004). Proceedings of the 2nd International Conference on Imaging Technologies in Biomedical Sciences, pp. 54–57. ISSN: 0168-9002. DOI: 10.1016/j.nima.2004.03.037. URL: <http://www.sciencedirect.com/science/article/pii/S0168900204003882> (cit. on p. 19).
- [Pan+09] R. Pani et al. “Investigation on a small FoV gamma camera based on LaBr3:Ce continuous crystal”. In: *Nuclear Physics B - Proceedings Supplements* 197.1 (2009). 11th Topical Seminar on Innovative Particle and Radiation Detectors (IPRD08), pp. 202–205. ISSN: 0920-5632. DOI: 10.1016/j.nuclphysbps.2009.10.067. URL: <http://www.sciencedirect.com/science/article/pii/S0920563209007889> (cit. on p. 81).
- [Pan+11] Roberto Pani et al. “LaBr3(Ce) and NaI(Tl) performance comparison for single photon emission imaging”. In: *Nuclear Science Symposium and Medical Imaging Conference (NSS/MIC), 2011 IEEE*. 2011, pp. 4433–4436. DOI: 10.1109/NSSMIC.2011.6153854 (cit. on p. 81).
- [Par00] L. C. Parra. “Reconstruction of cone-beam projections from Compton scattered data”. In: *IEEE Trans. Nucl. Sci.* 47.4 (2000), pp. 1543–1550 (cit. on pp. 2, 21).
- [PM06] V. Popov and S. Majewski. “A Compact High Performance Readout Electronics Solution for H9500 Hamamatsu 256 Multianode Photomultiplier Tube for Application in Gamma Cameras”. In: *Nuclear Science Symposium Conference Record, 2006. IEEE*. Vol. 5. 2006, pp. 2981–2985. DOI: 10.1109/NSSMIC.2006.356501 (cit. on p. 19).
- [Pov] *POV-ray, Persistence of Vision Raytracer*. URL: <http://www.povray.org/> (cit. on p. 27).
- [Pre11] Jennifer Prekeges. *Nuclear Medicine Instrumentation*. Jones and Bartlett Publishers, 2011 (cit. on p. 8).



- [Quc] *Qucs, Quite Universal Circuit Simulator*. URL: <http://qucs.sourceforge.net/> (cit. on pp. 53, 59).
- [Ros+11a] P. Rossi et al. “Design and Performance Tests of the Calorimetric Tract of a Compton Camera for Small-Animals Imaging.” In: *Nucl. Instr. and Meth. A* 628 (2011), pp. 430–433 (cit. on pp. 2, 13, 19, 21, 109).
- [Ros+11b] P. Rossi et al. “X-rays Compton detectors for biomedical application”. In: *AIP Conference Proceedings* 1336 (2011), p. 356 (cit. on pp. 2, 8, 13, 109).
- [SHR99] A. C. Sauve, A. O. III Hero, and L. W. Rogers. “3D image reconstruction for a Compton SPECT camera model”. In: *IEEE Trans. Nucl. Sci.* 46 (1999), pp. 2075–2084 (cit. on pp. 2, 21).
- [Sie+96] Stefan Siegel et al. “Simple Charge Division Readouts for Imaging Scintillator Arrays using a Multi-Channel PMT”. In: *IEEE Trans. Nucl. Sci.* 43.3 (1996), pp. 1634–1641 (cit. on p. 45).
- [Sin83] M. Singh. “An electronically collimated gamma camera for single photon emission computed tomography. Part 1: Theoretical considerations and design criteria”. In: *Medical Physics* 10.4 (1983), pp. 421–427 (cit. on p. 21).
- [SP03] J. A. Sorensens and M. E. Phelps. *Physics in Nuclear Medicine*. W.B. Saunders Company, 2003 (cit. on pp. 8, 12).
- [SQR95] G. Stöcklin, S. M. Qaim, and F. Rösch. “The Impact of Radioactivity on Medicine”. In: *Radiochimica Acta* 70/71 (1995), pp. 249–272 (cit. on p. 2).
- [TNE74] R. Todd, J. Nightingale, and D. Everett. “A proposed Gamma Camera”. In: *Nature* 251 (1974), pp. 132–134 (cit. on p. 21).
- [TT06] David I Thwaites and John B Tuohy. “Back to the future: the history and development of the clinical linear accelerator”. In: *Physics in Medicine and Biology* 51.13 (2006), R343. URL: <http://stacks.iop.org/0031-9155/51/i=13/a=R20> (cit. on p. 3).
- [Wei] E. W. Weisstein. *Shear Matrix*. URL: <http://mathworld.wolfram.com/ShearMatrix.html> [2013-01-10] (cit. on p. 87).
- [Wei95] Steven Weinberg. *The Quantum Theory of Fields*. Vol. 1. Cambridge University Press, 1995 (cit. on p. 21).
- [ZK03] A. Zoglauer and G. Kanbach. “Doppler broadening as a lower limit to the angular resolution of next-generation Compton telescopes”. In: *Society of Photo-Optical Instrumentation Engineers (SPIE) Conference Series*. Ed. by J. E. Truemper and H. D. Tananbaum. Vol. 4851. Society of Photo-Optical Instrumentation Engineers (SPIE) Conference Series. Mar. 2003, pp. 1302–1309. DOI: 10.1117/12.461177 (cit. on p. 39).